BROKEN BAR DETECTION IN SYNCHRONOUS MACHINES BASED WIND ENERGY CONVERSION SYSTEM

A Dissertation

by

MINA MASHHADI RAHIMIAN

Submitted to the Office of Graduate Studies of
Texas A&M University
in partial fulfillment of the requirements for the degree of

DOCTOR OF PHILOSOPHY

August 2011

Major Subject: Electrical Engineering

BROKEN BAR DETECTION IN SYNCHRONOUS MACHINES BASED WIND ENERGY CONVERSION SYSTEM

A Dissertation

by

MINA MASHHADI RAHIMIAN

Submitted to the Office of Graduate Studies of
Texas A&M University
in partial fulfillment of the requirements for the degree of

DOCTOR OF PHILOSOPHY

Approved by:

Chair of Committee,	Karen Butler-Purry
Committee Members,	Mehrdad Ehsani
	Shankar P. Bhattacharyya
	Reza Langari
Head of Department,	Costas N. Georghiades

August 2011

Major Subject: Electrical Engineering

ABSTRACT

Broken Damper Bar Detection in Synchronous Machines Based Wind Energy Conversion System.

(August 2011)

Mina Mashhadi Rahimian,

B.S., University of Wisconsin, Madison;

M.S., University of Wisconsin, Madison

Chair of Advisory Committee: Dr. Karen Butler-Purry

Electrical machines are subject to different types of failures. Early detection of the incipient faults and fast maintenance may prevent costly consequences. Fault diagnosis of wind turbine is especially important because they are situated at extremely high towers and therefore inaccessible. For offshore plants, bad weather can prevent any repair actions for several weeks. In some of the new wind turbines synchronous generators are used and directly connected to the grid without the need of power converters.

Despite intensive research efforts directed at rotor fault diagnosis in induction machines, the research work pertinent to damper winding failure of synchronous machines is very limited. This dissertation is concerned with the in-depth study of damper winding failure and its traceable symptoms in different machine signals and parameters. First, a model of a synchronous machine with damper winding based on the

winding function approach is presented. Next, simulation and experimental results are presented and discussed. A specially designed inside-out synchronous machine with a damper winding is employed for the experimental setup. Finally, a novel analytical method is developed to predict the behavior of the left sideband amplitude for different numbers and locations of the broken bars. This analysis is based on the magnetic field theory and the unbalanced multiphase circuits.

It is found that due to the asymmetrical structure of damper winding, the left sideband component in the stator current spectrum of the synchronous machine during steady state asynchronous operation is not similar to that of the induction machine with broken bars. As a result, the motor current signature analysis (MCSA) for detection rotor failures in the induction machine is usable to detect broken damper bars in synchronous machines. However, a novel intelligent-systems based approach is developed that can identify the severity of the damper winding failure. This approach potentially can be used in a non-invasive condition monitoring system to monitor the deterioration of a synchronous motor damper winding as the number of broken bars increase over time. Some other informative features such as speed spectrum, transient time, torque-speed curve and rotor slip are also found for damper winding diagnosis.

DEDICATION

To the precious fruits of my life

Amir and Mohammad

ACKNOWLEDGEMENTS

I would like to thank my advisor, Dr. Karen Butler-Purry, for her support, patience and understanding throughout the period of this research. I would also like to thank the members of my graduate study committee, Dr. Mehrdad Ehsani, Dr. Shankar P. Bhattacharyya and Dr. Reza Langari, for accepting my request to be a part of the committee.

I would like to extend my gratitude to my fellow colleagues, Robert Vartanian and Dr. Seung Choi, for their friendship and support. I would also like to thank my best friend, Ms. S. Ghiassi, for her encouragement and valuable life lessons.

Also, I would like to thank my dear husband and beloved sons for their emotional support and patience during this period.

TABLE OF CONTENTS

Page

Page

Page

LIST OF FIGURES

Page

Page

Page

Page

LIST OF TABLES

Page

1. INTRODUCTION AND LITERATURE REVIEW

1.1 Fault Diagnosis in Electric Machines

With the increasing dependence on rotating electrical machines in a wide variety of industrial applications, condition monitoring leading to fault diagnosis has received intense research interest. Early diagnosis of faults, while the system is still operating in a controllable region, can help avoid abnormal event progression and reduce productivity loss, which in turn can help avoid major system breakdowns and catastrophes. Hence, fault diagnosis is a major research topic attracting considerable interest from industrial practitioners as well as academic researchers.

Motor condition monitoring is a technique of sensing the health of electrical machines. Analysis of the monitored data quantifies the condition of the machine, so that faults can be detected and diagnosed at the developing stage.

The overall concept of fault diagnosis consists of the following three essential tasks:

- Fault detection: detection of the occurrence of faults, which lead to undesired or intolerable behavior of the system
- Fault isolation: localization (classification) of different faults
- Fault analysis or identification: determination of the type, magnitude and cause of the fault

---

This dissertation follows the style of *IEEE Transactions on Industrial Applications.*

A good machine diagnostic procedure attempts to extract a diagnosis by analysis of the minimum data and measurements from a machine, so that it gives a clear indication of incipient failure modes in a minimum time. Electrical machines are subject to many different types of mechanical and electrical faults which can broadly be classified as the following: 1) abnormal connection of the stator windings, open or short circuit in one or more turns of a stator phase winding; 2) open or short circuited rotor winding in wound rotor machines; 3) broken rotor bars or rotor end-rings; 4) Air gap irregularities; 5) rotor mechanical faults such as bearing damage, eccentricity, bent shaft, and misalignment [1]. Each of these fault conditions produces specific symptoms during motor operation which can be described as follows:

- unbalanced air-gap voltages and line currents
- increased torque pulsations
- decreased average torque
- increased losses and reduction in efficiency
- excessive temperature
- audible noise and motor vibration

For the purpose of detecting these symptoms from the fault-related signals, several diagnostic techniques have been developed so far. These methods to identify the above faults can be summarized as follows [2], [3]:

- motor-current signature analysis (MCSA)
- electromagnetic field monitoring, search coils, coils wound around shafts
- temperature measurements

- infrared recognition
- radio-frequency emissions monitoring
- noise and vibration monitoring
- chemical analysis
- partial discharge measurement

1.2 Motor Fault Conditions and Causes

This subsection gives a brief summary of the most common motor fault conditions, their causes and symptoms. A survey on electric motor failures statistics, shown in Fig. 1.1, indicates that some types of faults have been reported more frequently than others.

1.2.1 Bearing Faults

Bearing faults accounts for over 50% of failures of electrical motors. In industrial facilities non-ideal conditions such as fatigue, ambient vibration, overloading, misalignment, contamination, corrosion, and wrong lubrication are the main causes of bearing failures. These conditions damage the inner raceway, outer raceway and rolling elements, and generate mechanical vibration causing audible noise. These mechanical vibrations cause slight rotor displacement which, in turn creates air gap variations. Therefore, the basic fault signature frequency equation of line current due to bearing defects is adopted from eccentricity literature [4].

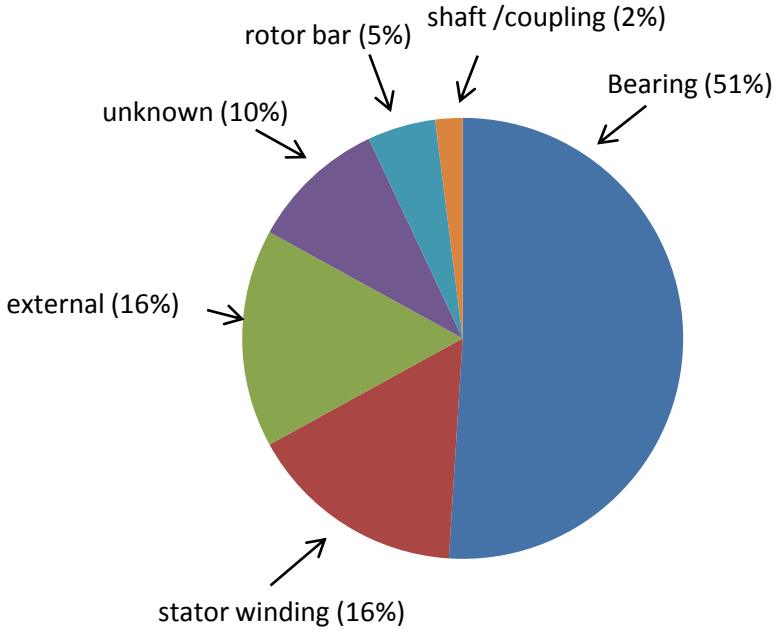

Figure 1.1 Motor failure distribution statistics. [5]

There are some commonly used methods to diagnose bearing failure and prevent further damage to motors. These methods are thermal or vibration analysis which requires additional sensors or transducers to be installed on motors. For small machines, these methods may not be economically or physically feasible. An alternative approach for monitoring bearings is based on continuous monitoring of the stator current. This method, which is known as Motor Current Signature Analysis (MCSA), has become one of the most attractive motor diagnostic methods because of its non-invasive, reliable and cost effective nature. Bearing faults are commonly classified as outer race, inner race, ball defect and cage defect. Each fault has specific vibration frequency components

which are dependent on the rotor speed and geometry of the bearing. The fault signatures corresponding to each specific bearing failure have been published in the diagnostic literature [6-10].

1.2.2 Stator Winding Faults

Stator failures are essentially due to thermal, electrical, mechanical, and environmental stresses acting on the stator. Thermal stress is probably the most recognized cause of insulation degradation and ultimate failure. The main sources of thermal stress in electric machinery are copper losses, eddy current and stray load losses in the copper conductors. High temperature causes a chemical reaction which damages the insulation material. The copper conductors expand faster than insulation material during a sudden temperature increase which cause stress on insulation material [11], [12]. The electrical stresses leading to winding failures can be classified into dielectric, tracking, corona, and transient voltage conditions. Mechanical stresses might be due to electromagnetic vibration, differential expansion due to temperature variations, coil movement and rotor striking the stator due to bearing failures, shaft deflection, rotor-to-stator misalignment, etc. Environmental stresses can be created by oil contamination, moisture, dirt, leakage in cooling systems.

Several monitoring techniques have been published in diagnostic literature for detection of stator winding failures. They propose using different parameters such as magnetic flux, vibration, noise, instantaneous angular speed, temperature, air-gap torque,

induced voltage, power, partial discharge, gas analysis, surge testing and motor circuit analysis [13].

1.2.3 Rotor Bar and End Ring Faults

Rotor failures in induction machines include broken or cracked rotor bars or end rings. Two different types of squirrel-cage rotors exist in induction motors: cast and fabricated. Cast cage rotors are used in motors up to 3-MW rating and fabricated cages are used for higher ratings. Cast rotors, though more rugged than the fabricated type, can almost never be repaired once faults such as cracked or broken rotor bars develop in them.

The rotor bar and end-ring breakage can be caused by the following types of stresses [3]:

- thermal stresses due to thermal overload and unbalance, hot spots, or excessive losses, sparking
- magnetic stresses caused by electromagnetic forces, unbalanced magnetic pull, electromagnetic noise, and vibration
- residual stresses due to manufacturing problems
- dynamic stresses arising from shaft torques, centrifugal forces, and cyclic stresses
- environmental stresses caused by for example contamination and abrasion of rotor material due to chemicals or moisture
- mechanical stresses due to the loose laminations, fatigued parts, bearing failure

Breakages in the rotor cage winding introduce a distortion in the air-gap field that produces sideband components in the line current spectrum around the fundamental and around other harmonics caused by non ideal winding distribution. The left sideband is due to electric and magnetic asymmetry of excitation frequency and the right sideband is due to the speed oscillations. A broken rotor bar can be considered as rotor asymmetry that causes unbalanced currents, torque pulsation and decreased average torque.

1.2.4 Eccentricity-Related Faults

Air gap eccentricity arises when there is a non-uniform distance between the rotor and stator in the air gap. The non-uniform air-gap causes the varying inductances giving rise to unbalanced magnetic flux within the air gap. This creates fault harmonics in the line current which can be identified in the frequency spectrum. When eccentricity becomes large, the resulting unbalanced radial forces can cause stator to rotor rub, and this can result in damage of the stator and rotor.

There are two types of eccentricity: static and dynamic. In the case of static eccentricity, the centerline of the shaft is at a constant offset from center of the stator. Therefore, the non-uniform air-gap does not vary in time. On the other hand when dynamic eccentricity occurs, the centerline of the shaft is at a variable offset from center of the stator and the air-gap length changes as the rotor rotates dynamically. In reality, both static and dynamic eccentricities tend to co-exist. Improper mounting, the ovality of the stator core, loose or missing bolt, a bent rotor shaft or misalignment, bearing wear and rotor unbalance might be causes of air gap eccentricity [3], [14-16].

1.3 Literature Review on Synchronous Machine Fault Diagnosis

This subsection summarizes the important electrical and mechanical failures in synchronous machines and the corresponding diagnosis techniques proposed in the literature. Some failures, like stator inter-turn faults, bearing faults and eccentricities, are common in all types of electrical machines. However, some faults like field winding faults, broken damper bars or end ring, are specific to wound rotor synchronous machines, and demagnetization faults are limited to permanent magnet synchronous machines (PMSMs).

Like induction machines, synchronous machines are subject to many different types of mechanical and electrical faults which can broadly be classified into the following: 1) open or short circuit in one or more turns of a stator winding; 2) open or short circuited rotor winding in wound rotor synchronous machines; 3) broken damper bars or end-rings; 4) eccentricities; 5) rotor mechanical faults such as bearing damage, bent shaft, and misalignment; 6) demagnetization fault in PMSMs.

Each of these fault conditions produces specific symptoms during motor operation which can be described as follows:

- unbalanced line currents and air-gap voltages
- excessive temperature
- audible noise and motor vibration
- lower average torque

- higher torque pulsations
- increased losses

Some of the fault conditions in synchronous machines have similar causes and symptoms to the same faults in induction machines which have been discussed in subsection 1.2.

1.3.1 Damper Winding Fault

To produce torque in synchronous machines, the rotor must be turning at synchronous speed which is the speed of the stator field. At any other speed, the rotating field of stator poles will not be synchronized with rotor poles. First it attracts and then repels the rotor poles. This condition produces no average torque and the machine will not start. Using a dc motor or a damper winding, a synchronous machine can be brought near to the synchronous speed. Damper windings, as shown in Fig. 1.2, consist of heavy copper bars, with the two ends shorted together, installed in rotor slots. The currents induced in the bars interact by the rotating air-gap field and produces torque. In other words, the machine is started as an induction motor [17]. The field winding is excited by a dc current when the machine is brought up to the synchronous speed. When the load is suddenly changed, an oscillatory motion will be superimposed on the normal synchronous rotation of the shaft. The damper winding helps damping out these oscillations.

Diagnostics of broken damper bars in synchronous machines has not been studied as widely as the other faults like eccentricity and inter-turn faults [18-21].

During transients, the electromagnetic behavior of asynchronous machines with damper windings is similar to that of induction machines. During transient times, when the machine accelerates from zero speed to synchronous speed, a significant current flows in the damper winding. Excessive start-stop cycles or frequent load or speed changes can cause the breakage of the damper bars.

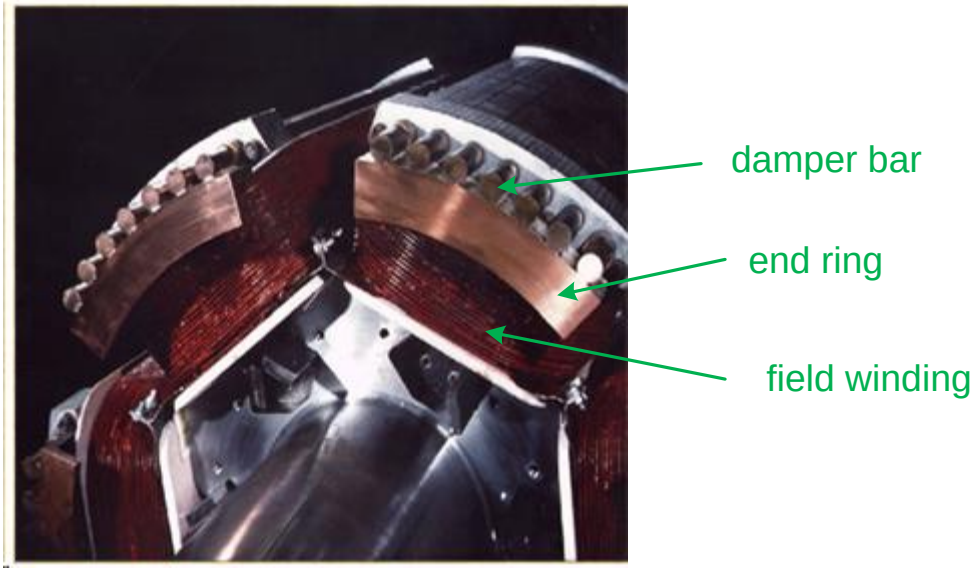

Figure 1.2 A salient pole synchronous machine with damper winding and interrupted end ring. (Courtesy of TECO-Westinghouse)

An on-line diagnosis method for detection of broken bars has been proposed in [22] using flux probe and finite element modeling. For the squirrel cage induction machines, several methods of detection of broken rotor bars have been reported in the literature. It has been found that in squirrel cage induction machines when a bar breaks some of the current that would have flown in that bar will flow into the two adjacent bars

on either side. This could result in breakage of several bars [23]. Similar effects have been reported for the converter-fed synchronous machines with broken damper bars [24]. Winding function analysis and time-stepping Finite Element Analysis have been used to study the broken damper bars and end ring [22], [25].

For detecting the broken damper bars flux probes can be attached to the stator bore surface for measurement of air gap flux waveform during acceleration from standstill to rated speed [22]. Another method is the separation of pole voltages of the field winding according to its polarity [26]. This way, the difference of the pole voltages can be determined. The main field of a symmetrical built machine disappears in the difference voltage but the difference voltage which is caused by the noise field of the missing damper bar will remain.

1.3.2 Demagnetization Fault in PMSM

In comparison to other types of ac motors, permanent magnet synchronous motors (PMSMs) are becoming more popular in applications with high-speed operation and precise torque control. The demagnetization phenomenon is mainly due to armature reaction especially in the high torque conditions. Some other advantageous features include high efficiency, low noise, high torque to current ratio, high power to weight ratio, and robustness.

During the normal operation of the PMSM, the inverse magnetic field produced by the stator current, opposes the permanent magnets remnant induction. When this phenomenon is repeated, the permanent magnets will be demagnetized. This

demagnetization can be all over the pole (complete demagnetization), or on a part of the pole (partial demagnetization). High temperature can also demagnetize the magnet. A stator winding short-circuit fault may partially demagnetize a surface mount magnet. Partial demagnetization, causes magnetic force harmonics, noise and vibration in the machine unbalanced magnetic pull.

The demagnetization effects on the parameters of motors such as cogging torque, torque ripple, back EMF, and load angle curve were investigated in [27]. For steady state analysis under demagnetization conditions, fast Fourier transform (FFT) of the stator current is used for frequency analysis. Time-frequency analysis methods are used for non-stationary conditions. These techniques such as, short-time Fourier transform (STFT), continuous wavelet transform (CWT) and discrete wavelet transform (DWT), require the proper selection of parameters such as window size and coefficients

Field reconstruction method (FRM) can also be used to detect demagnetization faults in PMSMs. The flux linkages of the stator phases which are calculated by FRM are used to monitor the faults [28].

1.3.3 Eccentricity Fault

Various diagnosis methods for eccentricity fault detection in synchronous machines have been proposed in literature. The modified winding function approach (MWFA) accounting for all space harmonics, and the finite element method have been used to model the salient pole synchronous machines. These models show the effect of

dynamic air-gap eccentricity on the performance of a salient pole synchronous machine [29].

In [30], a method of detecting static eccentricity (SE), dynamic eccentricity (DE), and mixed eccentricity (ME) in three-phase PMSMs is presented. The nominated index is the amplitude of sideband components with a particular frequency pattern in the stator current spectrum. The occurrence, as well as the type and percentage, of eccentricity can be determined using this index. After determination of the correlation between the index and the SE and DE, the type of the eccentricity is determined by a *k*-nearest neighbor classifier. Then a three-layer artificial neural network is employed to estimate the eccentricity degree and its type.

In [31], implementation and detection of rotor faults such as static and dynamic eccentricities and broken magnets in permanent magnet synchronous machines are investigated. A new flux estimation method was developed that does not require the measurement of the rotor position or speed. In this method, the stator currents and voltages are used for detection of these and other rotor faults.

1.3.4 Stator Inter-turn Faults

One of the most common failures in synchronous motors is the inter-turn short circuit in one of the stator coils. Stator failures are essentially due to electrical, mechanical, thermal, and environmental stresses acting on the stator. The most recognized cause of insulation degradation and ultimate failure is thermal stress. The

dielectric, corona, tracking, and transient voltage conditions are some of the electrical stresses leading to inter-turn short circuit failures [32].

In the case of an inter-turn fault in stator windings, the machine symmetry is destroyed. This produces a reverse rotating field which decreases the output torque and increases losses per ampere of fundamental frequency of the positive sequence current. The stator faults in Reluctance Synchronous Motors (RSM) under steady state operating condition were studied in [33]. The detailed modeling of the faulted machine has been carried out using Modified Winding Function Approach (MWFA). Monitoring the stator current in presence of such faults shows that odd triple harmonics are increased in the line current of RSMs with inter-turn faults. The line current of the faulty phase increases further when the number of shorted turns increases. An increase of 9th harmonic seems to be a good indication of inter-turn faults.

Stator inter-turn faults in a salient pole synchronous motor can be detected by analyzing the field current of the machine. Some of the even harmonics in the field current have been reported to increase with stator inter-turn faults. Due to internal structural asymmetries of field windings, some of these components clearly increase when stator inter-turn faults occur [19].

For analyzing internal phase and ground faults in stator windings, a mathematical model for a synchronous machine was presented in [34]. This method employs a direct phase representation, using a traditional coupled circuit approach. This analysis was implemented in a computer simulation package called GENSIM.

A specific frequency pattern of the stator current is derived for short circuit fault detection in PMSMs [35]. The amplitude of the side-band components at these frequencies is used to determine the number of short circuited turns. Using the mutual information index, the relation between the nominated criterion and the number of short circuited turns is specified. The occurrence and the number of short circuited turns are predicted using support vector machine (SVM) as a classifier.

The two-reaction theory is well suited for computer modeling of synchronous machines. However, in the derivation of the dq0 model of a synchronous machine, the machine windings are assumed to be sinusoidally distributed. This implies that all higher space harmonics of the stator windings distributions are neglected. In the case of an internal fault, the stator windings no longer have the characteristics of sinusoidally distributed windings. The faulted windings will produce stronger space harmonics. Moreover, the symmetry between the machine windings will no longer be present. Therefore, the conventional *dq*0 model is not suitable to analyze internal faults.

Inter-turn faults of synchronous machines can be modeled based on the actual winding arrangements [36]. This method which is known as winding function approach, calculates the machine inductances directly from the machine winding distribution. Using his model, the space harmonics produced by the machine windings are taken into account. In [37], the winding function approach is used to simulate inter-turn faults in stator windings of permanent magnet synchronous machines.

A time-stepping finite-element-method (FEM) is another analysis method to study synchronous machines with inter-turn faults. In [38], FEM is employed for

internal fault analysis of surface-mounted permanent-magnet synchronous machines. The method is used for magnetic field study and determining the machine parameters under various fault conditions and the effect of machine pole number and number of faulted turns on machine parameters.

1.3.5 Rotor Inter-turn Faults

Rotor winding inter-turn faults are common electrical faults in synchronous machines. Their existence may result serious problems such as high rotor current, high winding temperature, low reactive output power, distorted voltage waveform, and vibration. Rotor winding inter-turn faults are mainly caused by poor manufacturing or operation conditions such as loose rotor end winding, loose spacer block, poor trimming of soldered joint, deformation of high-speed rotor winding due to centrifugal force, overheating and poor insulation.

There have been studies on diagnosis of rotor winding turn-to-turn faults. One method is based on indirect measurement of the impedance of the rotor field-winding during operation [39]. This method is useful when the number of shorted-turns is significant.

Some methods are based on detection of flux asymmetry created by shorted turns by applying ac current to the field [40]. This method is accurate but not easy to implement because it requires removing the rotor from the bore. Some reliable methods based on direct measurement of the air-gap magnetic flux can be applied to the machine in operation [41]. The flux is measured by a search coil installed in the air gap.

Neural network models of machines can be used to detect the rotor turn faults. Neural network based methods require training data through simulation or experiments. A mathematical model of the machine is needed for simulated data. Experimental training data can be acquired using a machine in which the rotor turns can be shorted.

A method based on traveling waves is proposed in [42]. This method along with neural network feature extraction and a novelty detection algorithm are used for diagnosis of short-circuit windings in rotating machines and other equipment containing symmetrical windings.

The terminal parameters are affected by the fault conditions of the rotor windings, but it's difficult to relate them together by accurate mathematical expressions. An artificial neural network method is investigated in [43] for rotor-shorted winding fault diagnosis. Since it is difficult to find the faulty samples in practical applications, these samples are gained through calculation. Using this method, the severity of fault can be detected, but the location of faults cannot be determined.

1.3.6 Bearing Faults

Even under normal operating conditions with balanced load and good alignment, bearing failures may take place. Flaking of bearings might occur when fatigue causes small pieces to separate from the bearing. Sometimes bearing faults are considered as rotor asymmetry faults, which are usually covered under the eccentricity-related faults. Bearing failures are reported frequently by industry. Different techniques for a joint time-frequency analysis and an experimental study of detection and diagnosis of

damaged bearings on a PMSM have been investigated in [44]. When the motor is running under non-stationary conditions, the conventional signal processing methods such as FFT in Motor Current Signature Analysis (MCSA) do not work well. Under such conditions, the stator current can be analyzed by means of STFT and Gabor Spectrogram for detecting the bearing damage.

Another diagnosis method for detecting bearing faults in PMSMs, based on frequency response analysis is proposed in [45]. The torque and velocity signals of the machine are periodically disturbed when the bearing is damaged. These disturbances cause the frequency response of the mechanical system to change at specific frequencies. Utilizing the velocity of the motor and the torque generating component of the stator current (i_q), the frequency response of the machine in the closed loop speed control can be derived. The frequency response analysis proposed by this method yields more reliable fault detection results than the FFT analysis.

1.4 Research Objectives

The purpose of the research presented in this dissertation is to analyze damper winding failures in synchronous machines and the effect of faults and their severity on the current spectrum during transient and steady state operations.

The first objective is to develop a novel computer model of synchronous machine to simulate various broken damper bar scenarios. The second objective is to build a synchronous motor and experimental setup to stage various types of broken bar experiments. The third objective is to investigate and adapt existing non-invasive

induction motor rotor failure detection methods for detection of broken damper bar failures in synchronous machines using the experimental and simulation data. The last objective is to develop a novel analytical method using electromagnetic field theory to explain the effect of broken bars on the current spectrum in induction machines as well as synchronous machines and to justify the simulation and experimental results.

The modeling of synchronous machines using winding function approach has been reported in the literature without including a damper winding, which is valid only at the steady state operation. When including a damper winding in the model, the machine behavior at transient as well as steady state can be studied. The equations describing the three sets of mutually coupled circuits; stator, field and damper windings are presented in section 2. A method of modeling the skewed rotor is presented and a general electromagnetic torque equation generated by interaction of armature, field and damper currents is presented.

In section 3, an analysis of the armature current spectrum during transient and steady state operations is presented. At synchronous speed, the damper winding has no effect on the motor operation because it has the same speed as the air gap rotating field and no current is induced in the damper winding. Therefore, if a defective damper winding leaves a faulty signature on the armature current spectrum it can be either during transient or at asynchronous steady state operation. The possible transient operations are at the startup transient, the field excitation transient, and the load change transient. For current spectrum analysis during transients, the Short Time Fourier Transform (STFT) is employed.

Asynchronous steady state operation is achieved at startup when the armature winding is connected to the source but the field winding is left open. Under this condition, the motor operates as an induction motor and the torque is produced only by interaction of the armature winding and the damper winding currents. In the induction mode of operation, the rotor cannot reach the synchronous speed and has a constant slip at steady state. For the broken damper bar signature analysis in the asynchronous steady state mode of operation, the well known Fast Fourier Transform (FFT) is used.

In section 4, experimental results are presented and compared with simulation results. For the experimental set up, an inverted round rotor synchronous machine with damper winding was designed. The armature windings of the inverted motor were wound on the rotor, connected to the supply via slip rings, and its field winding was mounted in some of the stator slots. The copper bars of the damper cage were placed in the remaining stator slots aligned with the pole faces. The end ring was fixed on one side and removable on the other side. This makes it possible to disconnect any of the bars from the end ring for a broken bar test.

Despite the operational similarity between a of synchronous machines with broken damper bars in the asynchronous steady state operation and the cage rotor induction machines with broken rotor bars, the fault signatures are not quite similar. Due to the structure of a damper winding, which often looks like an incomplete cage, a healthy damper winding behaves as a broken cage, leaving a fault-like signature on the current spectrum. This makes the diagnostic of broken damper bars a challenging task. For diagnosis of damper winding failures it is not adequate to detect the present of a

fault-like signature since it exists in healthy cases too. Fault diagnosis requires further knowledge about the magnitude of the fault components in the current spectrum. In section 5, a novel analytical approach is presented to analyze the variation of the magnitudes of the sideband components known as the fault signatures in the current spectrum. The proposed analytical method is based on rotating field theory and the characteristics of an unbalanced multiphase system. Section 6 summarizes the findings and conclusions of work.

1.5 Conclusions

In this section, a summary of different types of failures in induction and synchronous machines have been discussed, and machine failure diagnosis techniques proposed in the literature have been presented. The research objectives and the outline of this dissertation are stated.

2. MODELING OF SYNCHRONOUS MACHINES WITH DAMPER WINDINGS

2.1 Introduction

This section deals with a new method for modeling of synchronous machines with damper windings using the winding function approach (WFA). This method of machine analysis with the actual winding distribution does not require neglecting the harmonics of the stator winding distribution. The proposed model is capable of simulating various fault conditions such as broken damper bars, broken end rings, eccentricities and inter-turn faults. Given the geometry of the machine and its winding configuration, all of the inductances are calculated as a function of the rotor positions. The skew effect is included in defining the winding functions and the calculation of the inductances.

To produce torque in synchronous machines, the rotor must be turning at the same speed as the stator field (i.e., synchronous speed). At any other speed, the rotating field of stator poles will be moving past the rotor poles, first attracting and then repelling them. This condition results in zero average torque and the machine will not start. Using a dc motor or a damper winding, the machine can be brought up to the synchronous speed. A damper winding consists of heavy copper bars, with the two ends shorted together, installed in slots of the rotor pole faces. The interaction of the currents induced in the bars by the rotating air-gap field produces torque. In other words, the

machine is started as an induction motor [46]. The dc field current is turned on when the machine is brought near the synchronous speed. When the load is suddenly changed, the damper winding helps damping out the oscillatory motion superimposed on the normal synchronous rotation of the shaft.

Diagnostic of broken damper bars in synchronous machines has not been studied as widely as the other faults like eccentricity and inter-turn faults [47], [48]. In most operational conditions, when the machine speed is not changed very often, this fault is less frequently reported compared to the other faults. At startup, the electromagnetic behavior of asynchronous machines with a damper winding is similar to that of an induction machine. During transient times, when the machines accelerate from zero speed to synchronous speed, significant current flows in the damper winding.

Excessive start-stop cycles or frequent speed changes can cause the breakage of the damper bars. When a bar breaks most of the current that would have flown in that bar now flows in the two bars immediately adjacent to it on either side. This could result in breakage of several bars [49].

In the development of the d-q model of synchronous machines, it is assumed that the stator windings are sinusoidally distributed [50]. In other words, all harmonics of the stator winding distribution are neglected. In the proposed model however, the machine is simulated in the natural reference frame. That is, the machine is simulated in terms of the actual physical rather than transformed or equivalent variables. The coupled magnetic circuit approach is used to derive a synchronous machine model with *m* phase stator windings, one field winding and *n* rotor bars.

2.2 Stator Voltage Equations

The analysis described in this subsection is developed in a general form which is applicable to any type of single or multi-phase motor with any winding configuration. Consider a synchronous machine with *m* stator windings, a field winding and *n* damper bars. Taking into account the damper winding end rings, there will be *m+n+2* independent circuits which are magnetically coupled to each other. These equations are written in three sets of matrix equations.

The voltage equations for the stator circuits can then be written as:

$$V_s = R_s I_s + \frac{d\Lambda_s}{dt} \tag{2.1}$$

where the stator flux linkages are given by:

$$\Lambda_s = L_s I_s + L_{sf} I_f + L_{sd} I_d \tag{2.2}$$

V_s and I_s are vectors of the armature voltages and currents and can be written as:

$$V_s = [v_{s1} \quad v_{s2} \quad \cdots \quad v_{sm}]^t \tag{2.3}$$

$$I_s = [i_{s1} \quad i_{s2} \quad \cdots \quad i_{s,m}]^t \tag{2.4}$$

I_f, is the field current and I_d is the vector of the damper bars and end ring currents which can be presented by:

$$I_f = [i_f] \tag{2.5}$$

$$I_d = [i_{d1} \quad i_{d2} \quad \cdots \quad i_{d,\ n+1}]^t \tag{2.6}$$

R_s is a diagonal *m* by *m* matrix given by:

$$R_s = r_s\, I \tag{2.7}$$

where, I is an m by m identity matrix and r_s is the resistance of each stator coil assuming all coils are similar. Inductance matrix L_s is a symmetric m by m matrix of the form:

$$L_s = \begin{bmatrix} l_{s1s1} + l_s & l_{s1s2} & \cdots & l_{s1sm} \\ l_{s2s1} & l_{s2s2} + l_s & \cdots & l_{s2sm} \\ \vdots & \vdots & \ddots & \vdots \\ l_{sms1} & l_{sms2} & \cdots & l_{smsm} + l_s \end{bmatrix} \tag{2.8}$$

where, l_s is the leakage inductance of an armature winding. The diagonal terms are the magnetizing inductances and off-diagonal terms are the mutual inductances of armature windings.

L_{sf} is an *m* by 1 matrix comprised of the mutual inductances between the armature coils and the field winding:

$$L_{sf} = [l_{s1f} \quad l_{s2f} \quad \cdots \quad l]^t \tag{2.9}$$

L_{sd} is an *m* by *n+1* matrix consists of the mutual inductances between the armature coils and the damper windings:

$$L_{sd} = \begin{bmatrix} l_{s1d1} & l_{s1d2} & \cdots & l_{s1dn+1} \\ l_{s2d1} & l_{s2d2} & \cdots & l_{s2dn+1} \\ \vdots & \vdots & \ddots & \vdots \\ l_{smd1} & l_{smd2} & \cdots & l_{smdn+1} \end{bmatrix} \tag{2.10}$$

2.3 Field and Damper Winding Equations

The field and damper windings are normally located on the rotor of the synchronous machine. A mesh model is used to derive the damper winding equations. Each mesh consists of two adjacent bars and the end ring segments that join them. The

field winding is coupled with m stator windings and *n+1* damper loops. The voltage equation for the field winding is:

$$V_f = R_f I_f + \frac{d\Lambda_f}{dt} \tag{2.11}$$

where, the field flux linkage is given by:

$$\Lambda_f = L_{fs} I_s + L_f I_f + L_{fd} I_d \tag{2.12}$$

R_f is the field winding resistance, L_f is self inductance of the field winding, $L_{fs} = L^t_{sf}$ is the matrix of the mutual inductances between the field and the stator windings, and L_{fd} is the matrix of the mutual inductances between the field and damper windings:

$$L_{fd} = [l_{fd1} \quad l_{fd2} \quad \dots \quad l_{fdn+1}] \tag{2.13}$$

The damper winding which consists of n bars and two end rings can be treated as *n+1* meshes with independent voltage equations. The damper voltage equations can be written as:

$$V_d = R_d I_d + \frac{d\Lambda_d}{dt} \tag{2.14}$$

where the damper winding flux linkage is given by:

$$\Lambda_d = L_{ds} I_s + L_{df} I_f + L_d I_d \tag{2.15}$$

R_d is an n+1 by n+1 matrix of the damper winding resistances and L_d is an n+1 by n+1 matrix of the self and the mutual inductances between damper loops including the end ring. $L_{ds} = L^t_{sd}$ is the matrix of the mutual inductances between the damper and the stator windings, and $L_{df} = L^t_{fd,}$ is the matrix of the mutual inductances between the field and damper windings.

In general the damper bars are not uniformly distributed on the cage, leading to unequal meshes and unequal mesh currents. In most cases the end ring is continuous, which makes an additional loop in the damper circuit. Therefore, there will be *n+1* independent voltage equations associated with the damper winding. It should be noted that the damper mesh currents are not the actual currents flowing in the bars. Each bar current can be obtained by subtracting the two mesh currents sharing that bar. The coefficients of the mesh currents in the damper equations make the resistance matrix R_d and the coefficients of the derivatives of the mesh currents make the inductance matrix L_d. Assuming *2k-1* bars per pole and bar #1 located in the middle of the first pole, the k^{th} mesh equation corresponds to a big mesh between two poles with a larger resistance r_{eq} and leakage inductance L_{eq}.

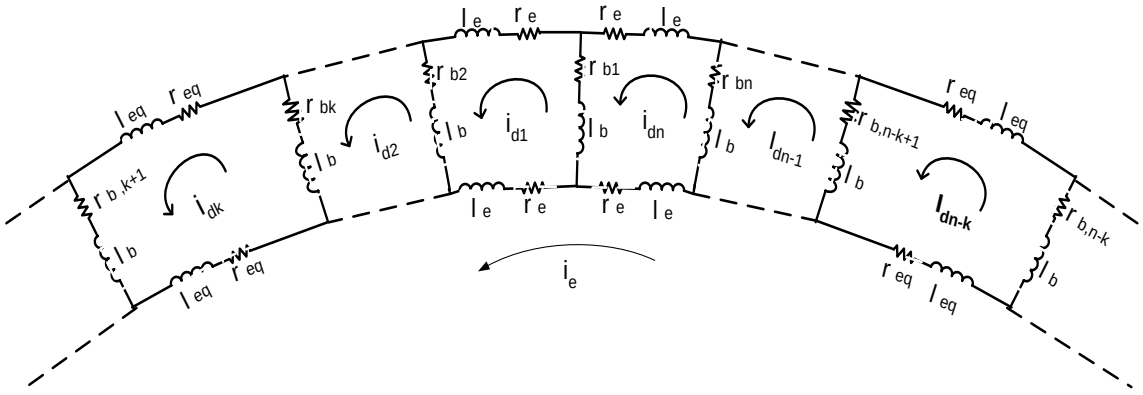

Figure 2.1 Damper winding circuit model used to derive R_d and L_d matrices.

Fig. 2.1 shows the mesh model for the damper winding used in deriving the two matrices R_d and L_d. In this model each mesh is treated as a single phase winding. A voltage equation for each mesh can be written. The coefficients of the mesh currents define the damper resistance matrix R_d in the damper matrix equation:

$$R_d = \begin{bmatrix} r_{b1}+r_{b2}+2r_e & -r_{b2} & \cdots & 0 & 0 & 0 \\ -r_{b1} & r_{b2}+r_{b3}+2r_e & \cdots & 0 & 0 & 0 \\ \vdots & \vdots & \ddots & \vdots & \vdots & \vdots \\ 0 & 0 & \cdots & -r_{b,k-1} & r_{bk}+r_{b,k+1}+2r_{eq} & -r_{b,k+1} \\ \vdots & \vdots & \ddots & \vdots & \vdots & \vdots \\ -r_{b1} & 0 & \cdots & 0 & 0 & \cdots \\ -r_e & -r_e & \cdots & -r_e & -r_{eq} & -r_e \end{bmatrix}$$

$$\begin{bmatrix} \cdots & -r_{b,n} & -r_e \\ \cdots & 0 & -r_e \\ \ddots & \vdots & \vdots \\ \cdots & 0 & -r_{eq} \\ \ddots & \vdots & \vdots \\ -r_{b,n-1} & r_{b1}+r_{bn}+2r_e & -r_e \\ \cdots & -r_e & (n-p)r_e+p.r_{eq} \end{bmatrix} \qquad (2.16)$$

P is the number of poles, r_{bi} is the resistance of the i^{th} bar, r_e is the end ring resistance of a small segment between the bars and r_{eq} is the end ring resistance of the big segments. Different bar resistances are used in the equations in order to be able to assign a large value to the broken bars when simulating the faulty cases. With this model, any fault situation in terms of the number and location of broken bars can be easily implemented.

$$L_d = \begin{bmatrix} l_{1,1}+2l_b+2l_e & l_{1,2}-l_b & \cdots & l_{1,k-1} & l_{1,k} & l_{1,k+1} \\ l_{2,1}-l_b & l_{2,2}+2l_b+2l_e & \cdots & l_{2,k-1}-l_b & l_{2,k} & l_{2,k+1} \\ \vdots & \vdots & \ddots & \vdots & \vdots & \vdots \\ l_{k,1} & l_{k,2} & \cdots & l_{k,k-1}-l_b & l_{k,k}+2l_b+2l_{eq} & l_{k,k+1}-l_b \\ \vdots & \vdots & \ddots & \vdots & \vdots & \vdots \\ l_{n,1}-l_b & l_{n,2} & \cdots & l_{n,k-1} & \vdots & \vdots \\ -l_e & -l_e & \cdots & -l_e & -l_{eq} & -l_e \end{bmatrix}$$

$$\begin{bmatrix} \cdots & l_{1,n}-l_b & -l_e \\ \cdots & l_{2,n} & -l_e \\ \ddots & \vdots & \vdots \\ \cdots & l_{k,n} & -l_{eq} \\ \ddots & \vdots & \vdots \\ l_{n,n-1}-l_b & L_{n,n}+2l_b+2l_e & -l_e \\ \cdots & -l_e & (n-p)l_e+p.l_{eq} \end{bmatrix} \quad (2.17)$$

The damper inductance matrix which consists of the coefficients of the derivatives of the mesh currents is derived in (2.17) where, l_e is the leakage inductance of the small segments and l_{eq} is the leakage inductance of the big segments on the end ring. $l_{i,i}$ is the magnetizing inductance of loop i, l_b is the leakage inductance of each bar, and $L_{i,j}$ is the mutual inductance between loop i and j.

The n damper mesh currents are coupled to each other, to the stator and the field windings, through the mutual inductances. However, there is no mutual inductance between the end ring and any other windings.

2.4 Derivation of the Torque Equation

The mechanical equation of motion depends upon the characteristics of the load and is given by:

$$J\frac{d^2\theta_{rm}}{dt^2} + T_l = T_e \tag{2.18}$$

where, J is the moment of inertia of rotor, θ_{rm} is the angular displacement of the rotor, T_ℓ is the load torque, and T_e is the electromagnetic torque produced by the machine. The electrical torque can be found from the magnetic co-energy W_{co}:

$$T_e = \left[\frac{dW_{co}}{d\theta_{rm}}\right]_{(I_s,\ I_f\ ,\ I_d\ constant)} \tag{2.19}$$

In a linear magnetic system, the co-energy is equal to the stored magnetic energy in all of the inductances. Therefore, with three inductance matrices of the machine co-energy can be expressed as:

$$W_{co} = \frac{1}{2}\begin{bmatrix} I_s^t & I_f^t & I_d^t \end{bmatrix}\begin{bmatrix} L_s & L_{sf} & L_{sd} \\ L_{fs} & L_f & L_{fd} \\ L_{ds} & L_{df} & L_d \end{bmatrix}\begin{bmatrix} I_s \\ I_f \\ I_d \end{bmatrix} \quad (2.20)$$

After carrying out the matrix multiplication, w_{co} is simplified as:

$$W_{co} = \frac{1}{2}\ (I_s^t\ L_s\ I_s + I_f^t\ L_{fs}\ I_s + I_d^t\ L_{ds}\ I_s + I_s^t\ L_{sf}\ I_f + I_f^t\ L_f\ I_f + I_d^t\ L_{df}\ I_f +$$

$$I_s^t\ L_{sd}\ I_d + I_f^t\ L_{fd}\ I_{fd} + I_d^t\ L_d\ I_d) \quad (2.21)$$

In general, if the slot effect is to be considered, the inductance matrices in this equation are not constant and the co-energy equation cannot be further simplified. To derive an expression for the electromagnetic torque, the derivative of W_{co} with respect to the rotor mechanical angle must be taken, assuming all currents are constant.

$$T_e = \frac{1}{2}\left(I_s^t \frac{dL_s}{d\theta_{rm}} I_s + I_f^t \frac{dL_f}{d\theta_{rm}} I_f + I_d^t \frac{dL_d}{d\theta_{rm}} I_d\right) + I_f^t \frac{dL_{fs}}{d\theta_{rm}} I_s + I_d^t \frac{dL_{ds}}{d\theta_{rm}} I_s + \frac{dL_{df}}{d\theta_{rm}} I_f \quad (2.22)$$

2.5 Setting up the Machine System of Equations

Given the stator, field and damper voltage equations, the differential equations can be set up to solve for the currents. Damper voltages are zero since the bars are shorted together. The following equations must be solved simultaneously to obtain all the currents.

$$I = L^{-1}\Lambda \quad (2.23)$$

$$\frac{d\Lambda}{dt} = V - RI \quad (2.24)$$

$$\frac{d\omega}{dt} = \frac{1}{J}\ (T_e - T_L) \quad (2.25)$$

$$\frac{d\theta_{rm}}{dt} = \omega \quad (2.26)$$

Each of the current, voltage and flux vectors consists of m+n+2 entries. The first m entries correspond to the stator windings, the next one is for the field winding and the last n+1 entries correspond to the damper winding. These matrices are defined as follows:

$$I = [I_s \quad I_f \quad I_d]^t \tag{2.27}$$

$$V = [V_s \quad V_f \quad V_d]^t \tag{2.28}$$

$$\Lambda = [\Lambda_s \quad \Lambda_f \quad \Lambda_d]^t \tag{2.29}$$

The m+n+2 by m+n+2 matrices of the machine resistances and inductances are given by:

$$R = \begin{bmatrix} R_s & 0 & 0 \\ 0 & R_f & 0 \\ 0 & 0 & R_d \end{bmatrix} \tag{2.30}$$

$$L = \begin{bmatrix} L_s & L_{sf} & L_{sd} \\ L_{fs} & L_f & L_{fd} \\ L_{ds} & L_{df} & L_d \end{bmatrix} \tag{2.31}$$

All inductances in matrix L and the derivatives in (2.22) will be obtained using the winding function approach which will be discussed in the next subsection. These values are calculated at the beginning as a function of rotor position θ_{rm} and saved over one revolution. When solving the differential equations the inductance corresponding to each rotor position θ_{rm} will be used.

2.6 Winding Function Theory

Winding function theory is a method of calculating the self and mutual inductances of one or two circuits magnetically coupled together. This method is established based on Ampere's law and Gauss's law [50]. In derivation of this theory, the relative permeability of the iron was assumed to be infinity, i.e. the magneto-motive force (MMF) drop in the iron was neglected. The MMF distribution created by each winding in the air gap can simply be found by the product of the winding function and the current flowing in the winding:

$$F_A(\emptyset, \theta) = N_A(\emptyset, \theta)\ i_A \tag{2.32}$$

where, F_A is the MMF distributed in the air gap due to the current in the stator coil *A*, i_A, N_A is the winding function of coil *A*, θ is the angular position along the stator inner surface and ϕ is the angular rotor position with respect to any stator reference point.

The winding function of each coil represents the cumulative number of turns over a complete turn. Looking into the cross section of a coil winding arrangement around the periphery of the motor, the turns carrying inward current are considered positive turns and the turns carrying outward current are considered negative turns. The flux in a magnetic circuit is the product of the MMF and the permeance (P) of the flux path.

$$\Phi = F\ P \tag{2.33}$$

And, the permeance is given by:

$$P = \frac{\mu A}{l} \tag{2.34}$$

where, μ is the permeability, *A* is the cross sectional area and *l* is the length of the magnetic path. The differential flux across the gap through a differential volume $r.L.d\phi$ is:

$$d\emptyset = F_A(\emptyset,\theta)\mu_0\ r\ L\ \frac{d\emptyset}{g(\emptyset,\theta)} \tag{2.35}$$

The flux linking the coil section 1-1' of winding *B* can be calculated using the following integration:

$$\Phi_{1-1'} = \mu_0\ r\ L\ \int_0^{2\pi} n_{B1}(\emptyset,\theta).F_A(\emptyset,\theta).g^{-1}(\emptyset,\theta)d\emptyset \tag{2.36}$$

where, n_{B1} is the number of turns in coil section 1-1' between the angles ϕ1 and ϕ1'and is zero elsewhere. Coil side 1' is the return path of coil side 1. This process is repeated to calculate the flux linking the other coil sides of winding *B*. In general for the coil side k-k', the flux linkage will be:

$$\Phi_{k-k'} = \mu_0\ r\ L\ \int_0^{2\pi} n_{Bk}(\emptyset,\theta).F_A(\emptyset,\theta).g^{-1}(\emptyset,\theta)d\emptyset \tag{2.37}$$

The total flux linking winding B due to current in winding *A* can be expressed as:

$$\lambda_{BA} = \sum_{k=1}^{q_i}\Phi_{k-k'} = \mu_0\ r\ L\ \left[\sum_{k=1}^{q_i}\int_0^{2\pi} n_{Bk}(\emptyset,\theta).F_A(\emptyset,\theta).g^{-1}(\emptyset,\theta)d\emptyset\right] \tag{2.38}$$

This can be simplified in the form of:

$$\lambda_{BA} = \mu_0\ r\ L\ \int_0^{2\pi}\left[\sum_{k=1}^{q_i} n_{Bk}(\emptyset,\theta)\right].F_A(\emptyset,\theta).g^{-1}(\emptyset,\theta)d\emptyset \tag{2.39}$$

where the expression inside the bracket is the turns function of winding *B*, $n_B(\phi,\theta)$.

$$n_B(\emptyset,\theta) = \sum_{k=1}^{q_i} n_{Bk}(\emptyset,\theta) \tag{2.40}$$

and q_i is the number of series connected coil sections. Now the mutual inductance L_{BA} of winding *B* due to the current in winding *A* can be written as:

$$L_{BA} = \frac{\lambda_{BA}}{i_A} = \mu_0 \, r \, L \int_0^{2\pi} N_B(\emptyset,\theta).N_A(\emptyset,\theta).g^{-1}(\emptyset,\theta)d\emptyset \quad (2.41)$$

The winding function N_B is obtained by subtracting the average of n_B from n_B.

$$N_B = n_B - \int_0^{2\pi} n_B(\emptyset,\theta)\,\mathrm{d}\theta \quad (2.42)$$

Similarly, the magnetizing inductance of winding *A* can be calculated.

$$L_{AA} = r \, L \int_0^{2\pi} N_A(\emptyset,\theta).N_A(\emptyset,\theta).g^{-1}(\emptyset,\theta)d\emptyset \quad (2.43)$$

2.7 Calculation of Inductances Using Winding Function Approach

All of the inductances for solving the machine equations can be calculated using the winding function approach (WFA) described in subsection 2.4. First the winding functions corresponding to all stator, field and damper windings as well as the air gap function need to be defined according to their winding arrangements. Then using (2.41) and (2.43), all of the magnetizing and mutual inductances will be given as functions of the rotor position. In this research, a round rotor 3-phase, 4-pole synchronous machine with 24 rotor slots and 36 stator slots and a damper cage with 20 bars was used for simulations and experiments. It is to be noted that this machine is an inverted machine such that the armature windings are mounted on the rotor and the field and damper windings are mounted on the stator. The 3-phase, 4-pole armature winding configuration (rotor) is shown in Fig. 2.2. Each armature coil occupies two slots per pole per phase. The cross represents an inward direction and the dot represents an outward direction of the currents in the windings. The armature winding arrangements in 24 slots along with the turns function of winding *A* and the winding functions of

windings *A*, *B* and *C* are shown in Fig. 2.3. The turns function shows the number of turns as a function of θ, and the winding function is the turns function minus its average.

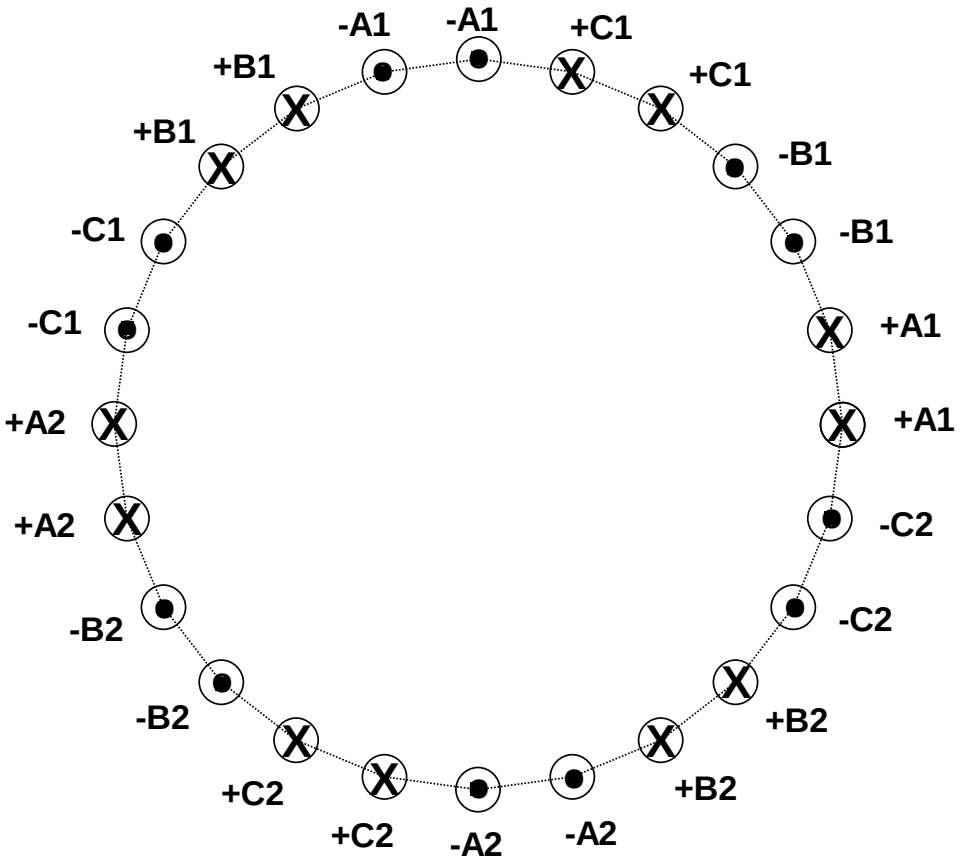

Figure 2.2 Configuration of the armature winding mounted on the rotor.

For more realistic winding functions, it was assumed that the windings are not concentrated at one point and are distributed uniformly in the slots. Therefore, the winding function which represents the number of turns increases or decreases linearly by

n_s over the width of the slot as shown in Fig. 2.3. In this figure, n_s represents the number of turns in each slot and skew effect is not included.

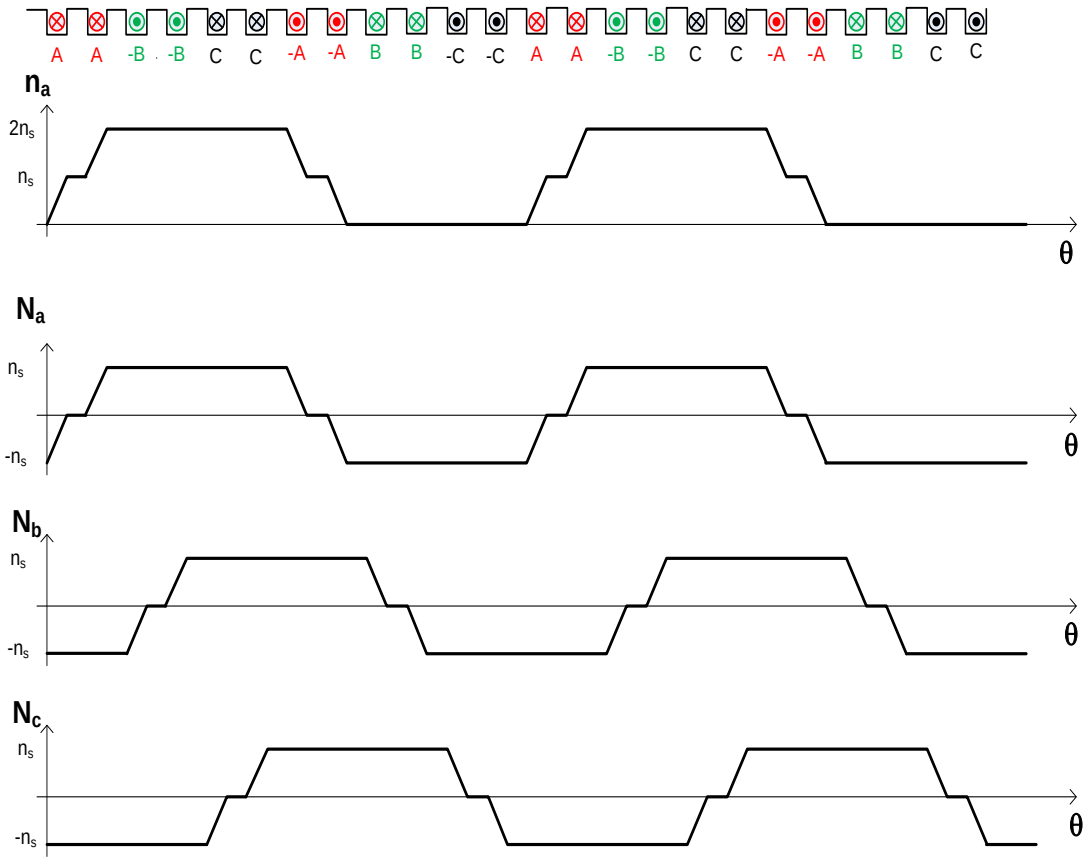

Figure 2.3 Winding functions. From top figure to bottom: winding arrangements in the slots, turns function of winding A, winding functions of windings A, B and C.

2.8 Skew Effect on the Winding Function

In rotating electrical machines, especially in squirrel cage induction motors, the stator and rotor slots are often assembled in a skew position with respect to each other in order to reduce the influences of the permeance harmonics caused by slots. The

objective of skewing is to reduce the ability of certain air gap harmonics created by stator, to induce respective voltages in the rotor bars.

In the case of the inverted synchronous machine under study, the rotor slots holding the armature windings are skewed by one slot. To show the effect of skewing on the winding function, consider the cross section of a rotor with the slot pitch α and skew angle sk as shown in Fig. 2.4. In this figure only one winding is shown and magnified in size. If the skew angle is zero and the rotor slots are straight, looking at the cross section of the rotor, the winding distribution in one slot starts at θ_1 and ends at $\theta_1+ \alpha$. However, in the case of the skewed slots, the winding distribution starts at the same angle θ_1 but ends at $\theta_1+ \alpha+sk$. In both cases, the same number of turns exist over one effective slot. The same discussion applies to the return path of the winding.

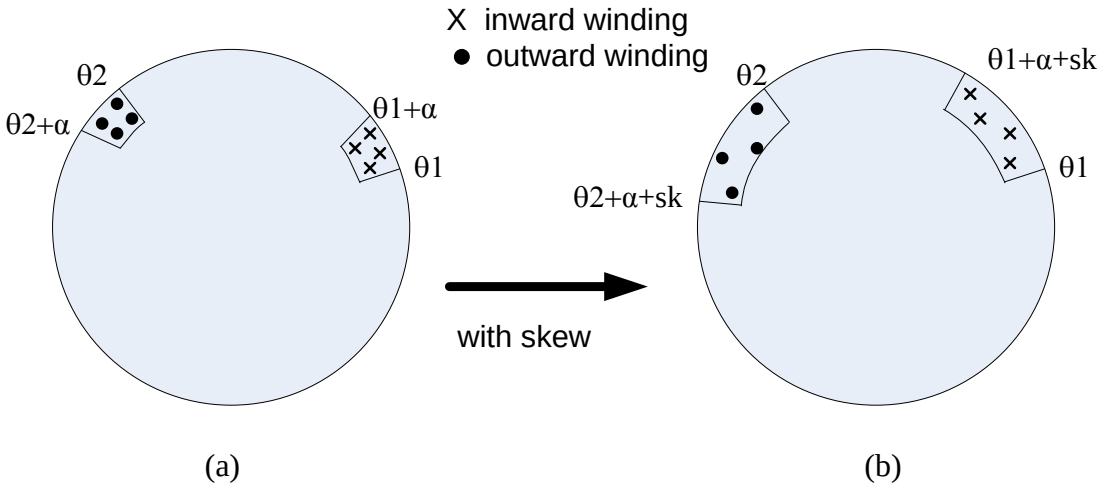

Figure 2.4 Cross section of a rotor showing the effective distribution of a winding in the slots. a) no skewing, b) with skew.

Using the proposed model of the skewing effect on the winding distribution, the winding functions for the three armature windings shown in Fig. 2.3 will be changed to the new winding functions in Fig. 2.5. To obtain the turns functions with the skewing effect, the turns function of the coil in each slot needs to be considered separately. For example consider the turns function n_{A1} for the first coil of phase *A* in the first slot. The turns function corresponding to this coil starts at zero with zero turns and increases linearly to n_s over one slot pitch plus the skew angle. It stays constant up to the ^{8th} slot which holds the return path of the same coil. At this point it decreases to zero, over one slot pitch plus the skew angle. The turns function n_{A2} for the second coil of phase *A*, starts at second slot with zero turns and increases to n_s over one slot pitch plus the skew angle, and at the 7^{th} slot returns to zero over the same distribution angle. To find the turns function n_A for phase *A*, the contributions of all coils of this phase need to be added. By subtracting the average of the turns function from itself, the winding function of phase *A*, with skewing effect is obtained. For a balanced three phase winding the winding functions of the other two phases can be found by phase shifting the phase winding function by $+2\pi/3$ and $-2\pi/3$.

When skewing is included in the model, the winding function will be in the trapezoidal form which is closer to the ideal sinusoidal function. To improve the winding function which represents the MMF, and make it closer to the actual MMF in the machine, each positive or negative ramp in the winding function is smoothed out using a sinusoidal approximation. A ramp function with a change of value from α_1 to α_2 between θ_1 and θ_2, can be approximated by a sinusoidal function $f(\theta)$.

$$f(\theta) = \alpha_1 - \frac{\alpha_2 - \alpha_1}{2}\left[\cos\left(\frac{\theta-\theta_1}{\theta_2-\theta_1}\,\pi\right) - 1\right] \tag{2.44}$$

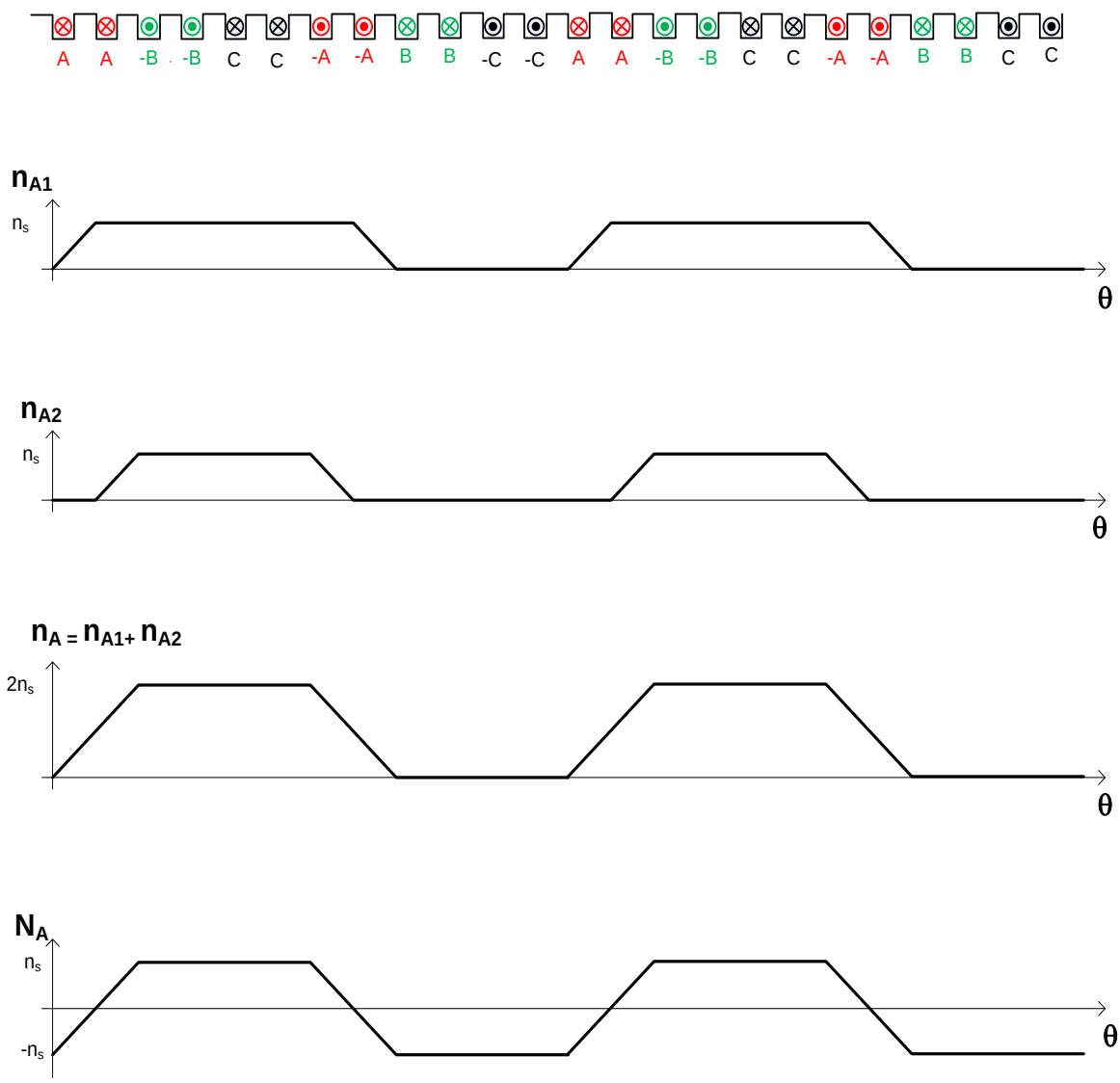

Figure 2.5 Effect of skewing on winding function. From top figure to bottom: winding arrangements in the slots, turns function of first coil of phase A, turns function of second coil of phase A, total turns function of phase A, winding function of phase A.

The field winding configuration is shown in Fig. 2.6. This winding is mounted on the stator and all are connected in series. The winding order and direction is as follows:

1-1’-2-2’-3-3’- … -8-8’.

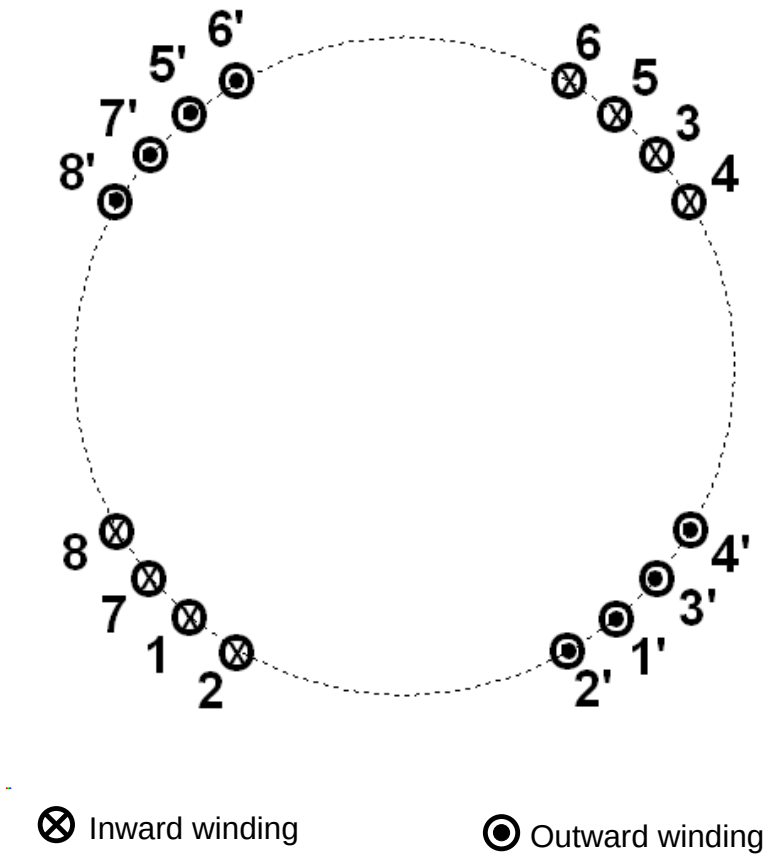

Figure 2.6 Configuration of the field winding mounted on the stator.

The damper winding with 20 bars (5 bars per pole) is shown in Fig. 2.7. The bars are shorted together with two end rings. Both field and damper windings are mounted on the stator.

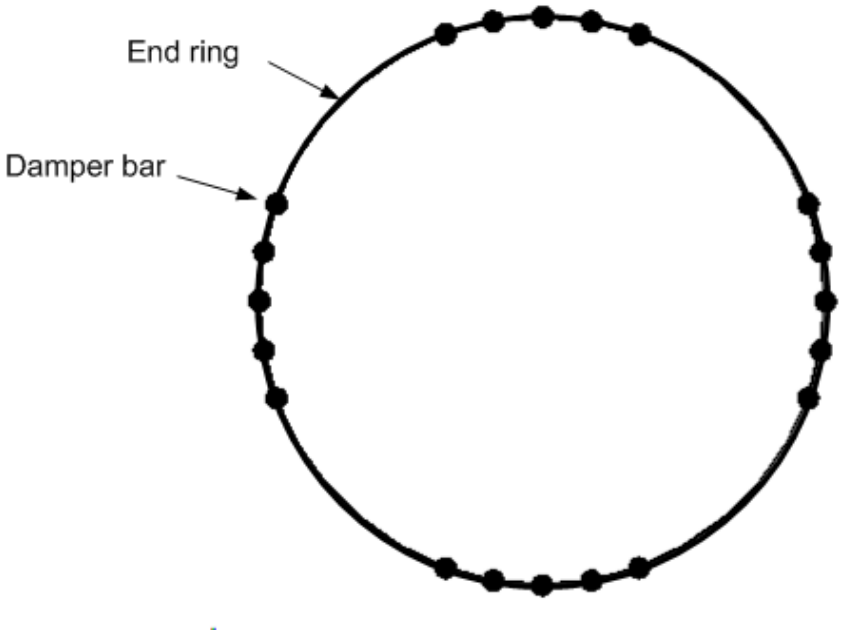

Figure 2.7 Damper winding configuration.

The winding functions of field and damper windings can be obtained using the same method described for the armature windings. Field and damper windings are not skewed but the ramps in the trapezoidal winding functions can be rounded up using sinusoidal approximation in (2.44).

To calculate all of the magnetizing and mutual inductances, the air gap function g must also be defined. The air gap function is the effective gap width as a function of θ over 2π radians. Since this is a round rotor synchronous machine, the gap function is

constant if the slot effect on the air gap is neglected. Now that all winding functions for 3 stator windings, one field winding and 20 damper meshes are known and the gap function is constant, it is possible to calculate all of the machine inductances using (2.41) and (2.43) at each rotor position ϕ. Since the gap is constant if the slot effect is neglected, some of the inductances will be independent of ϕ.

2.9 Matlab Program for Solving Machine Equations

The winding function method discussed in the subsection 2.6 for calculation of the machine inductances along with the machine equations (2.22) - (2.26) are used to develop a Matlab program for simulating the synchronous machine under healthy and faulty conditions. The flowchart showing the iterative process of solving the machine equations is presented in Fig. 2.8. In this program, all winding functions corresponding to the stator, field and damper windings are defined as a function of stator angle θ according to their winding layouts. Then using equations (2.41) and (2.43) the magnetizing and mutual inductances are calculated over one complete revolution of the rotor. Each inductance as a function of the angular rotor position is saved in a matrix to be used when solving the machine equations. These equations given by (2.22) - (2.26) are solved iteratively and in each iteration the rotor position ϕ is found by taking the derivative of the rotor speed ω. Based on the new rotor position, the inductance matrices are updated to be used in the next iteration.

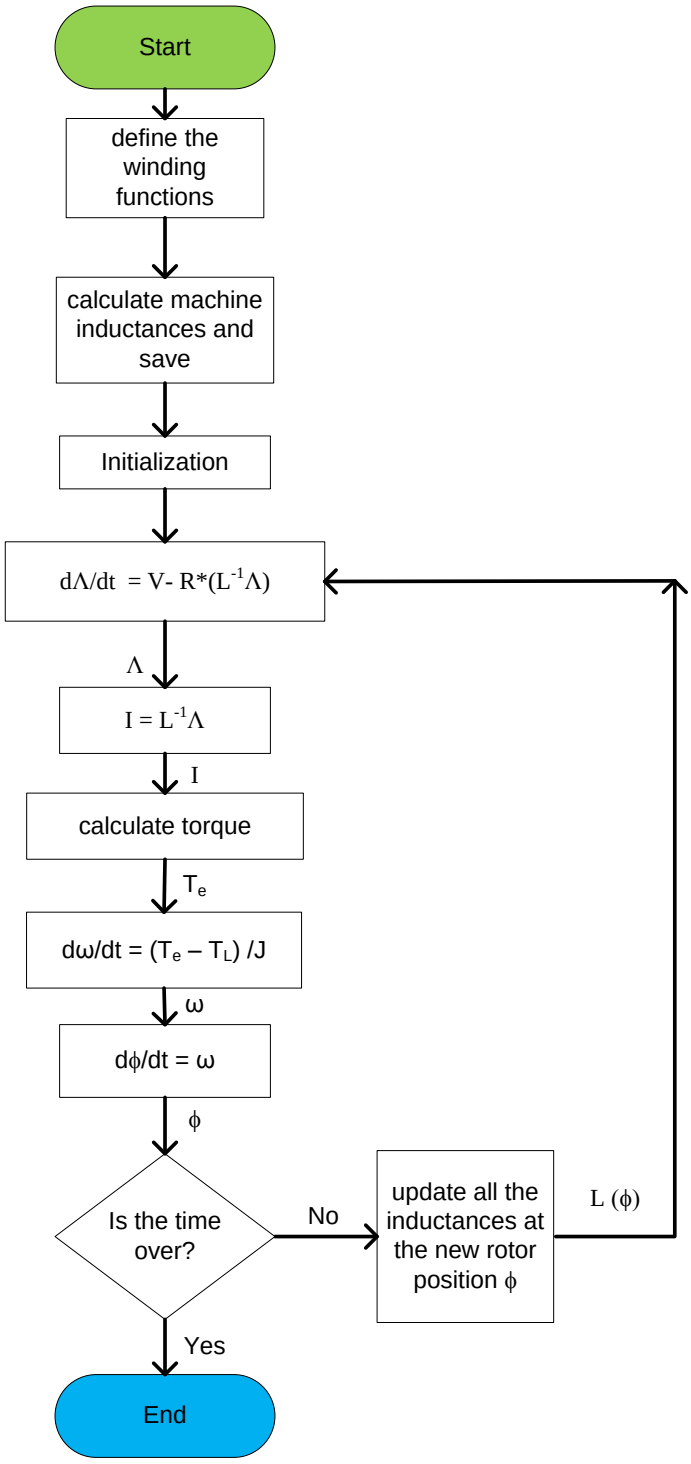

Figure 2.8 Flowchart of the iterative procedure for solving machine equations.

2.10 Calculated Inductances

The output waveforms of the Matlab program will be presented in this subsection. First let's examine the effect of including the rotor skewing on the armature winding functions. As discussed in subection 2.6, a skewed rotor can be modeled by extending the effective slot pitch by the skew angle. As shown in Fig. 2.9, when skewing effect is included in the model, the winding functions will be smoother leading to the reduced MMF harmonics. The ramp transitions of the winding functions are smoothened with sinusoidal approximation given by (2.44) to resemble the actual MMF.

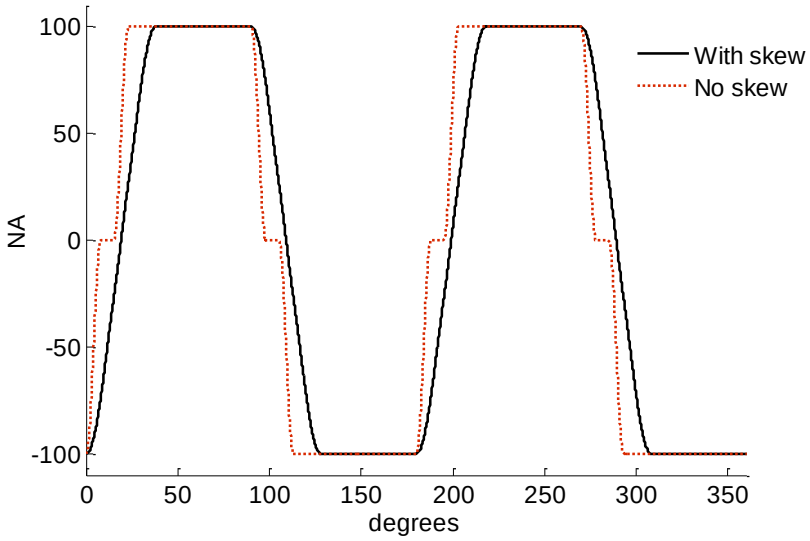

Figure 2.9 Armature winding function N_A with and without skewing.

The field winding layout in Fig. 2.6, which consists of 8 series connected coils and 100 turns per slot, has a winding function as shown in Fig. 2.10.

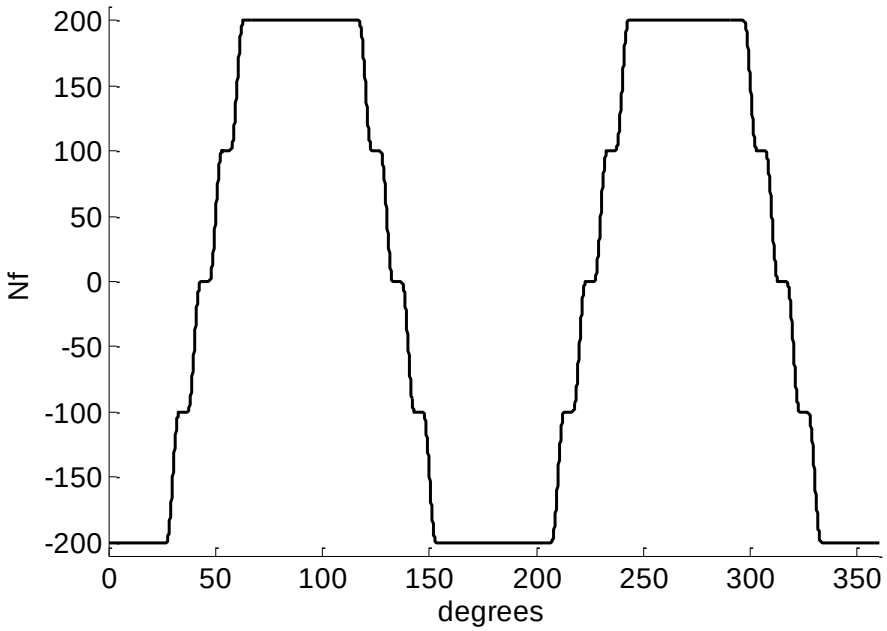

Figure 2.10 Field winding function N_f.

The damper winding has 20 meshes, each comprised of two adjacent bars and two end ring segments. Each mesh can be treated as a single turn winding with its own winding function. As shown in Fig. 2.11 (b), mesh #1, which is composed of bar #1, bar #2 and two end ring segments, is smaller than mesh #3. Therefore, the damper meshes do not have identical winding functions. Fig. 2.11 (a) shows the winding functions of the first three meshes.

Since the gap function is constant, for the round rotor, all the magnetizing inductances are constant and independent of the rotor position (ϕ). For the same reason the mutual inductances between 3 armature windings (L_{AB}, L_{BC}, L_{CA}), 20 damper meshes ($L_{d1,2}$, $L_{d1,3}$, …) and between field and damper windings ($L_{f,d1}$, $L_{f,d2}$, ..., $L_{f,d20}$)

are zero. The other inductances are functions of the rotor position. The mutual inductances between three armature windings and the field winding, shown in Fig. 2.12, are almost sinusoidally varying. They are identical functions phase shifted by $2\pi/3$ electrical angle.

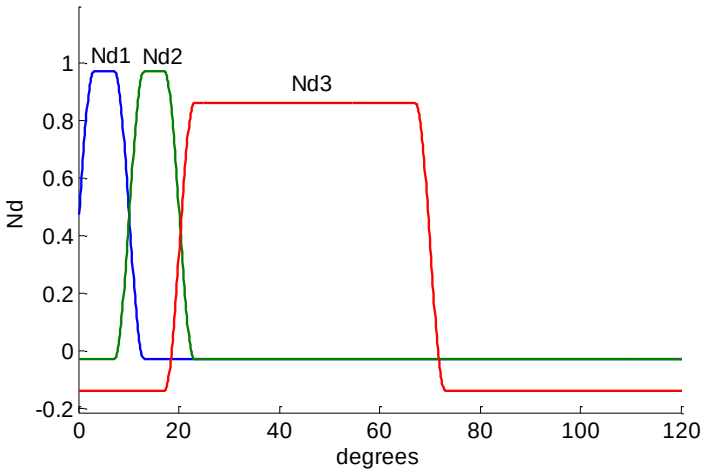

(a)

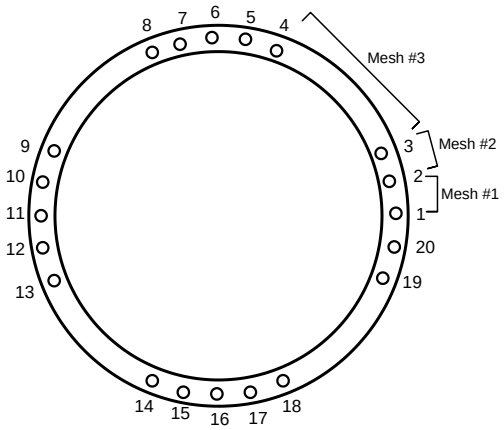

(b)

Figure 2.11 Damper winding. a) damper winding function for mesh #1,2 and 3, b) damper cage showing the bar numbers.

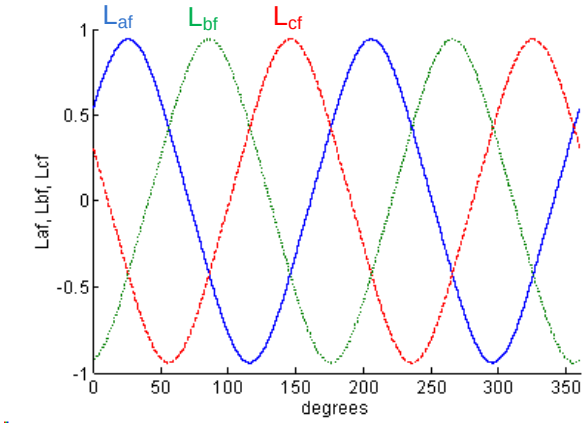

Figure 2.12 Mutual inductances between the field winding and three armature windings.

The mutual inductance between three armature windings and the first mesh in the damper winding are presented in Fig. 2.13. For the other small meshes, there are similar but phase shifted inductances. However, the mutual inductances of big meshes will be different.

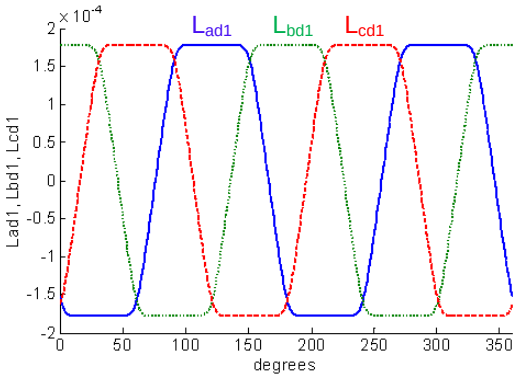

Figure 2.13 Mutual inductances between the damper mesh #1 (d1) and the three armature windings a, b, and c.

The mutual inductances of phase *A* of the armature winding with the first three meshes of the damper winding are presented in Fig. 2.14. It can be observed that the third mesh with a wider pitch than mesh #1 and #2, makes a wider function (see Fig. 2.11a) and therefore, a higher mutual inductance with the armature winding according to (2.41).

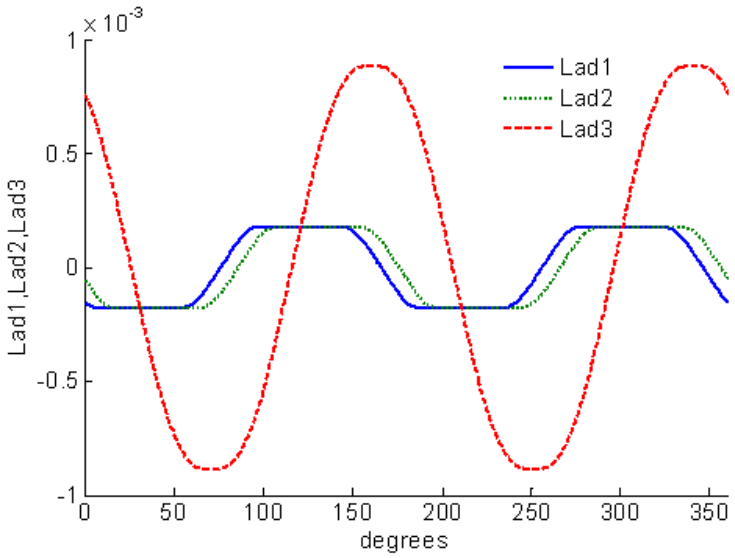

Figure 2.14 Mutual inductances between the stator winding phase 'a' and three damper meshes #1, 2 and 3.

2.11 Simulation Waveforms at No Load and No Field Excitation

The Matlab implementation is capable of simulating the machine behavior during transient as well as steady state conditions. In this subsection, the simulation results of some of the machine waveforms are presented at no load and without the field excitation.

Fig. 2.15 shows the transient armature current i_a, and the steady state three-phase armature currents i_a, i_b, i_c. It can be observed that the armature current has a higher value at startup. When the machine reaches synchronous speed, the armature currents make a balanced three phase set with constant amplitudes as shown in Fig. 2.15b.

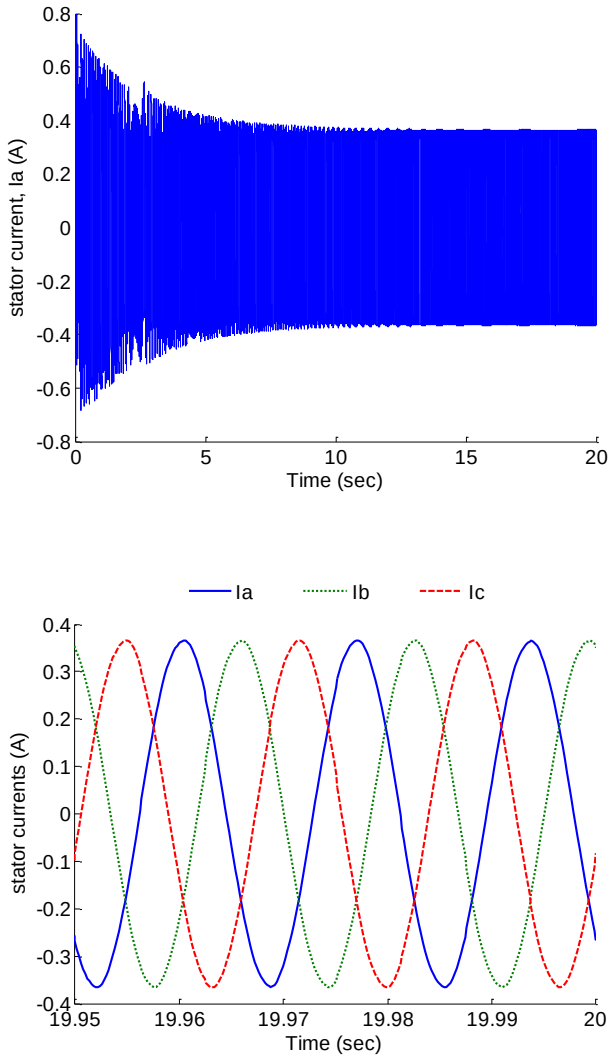

Figure 2.15 Armature currents: top) transient waveform i_a, bottom) steady state waveforms i_a, i_b, i_c.

The waveforms of electromagnetic torque and rotor speed are shown in Fig. 2.16 under no-load condition. The starting torque is high due to the high starting current and at steady state the average torque is zero. The rotor speed reaches the synchronous speed of 188.5 rad/sec at steady state.

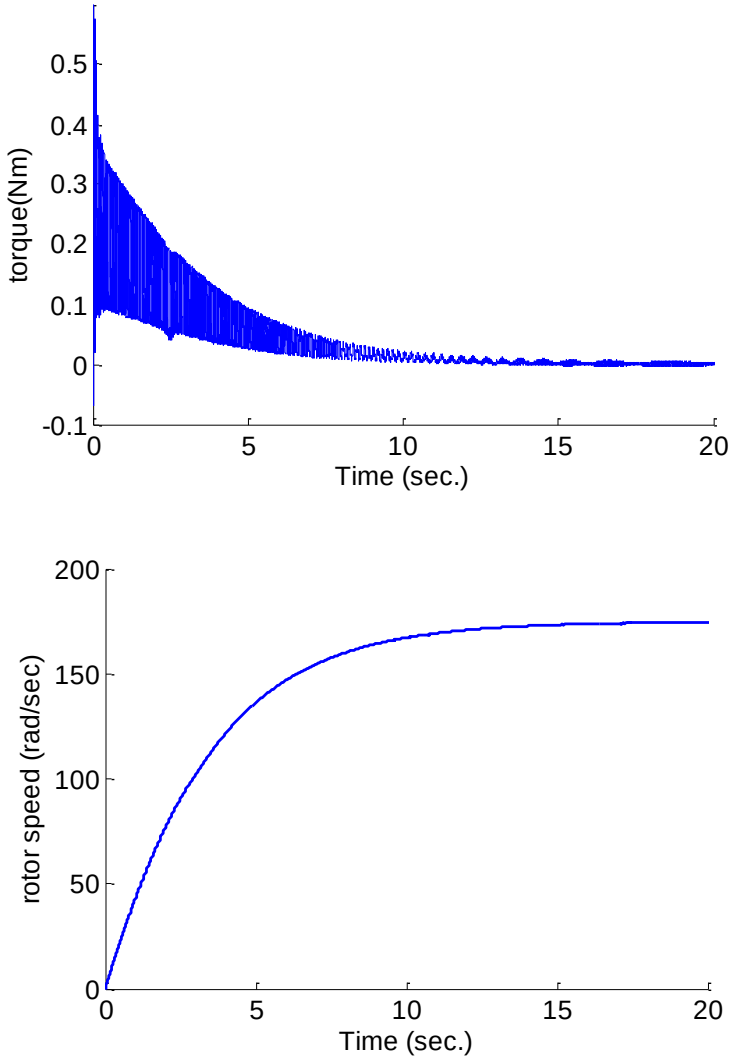

Figure 2.16 Transient waveforms: top) torque, bottom) speed.

In Fig. 2.17 the end ring mesh current and the actual current flowing through a small segment of the end ring are presented. The end ring mesh current is the fictitious current assigned to the end ring mesh and is zero as long as the mesh is symmetric. However, the end ring segment current is the actual current flowing in the end ring.

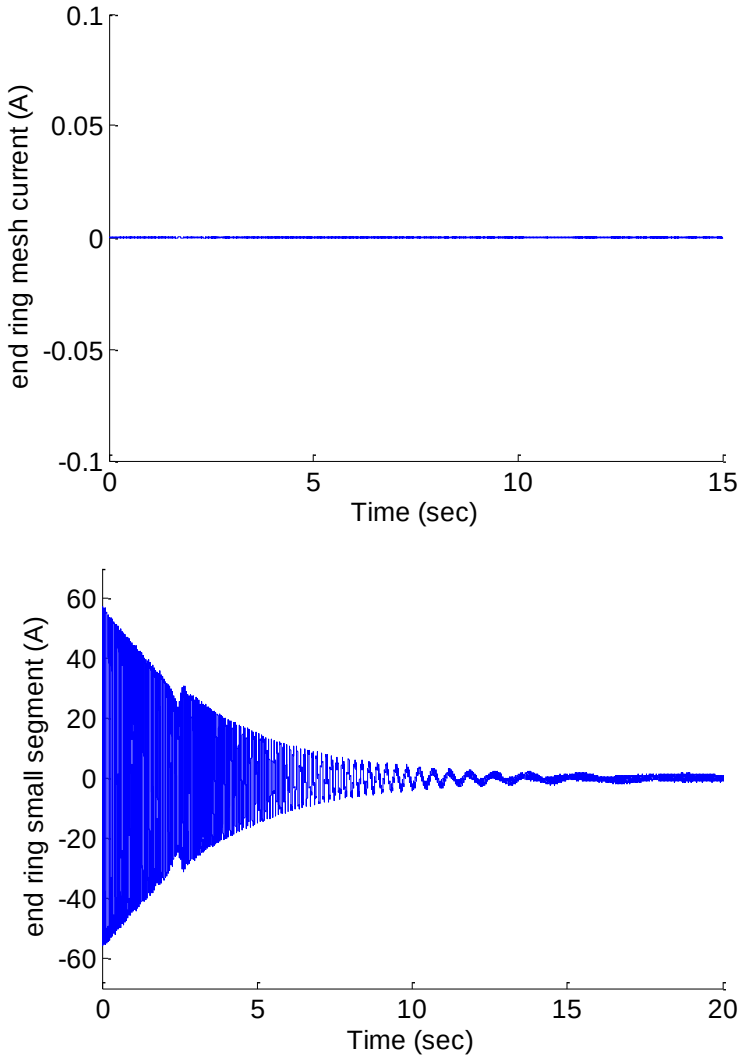

Figure 2.17 End ring currents. top) end ring mesh current, bottom) actual current in a small segment of the end ring.

With a healthy damper winding, the end ring mesh current is zero. However, the actual currents flowing through the end ring segments have high values at startup which decreases to a small current at steady state. It is worth mentioning that the actual current in any end ring segment is the difference between the end ring mesh current and the corresponding damper mesh current. The current flowing through the damper bar #1 which is the middle of the pole is shown in Fig. 2.18. Similar to the end ring segment current, the damper bar experiences high current at startup. This phenomenon which exists at any transient situation like start, stop and load change is the major cause of the damper winding failure. Since the currents flowing in the small and big meshes are not equal, the bars experience unequal heat and unequal expansion. When there are frequent load changes or start-stop cycles, the chance of damper failure increases.

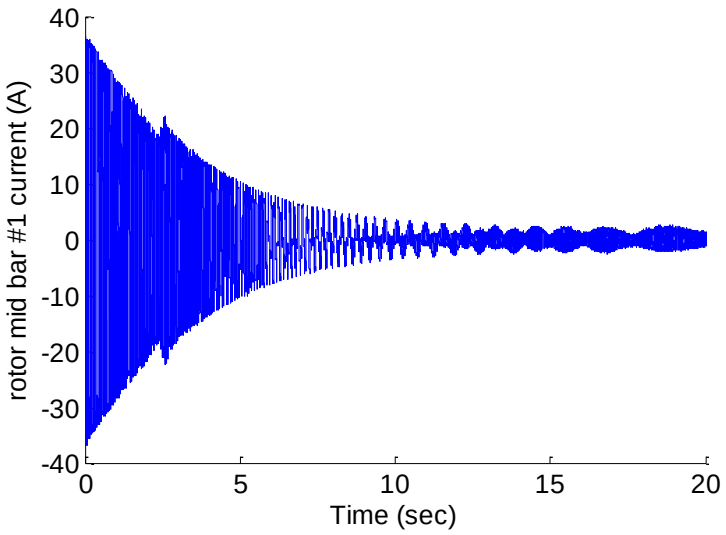

Figure 2.18 Damper bar #1 current.

2.12 Simulation Waveforms with Load and Field Excitation

Synchronous motors are not self-starting motors. This property is due to the inertia of the rotor. If the field winding is switched on at the same time that the armature winding is excited, the armature winding creates a rotating magnetic field instantaneously, which revolves at the designated motor speed. The rotor, due to inertia, will not follow the revolving magnetic field. In practice, the rotor should be rotated by some other means near to the motor's synchronous speed to overcome the inertia. Once the rotor nears the synchronous speed, the field winding is excited, and the motor pulls into synchronization. Damper winding is a means to start the motor as an induction motor to reach near the synchronous speed. The other techniques are using a separate motor to drive the rotor before it locks into synchronization, or reducing the input electrical frequency to get the motor starting slowly [46].

In this subsection, the simulation waveforms will be presented to illustrate the condition when initially the field is open through a large series connected resistance with the field winding. When the machine nears the synchronous speed the external resistance is shorted out and the field current is applied. To show the effect of each transition on the waveforms, 10% load is connected after the field was applied. Fig. 2.19 shows the transient waveforms of stator current, torque and rotor speed. First, the field winding is open under no-load condition. Then, when the rotor speed reached about 90% of the synchronous speed the field current of 1A was applied. After 10 seconds when the motor is locked to synchronization, the load was connected.

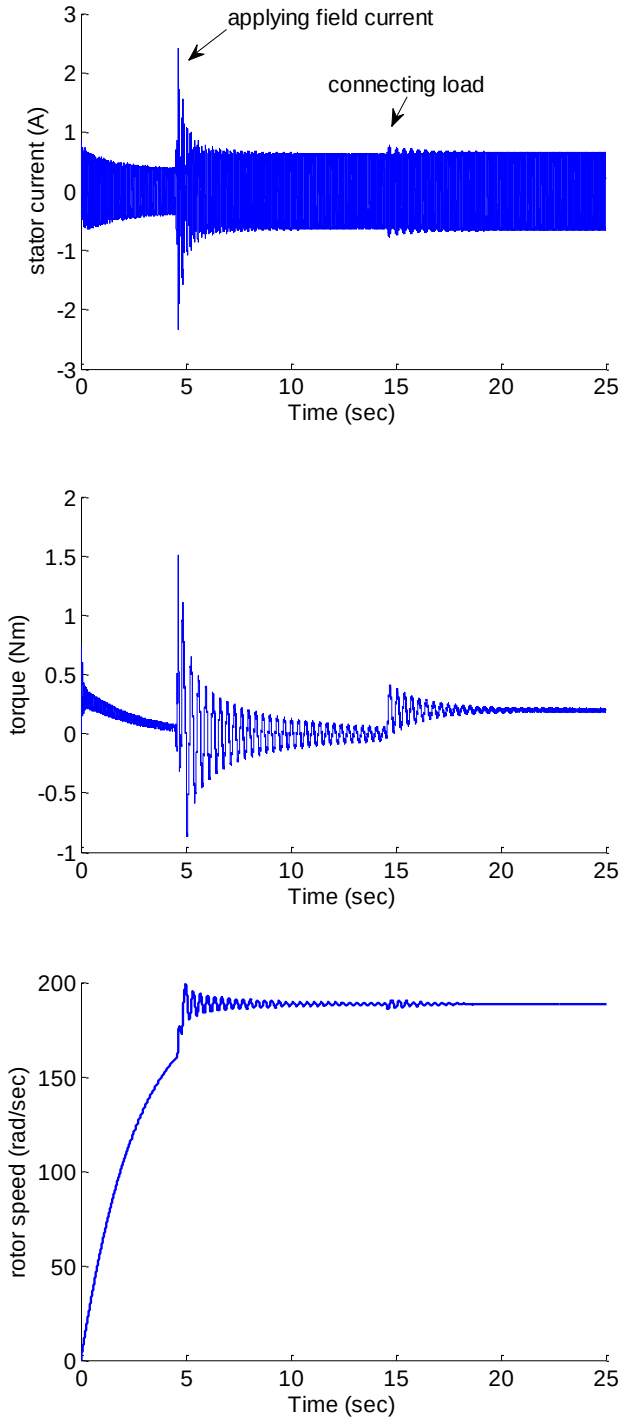

Figure 2.19 Waveforms during 3 transient phases. Top figure to bottom: armature current, torque, speed, field current, and damper bar current.

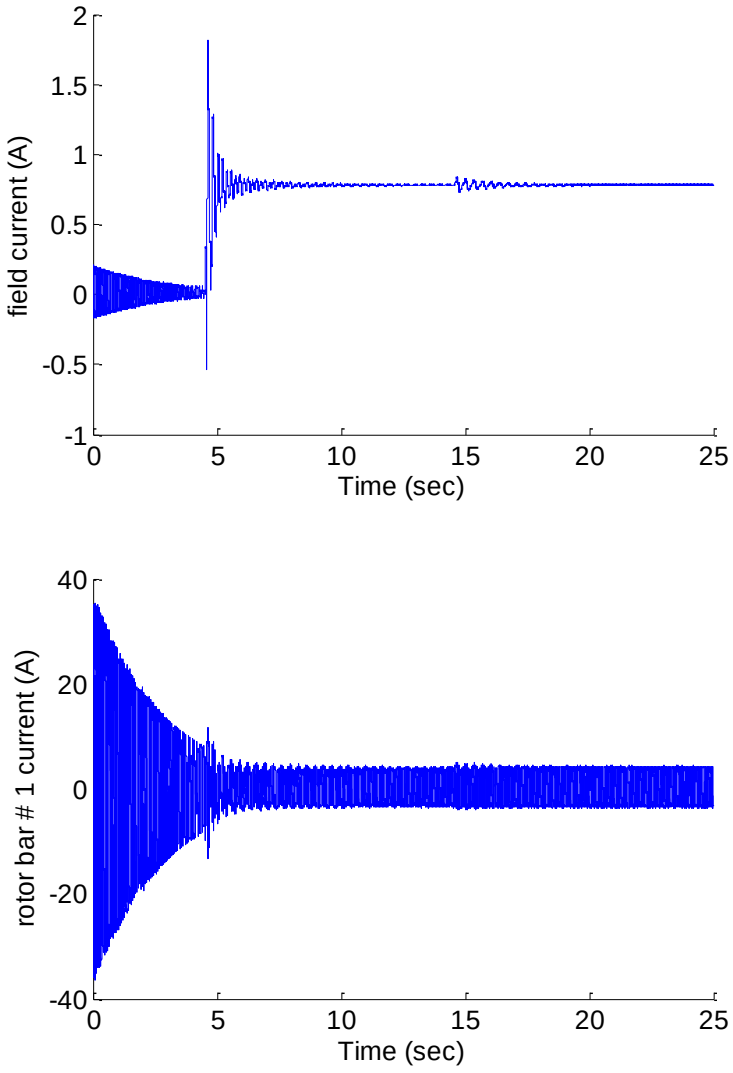

Figure 2.19 continued.

For a smoother transition when applying field current, it is more practical to use a variable external resistance in series with the field winding. This method will prevent an abrupt change in the field winding resistance and the field current. This approach is not used in the Matlab simulation.

2.13 Conclusions

In this section a new approach for modeling synchronous machines with a damper winding was presented. The magnetizing and mutual inductances of three sets of windings, armature, field and damper windings, were calculated using the winding function approach. A method for modeling a skewed rotor was presented. The electromagnetic torque equation and the voltage equations of all windings were derived in the natural reference frame. A system of differential equations was set up to be solved by Matlab. The simulation waveforms of a healthy machine were presented from studies during startup, when the field winding was excited, and when the load was connected. The next section will discuss the effects of damper faults on the machine waveforms.

3. EFFECTS OF DAMPER WINDING FAILURE ON THE MOTOR SIGNALS

3.1 Introduction

The function of the damper winding is to bring the rotor speed up to the synchronous speed at startup. It also helps damping out the oscillatory motion superimposed on the normal synchronous rotation of the shaft when the load is suddenly changed. If the motor is running at the synchronous speed, there will be no current induced in the damper winding and it has no effects on the motor operation. Therefore, a defected damper winding is not expected to affect the machine waveforms during the steady state synchronous operation. For diagnosis purpose, we can examine the waveforms during the following motor operations:

- Start or stop transient
- Field excitation transient
- Load change transient
- Asynchronous steady state operation with open field winding (like an induction machine)

In this subsection the armature current spectrum is studied at transient and steady state asynchronous operation under different broken damper bar conditions. The model developed in section 2 will be employed to introduce various damper fault situations. To introduce a bar breakage, its resistance is changed to a high value. Assigning a very large value to the defected bar resistance causes the program run time to be long.

3.2 Transient Analysis Using Short Time Fourier Transform

The standard Fourier Transform (FT) does not clearly indicate how the frequency content of a signal changes over time. In many applications such as speech processing, we are interested in the frequency content of a signal locally in time. Information which is localized in time cannot be detected from the Fourier Transform. Short Time Fourier Transform (STFT) is a method of detecting the frequency content of a non-stationary signal over time. It can be achieved by first windowing the signal and then taking the Fourier Transform of each window. The length of the window is optional. A long window will provide higher frequency resolution. A short window will provide higher time resolution because less averaging across samples is needed for each STFT value. Therefore, there is a trade-off between the time and frequency resolution when using STFT. The mathematical definition of the STFT of signal x(t) using a window function g(t) is as follows:

$$STFT(f,s) = \int_{-\infty}^{\infty} x(t)g(t-s)e^{-j2\pi ft}\,dt \tag{3.1}$$

The window function g(t) is sliding along the signal x(t). For each instant of time the shifted window g(t-s) is multiplied by x(t) and the FT of the product is computed. The magnitude of the STFT is called the spectrogram.

In this subsection the transient stator current during startup, field excitation and load change is investigated using STFT. The transient stator current is calculated using the method developed in section 2. The calculated stator current signal is used for time-frequency analysis. For STFT the following parameters are used: sampling rate of 5000, Hanning window of size 100 ms and one spectral slice every 20 ms.

3.2.1 Startup Transient

Motor current signature analysis (MSCA) has been extensively used to detect rotor bar and end ring failures in induction machines. It is a non-intrusive fault diagnosis technique because the stator current can be easily accessed and measured. This method is very useful for online condition monitoring of electric machines.

It is well known from the rotating field theory that any asymmetry in the rotor generates a negative rotating field which produces (1-2s)f component in the stator current spectrum. This component is known as the left sideband component which is specifically due to a broken bar. The left sideband in the stator current spectrum produces 2sf torque component and consequently speed ripple whose amplitude is damped by the inertia of the rotor-load combined [51 - 53]. Due to speed variation, the angular rotor position is modulated, producing two emfs and consequently two components at (1±2s)f in the stator current spectrum. With respect to the rotor which rotates at (1-s)f, these components appear at –sf and 3sf. Due to the rotor asymmetry a negative rotating field of -3sf with respect to rotor is produced which causes a new stator current component at (1+4s)f . If further harmonicas are considered, the rotor bar failure actually gives rise to a sequence of such sidebands around the fundamental of the stator current given by:

$$f_{1b} = (1 \pm 2ks)f, \qquad k = 1,2,3, \ldots \tag{3.2}$$

where, s is the rotor slip and f is the excitation frequency.

The magnitude of the sideband components are affected by the rotor-load inertia. Other spectral components around the harmonics of the stator current can be observed. The analytical expression for these components is given by Deleroi in [54] as:

$$f_{2b} = \left[\left(\frac{\mathrm{k}}{\mathrm{p}} \right)(1-s) \pm s \right] f, \qquad \frac{k}{p} = 1, 5, 7, 11, 13, \ldots \tag{3.3}$$

where, p is the number of pole pairs and k is the harmonic index.

For broken damper bar signature analysis during startup transient the armature windings are excited by a balanced three-phase sinusoidal voltage. The field winding is open and the motor is loaded with 10% of the rated value. Under these conditions the motor is running as an induction motor and the interaction of the armature and damper windings produces torque. The only difference is that the damper winding structure is different from the cage of an induction motor because it is not a complete cage. Since the field winding is not excited the motor cannot reach the synchronous speed. At the beginning the machine has a slip of one and it decreases to a small value as the motor speeds up. The asynchronous steady state slip depends on the load and the number of broken bars. Since the synchronous motor is running as an induction motor, the sideband frequencies in 3.2 and 3.3 are expected to be present in the current spectrum. The first four pairs of the sideband components of f_{1b} and f_{2b} are plotted in Fig. 3.1 as the motor slip decreases from 1 to 0.01. During transient as the motor slip decreases from one to a small value close to zero, the sideband components in 3.2 start from spectral components of: ±f, ±3f, ±5f, … and converge to some frequencies around f. Similarly, the sideband components in 3.3 start from ±f and end up at frequencies around f, 5f, 7f, 11f, 13f, … at steady state.

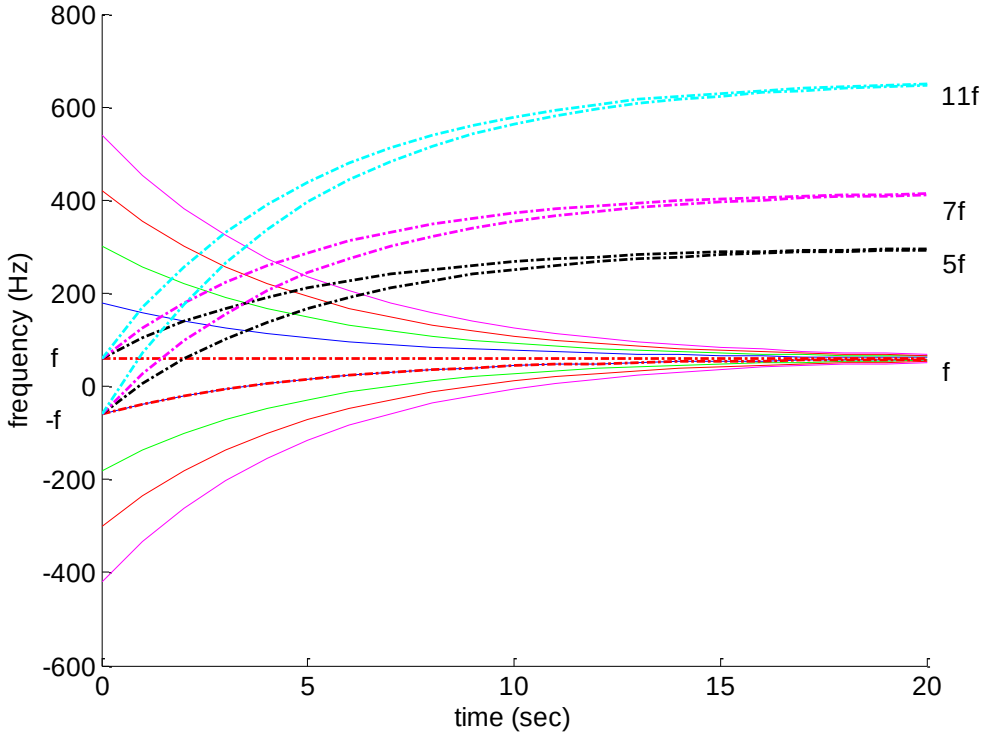

Figure 3.1 Variation of theoretical sideband components during startup transient.

In practice most of the theoretical sideband components of Fig. 3.1 are not visible in the current spectrum because their magnitudes are low and cannot be distinguished from noise. The left sideband component of the fundamental is the main signal to be monitored. It exists in both sets of f_{1b} and f_{2b} sidebands and has high magnitude. The next powerful signals are sidebands around 5th and 7th harmonics.

The simulation results of the armature current STFT during transient startup of the synchronous machine with 0 to 5 contiguous broken bars are presented in Fig. 3.2. These results are taken when the armature windings are connected to 120v line voltage, the field winding is open and the load inertia is 10% of the rated value.

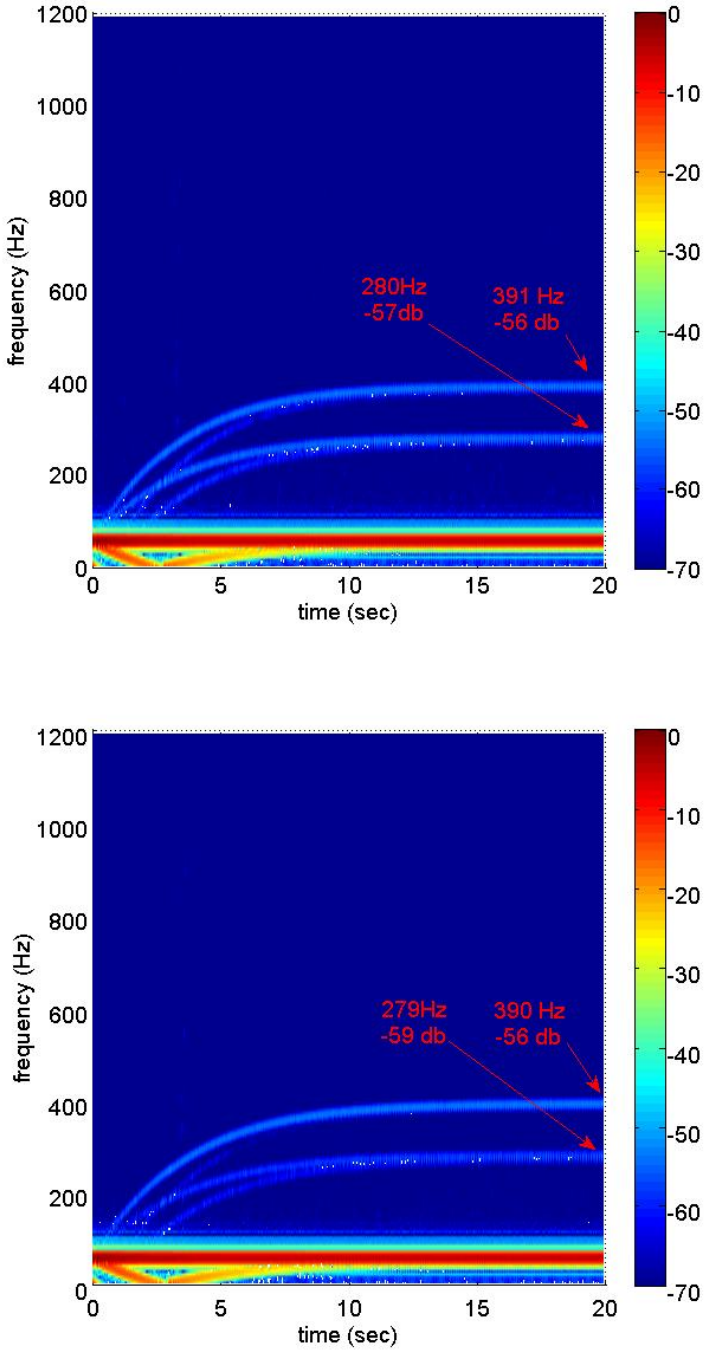

Figure 3.2 STFT of the line current during startup transient. Top figure to bottom: healthy, 1 broken bar to 5 broken bars.

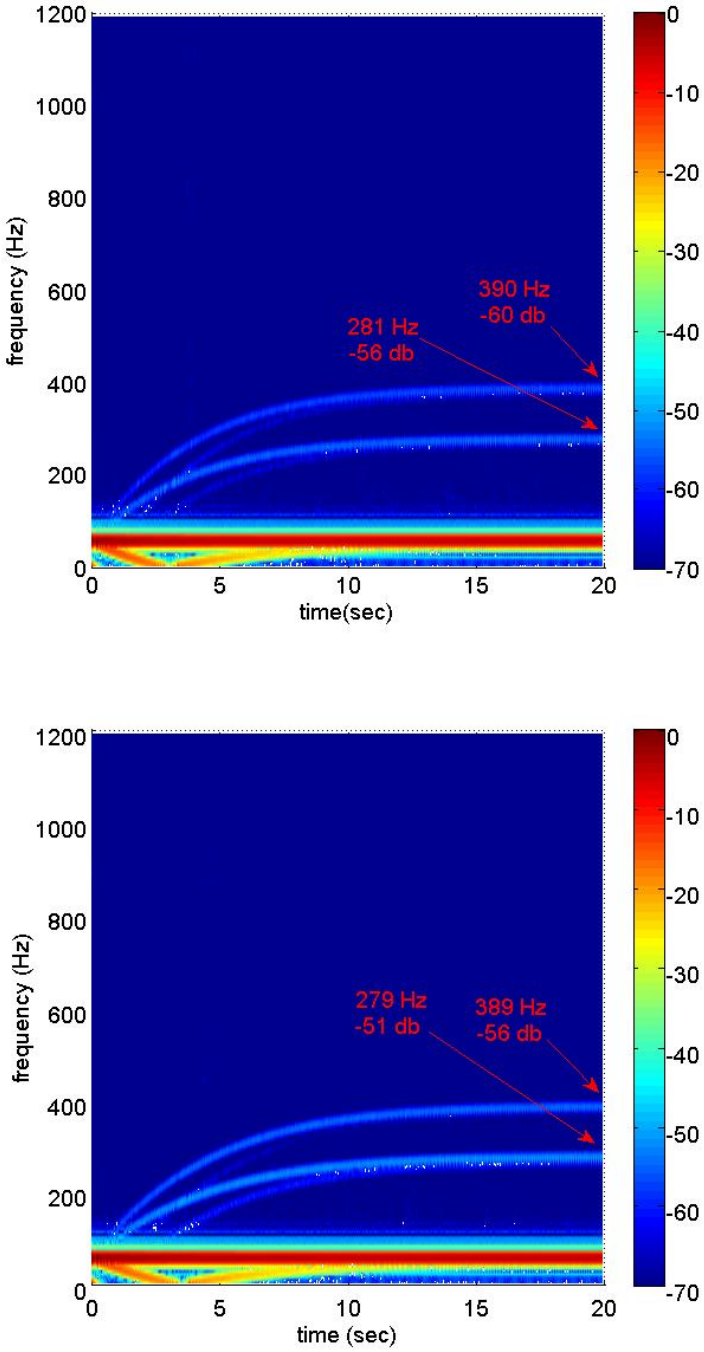

Figure 3.2 continued.

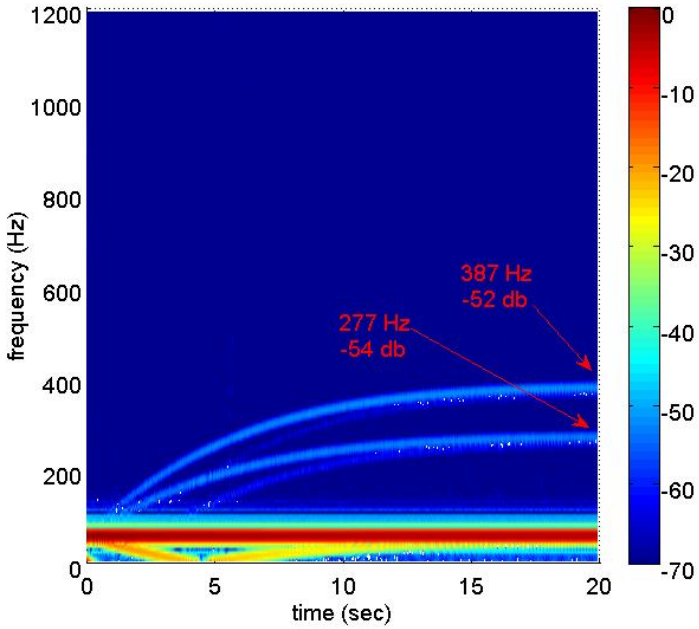

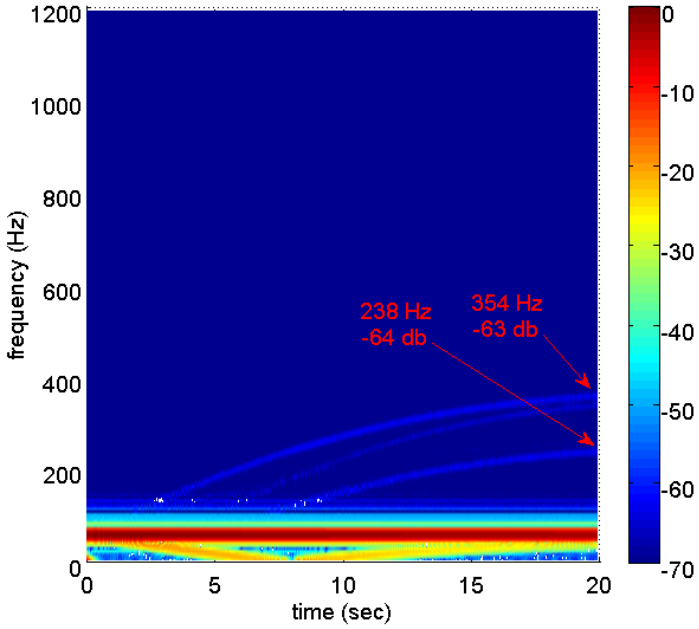

Figure 3.2 continued.

In Fig. 3.2 the color map indicates the magnitude of each spectral component during the first 20 seconds of startup transient in db. The most significant component in the spectrogram is at f which corresponds to the fundamental current. It can be observed that the left sideband of the fundamental components also have high magnitudes. It should be mentioned that the spectrograms in this figure show the one sided Fourier transform. That is why the main sideband which theoretically starts at –f and ends at f, has its negative part reflected to the positive frequency side. At steady state this speed dependent, high energy component fades away and coincides with the fundamental current which does not contain fault related information. This makes the separation of the fault related components difficult at steady state especially when the motor is not heavily loaded. Although the STFT is visually insightful it does not clearly indicate the degree of the damper failure.

The other significant components in the spectrograms are the components around 5^{th} and 7^{th} harmonics which start at +f and –f and end at (5-6s)f, (5-4s)f, (7-8s)f and (7-6s)f as given by 3.3. Another observation from the spectrograms is that the transient time increases as the number of broken damper bars increases. The magnitudes of the spectral components in different fault cases, are not clear indications of the fault severity and do not follow a certain pattern. With the very severe fault condition of 5 broken bars, when all damper bars in one pole are failed, the sideband components seem to have significantly lower magnitudes and the transient time is much longer.

It is very important to notice that even with a healthy damper winding the fault related sidebands appear in the current spectrum. The reason is that the structure the

damper winding is different from that of the cage of an induction motor. A damper winding can be considered as a cage with some missing bars in each pole. Therefore, the existence of the well known fault signatures of induction machines does not necessarily indicate a damper winding failure. Detection of the fault is possible if the variation of the sideband magnitudes can be predicted in each case of the fault. This subject will be investigated in section 5.

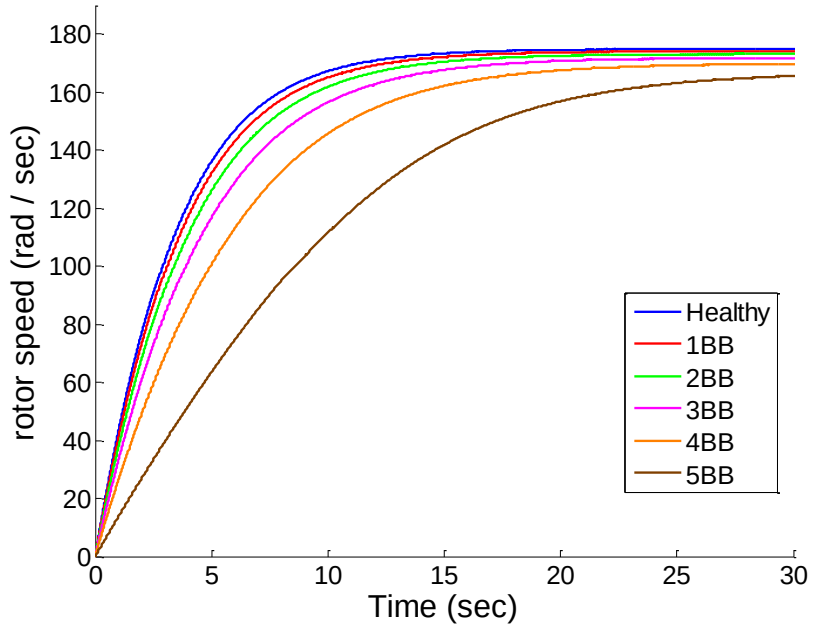

Figure 3.3 Transient rotor speeds for healthy and 1-5 broken damper bars (10% load).

The time domain rotor speed corresponding to the spectrograms in Fig. 3.2 for the healthy and 1-5 broken damper bars are shown in Fig. 3.3. Since the field winding is open, the interaction of the damper with the armature windings produces torque. The

induced current in the damper winding makes it an electromagnet which is attracted by the rotating field in the air gap and rotates with the field. As the number of defected bars increases the magnetization of the damper winding is reduced and the rotor cannot follow the rotating field closely. This leads to a lower steady state rotor speed or a higher slip.

Table 3.1 Simulation results for speed, slip, sideband components and transient time for different number of broken bars with 10% load at open field startup.

	Healthy	**1BB**	**2BB**	**3BB**	**4BB**	**5BB**
Steady state speed (rad/s)	174.9	174.1	173.2	171.9	170	167.1
Slip	0.072	0.076	0.081	0.088	0.098	0.114
F1 (Hz), k/p=5	282.7	281.7	280.5	278.9	276.4	272.8
F2 (Hz), k/p=5	274.0	272.5	270.8	268.3	264.7	259.1
F1 (Hz), k/p=7	394.0	392.5	390.8	388.3	384.7	379.1
F2 (Hz), k/p=7	385.4	383.3	381.0	377.7	372.9	365.5
Transient time (sec)	27	28	29	33	38	48

The steady state speed, rotor slip, the theoretical sideband frequencies around 5th and 7th harmonics, and the transient time are listed in Table 3.1. The sideband frequencies are calculated using (3.3) and the simulation slip value for each of the fault cases. The sideband frequencies around the 5th and 7th harmonics in the table are close to those in the spectrograms of Fig. 3.2 at steady state. In the severe fault cases the spectrogram components do not reach the steady state. The variation of transient time and slip for different fault conditions are shown in Fig. 3.4.

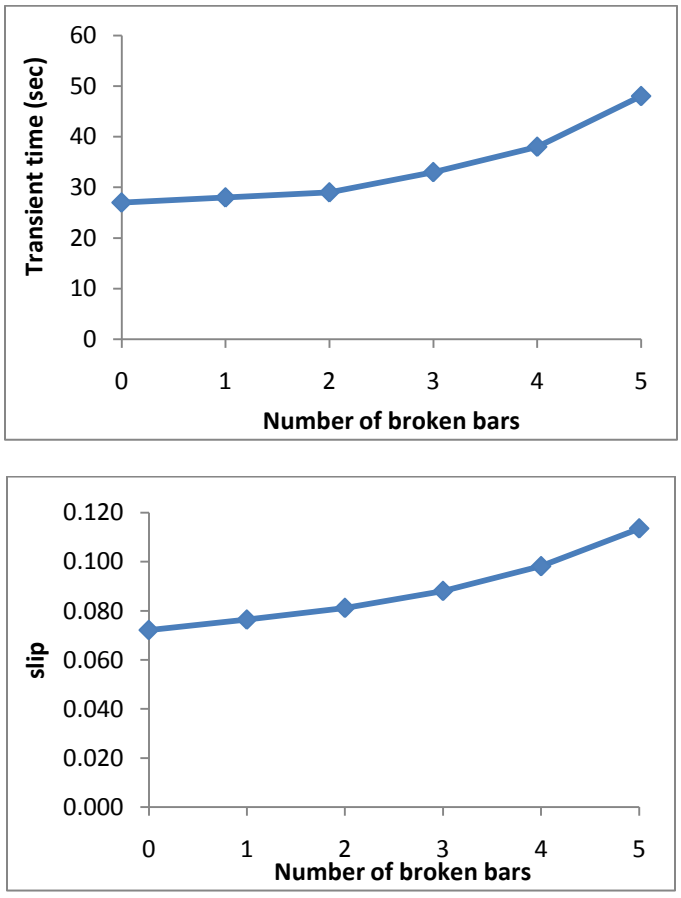

Figure 3.4 Effects of the fault severity. (top) transient time, (bottom) slip, for healthy and 1-5 broken bars with 10% load.

3.2.2 Field Excitation Transient

When the machine starts as an induction motor and speeds up near the synchronous speed then the field winding is connected to 15v dc. The field winding becomes a strong magnet and pulls into synchronization. During a short transient time between the field excitation and when the rotor reaches synchronous speed, the damper winding comes into effect. As shown in Fig. 3.5, when the field voltage is connected, the rotor speed oscillates before reaching the synchronous speed. This causes some oscillations in the armature current as well.

The STFT of the armature current for healthy and 1-5 broken damper bars, after applying the field voltage, are presented in Fig. 3.6. In this figure the spectrograms show that at steady state, when the rotor reaches synchronous speed there is no current induced in the damper winding. Therefore, the sideband components which are generated by the defected damper bars in the induction mode of operation do not appear around the fundamental and harmonics in the spectrogram. The transient time and the harmonic magnitudes do not change significantly in different fault cases and no specific pattern is observed in their variations. In the severe fault case of 5 broken bars, only the 5th harmonic exits in the spectrogram which has a very low magnitude.

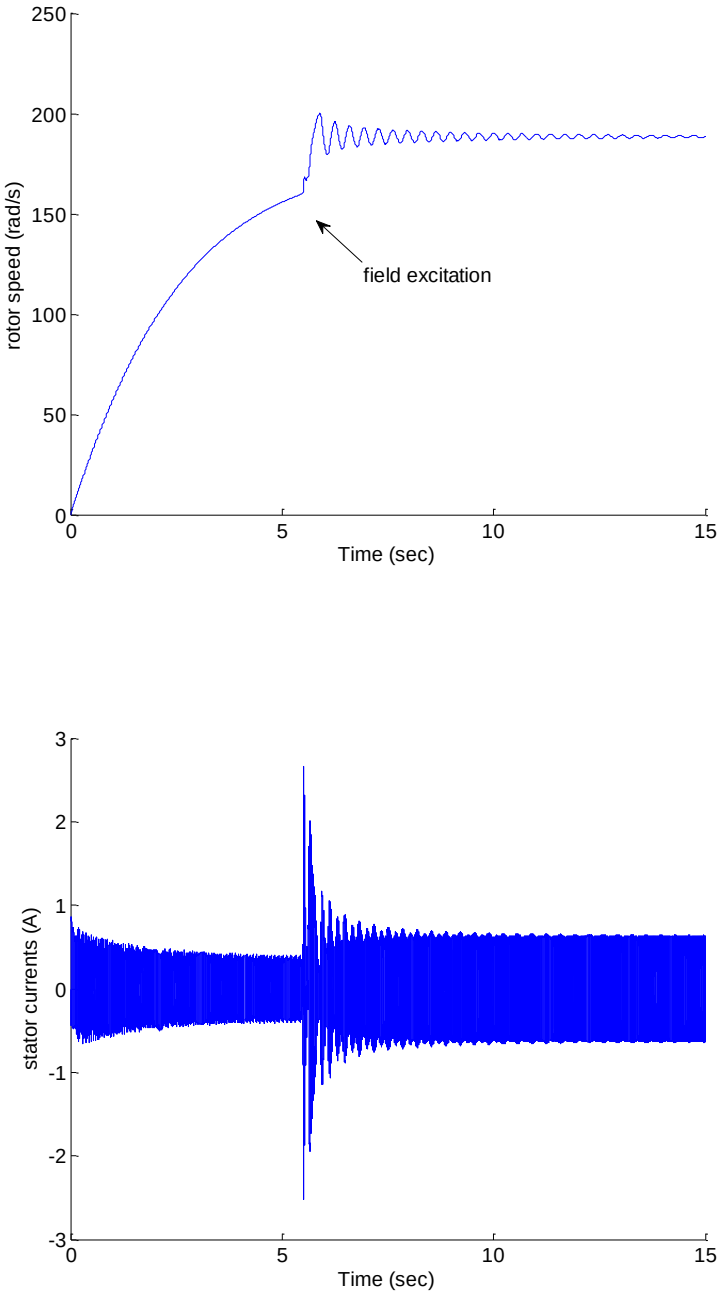

Figure 3.5 Field excitation transient. (top) speed, (bottom) armature current.

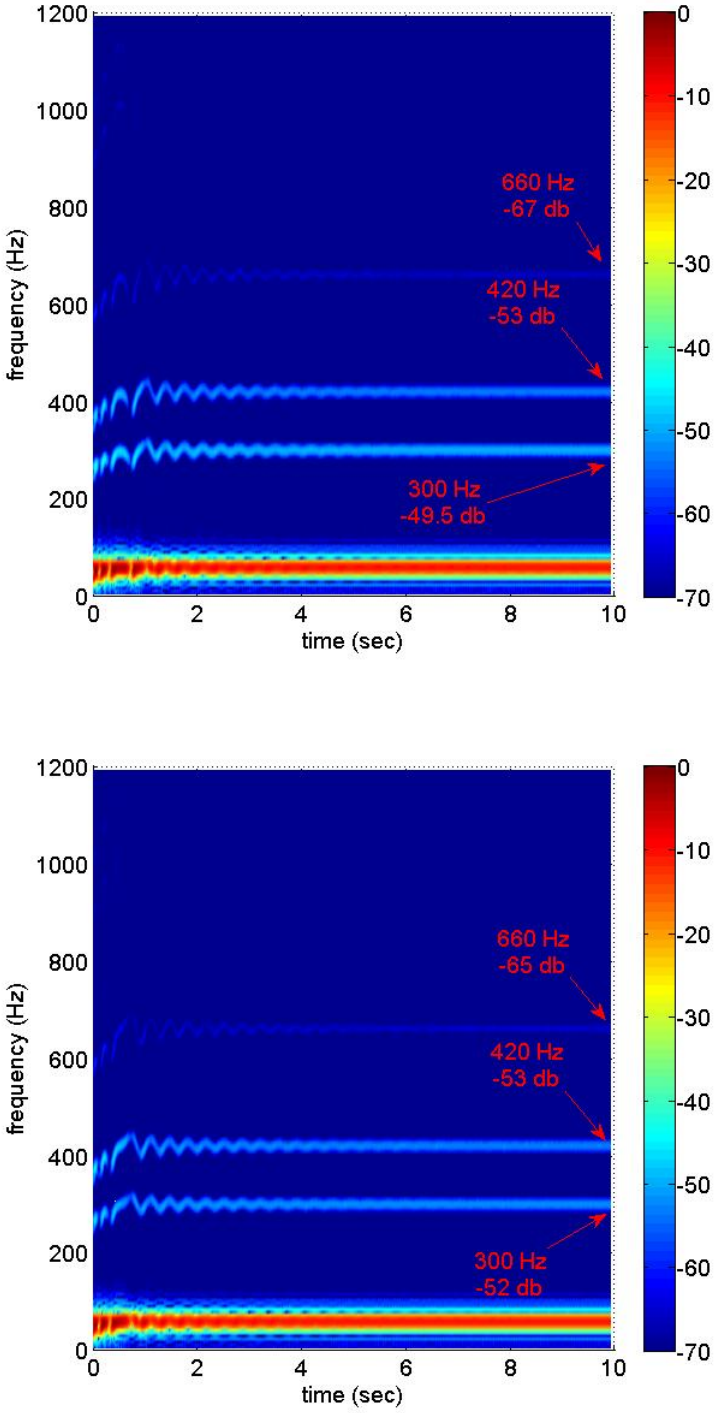

Figure 3.6 STFT of the line current during Field excitation transient. Top figure to bottom: healthy, 1 broken bar to 5 broken bars.

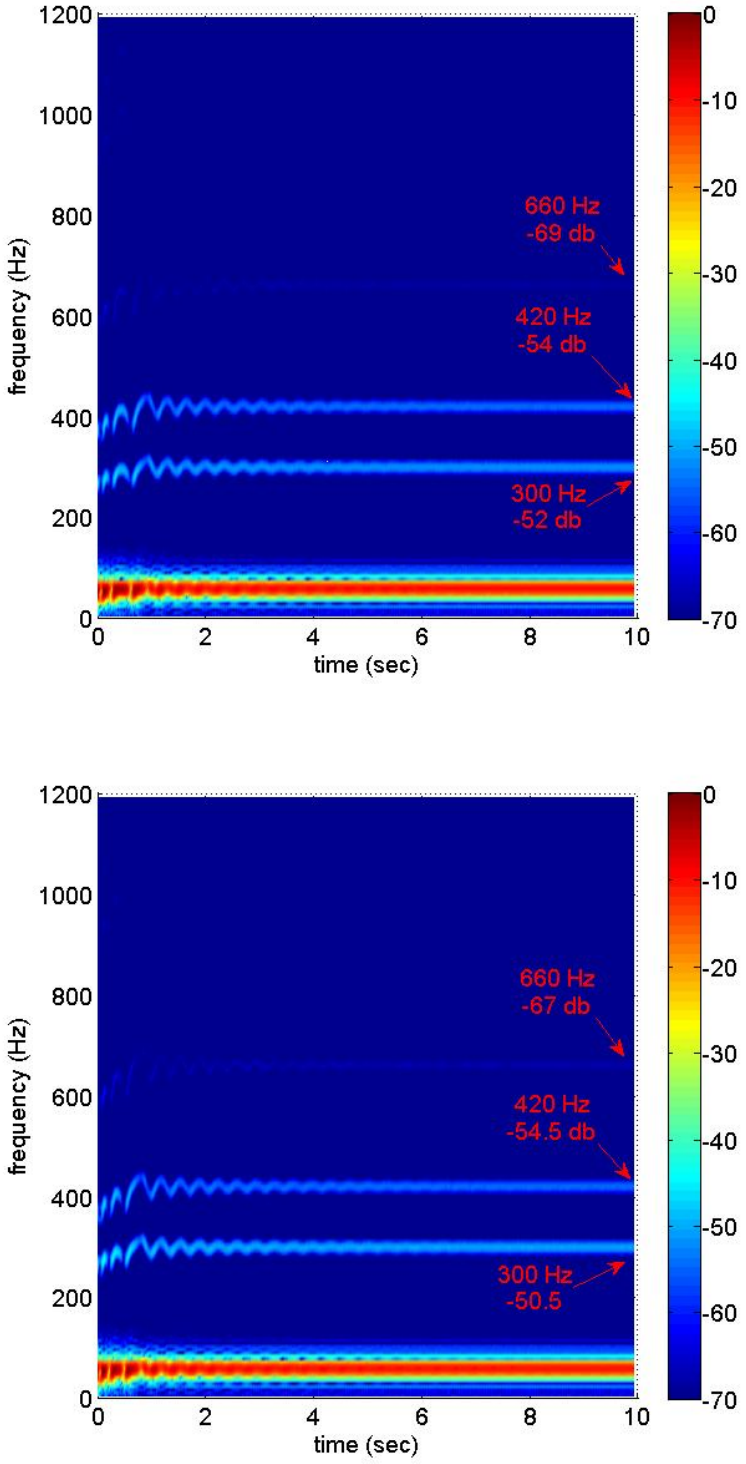

Figure 3.6 continued.

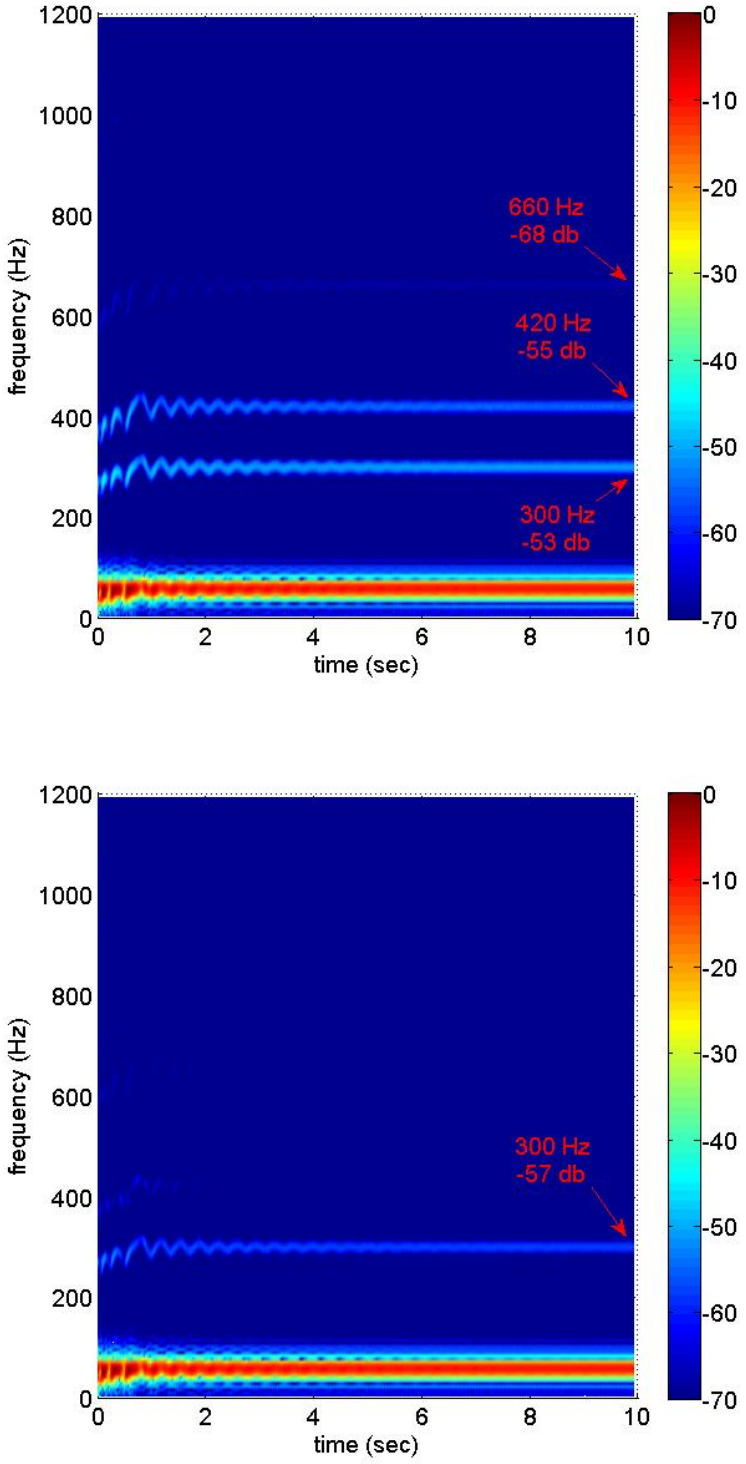

Figure 3.6 continued.

3.2.3 Load Change Transient

When the field winding is excited, the rotor speed reaches the synchronous speed. At this time there is no current induced in the damper winding and the damper winding becomes affectless. If the load is changed, the rotor speed momentarily goes out of synchronization and after some oscillations comes back into it. During the load change transient there will be some currents induced in the damper winding. The field generated by this current will in turn induce current in the armature windings. The STFT of the armature current during load change transient can be investigated for different damper fault cases to check if there is any useful information in the spectrogram for diagnosis purposes.

Figure 3.7 shows the simulation results of the time domain rotor speed and armature current after the load is changed from 10% to full load. The load is changed when the rotor is at the synchronous speed. The STFT of the armature current during load change transient is presented in Fig. 3.8 for healthy and 1-5 broken damper bar cases. It can be observed in the spectrograms that there are some oscillations in the harmonics due to the stator current oscillations after a sudden load change. No sidebands are observed around any of the frequency components to indicate the damper bar failure. This was true for the field excitation transient as well. The reason is that in both transient cases the field voltage is connected which pulls the rotor into synchronization. The magnetization of the damper winding during transient, however is speed dependent and is not as strong as the field winding magnetization. The conclusion is that when the field is connected it becomes the dominant magnetized winding on the

rotor and a faulted damper winding does not leave any clear signature on the current spectrum.

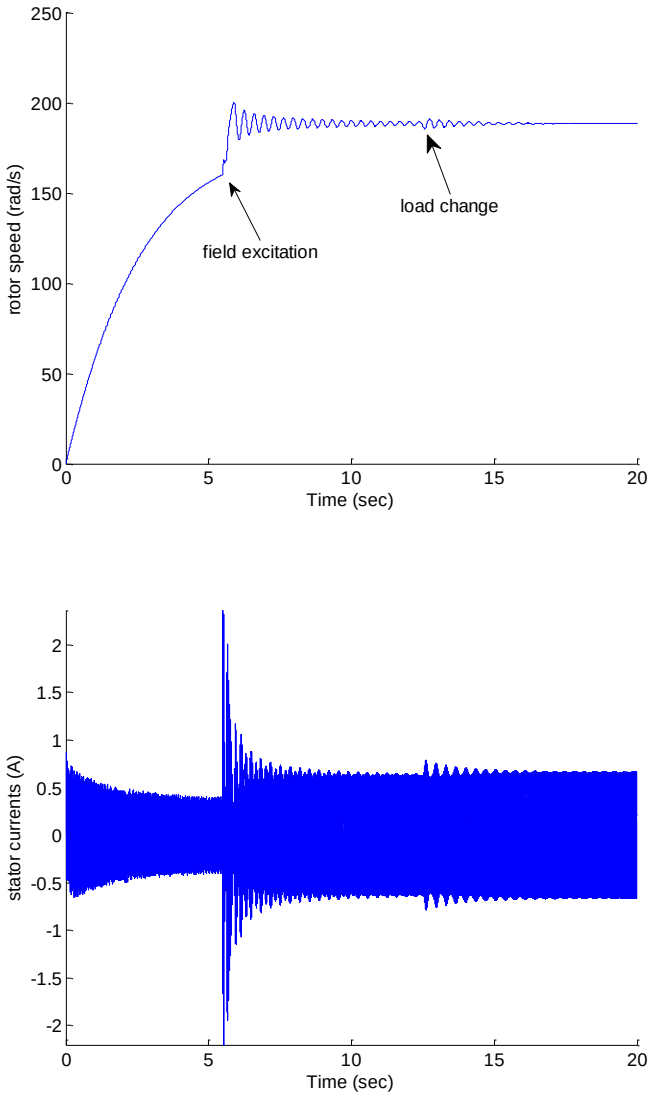

Figure 3.7 Load change transient after the field winding being excited. (top) time domain speed, (bottom) armature current.

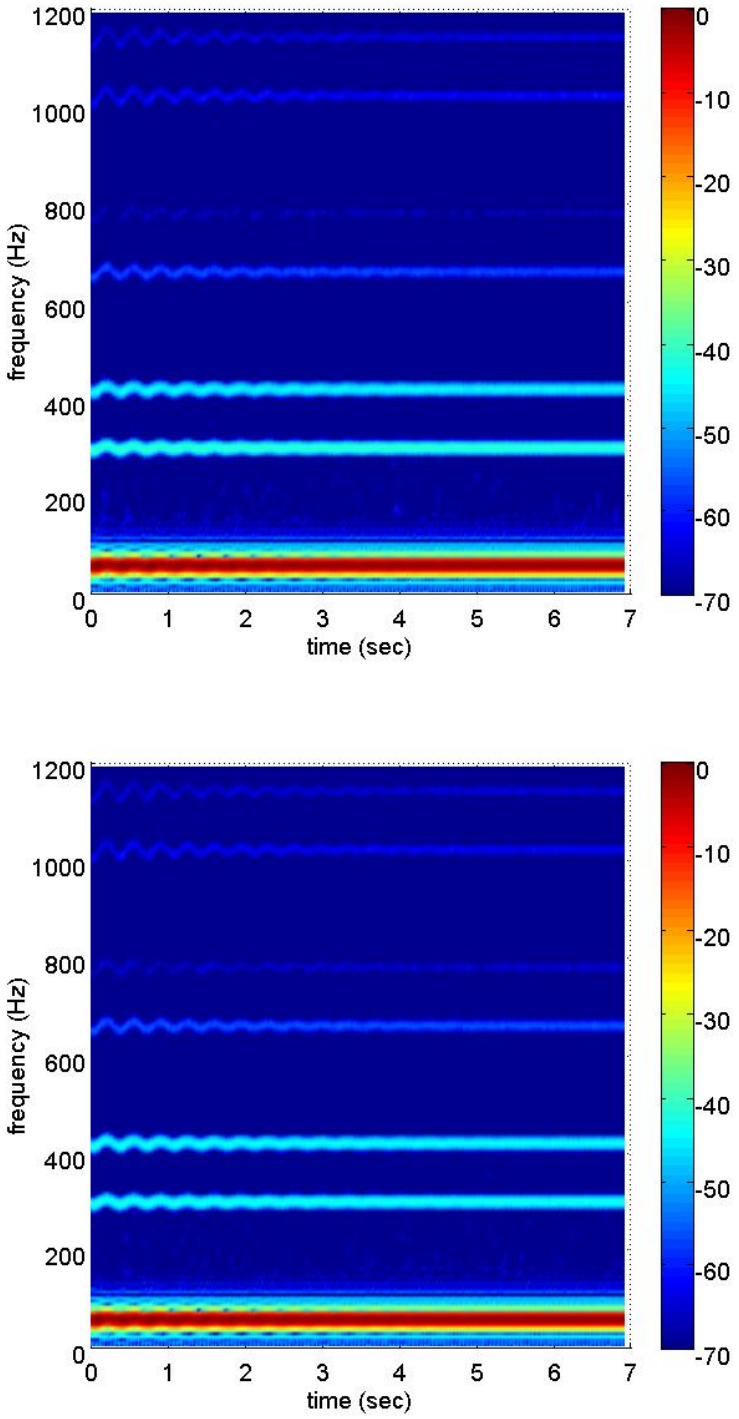

Figure 3.8 STFT of the line current during Load change transient. Top figure to bottom: healthy, 1 broken bar to 5 broken bars.

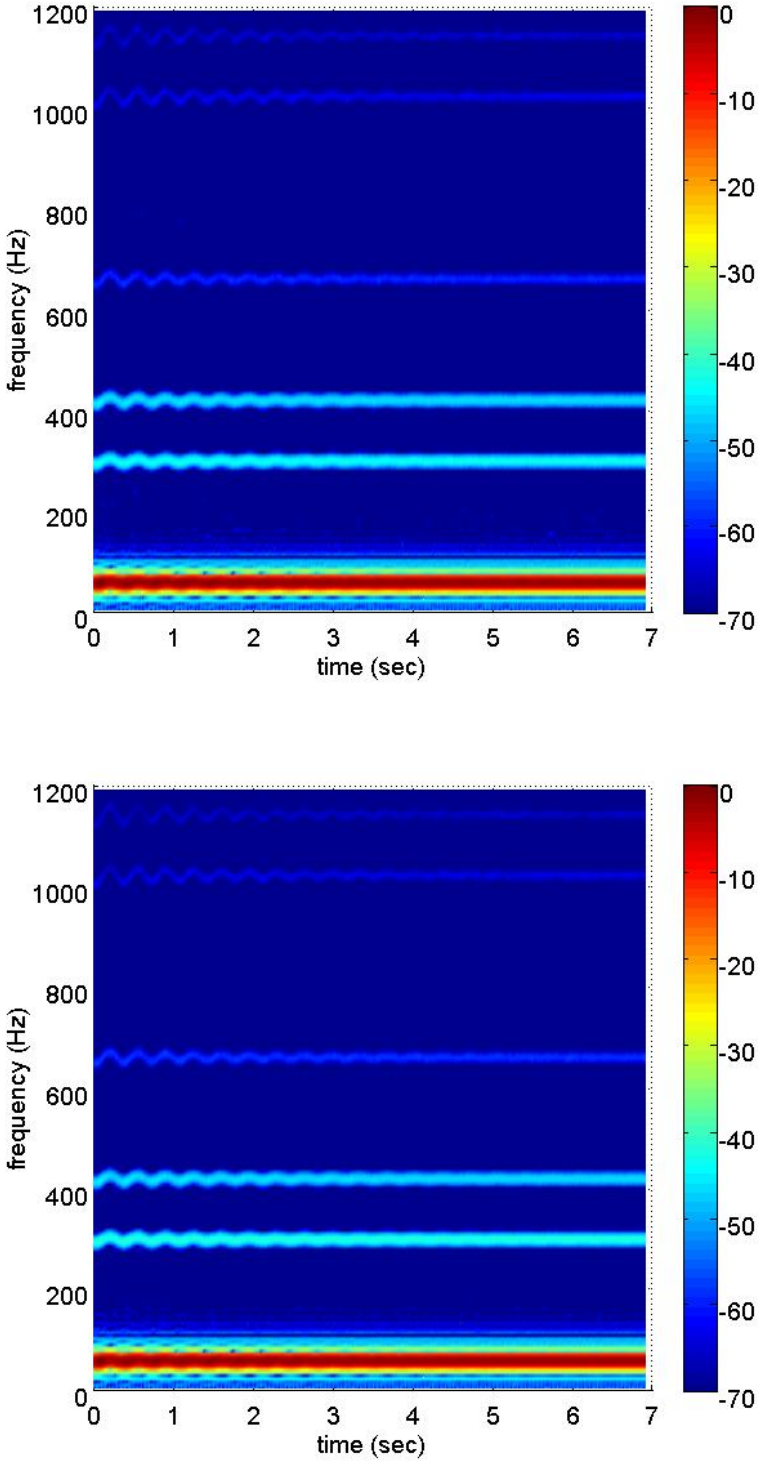

Figure 3.8 continued.

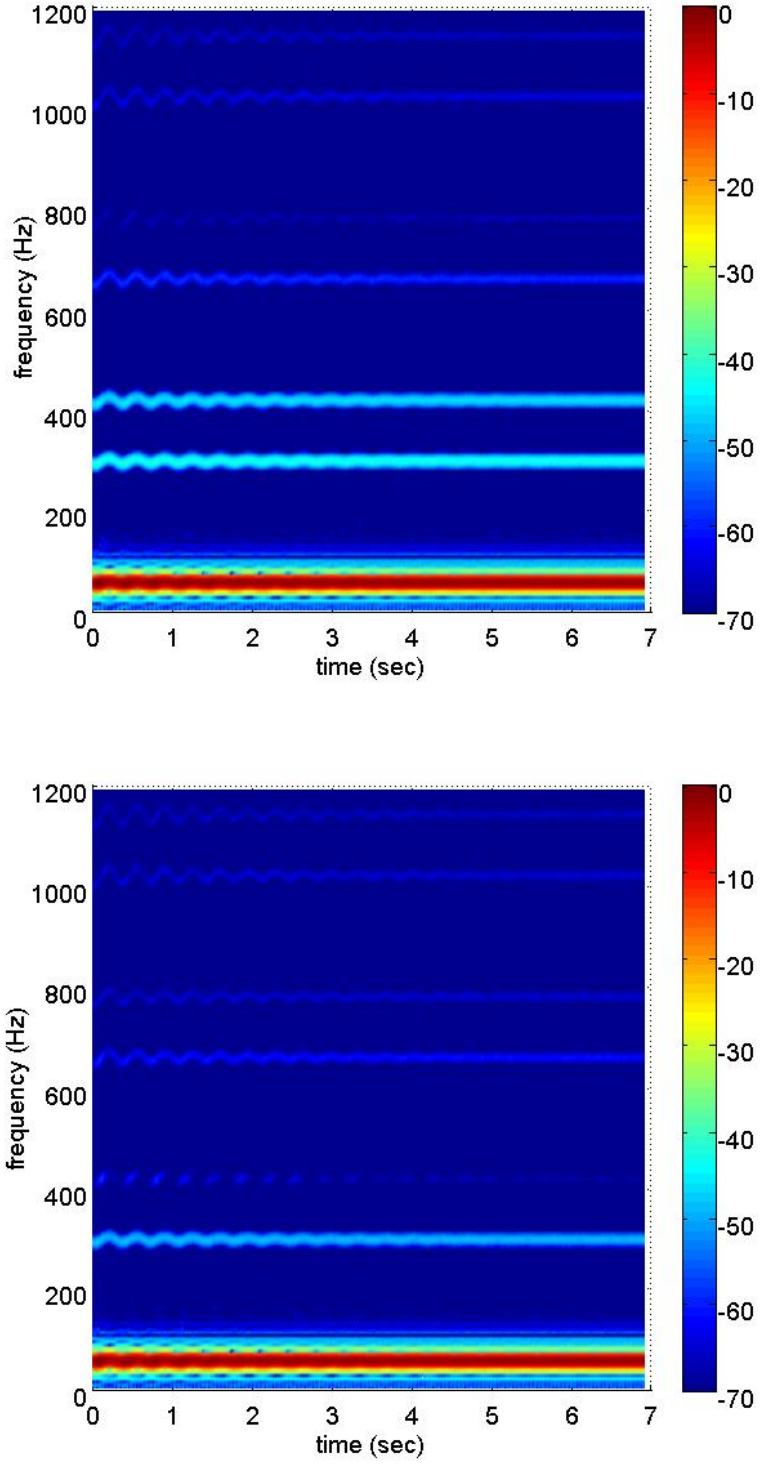

Figure 3.8 continued.

In the spectrograms of Fig. 3.8 higher order of harmonics exist compared to the spectrograms of the field excitation transient in Fig. 3.6. This is due to the heavier load conditions. Since the load is changed from 10% to full load, the fundamental and its spectral components have higher magnitudes which make them visible in the spectrograms of Fig. 3.8.

3.3 Asynchronous Steady State Analysis

In this subsection, the current spectrum is analyzed when the motor is running at asynchronous steady state. That is when the armature windings are connected to the power supply but the field winding is not excited. One of the techniques to start a synchronous motor is to start it as an induction motor and lock it into synchronization by connecting the field voltage, once it reaches near the synchronous speed. If the field is not energized it will run at a constant asynchronous speed exactly like an induction motor. The only difference is that the rotor of the induction motor is a complete cage with the bars equally distanced from each other while the damper winding of the synchronous motor has some gaps between the poles. These gaps make the damper winding look like a cage with some missing bars between the poles and functions as a symmetrically defected cage.

The existence of any asymmetry in the cage rotor of an induction machine will result in a backward rotating field component. In the case of rotor asymmetry, a backward rotating field at slip frequency -sf will appear in the air gap. This backward rotating field will induce an emf in the stationary stator winding at (1-2s)f. This is

known as the left sideband component (LSBC) of the stator current and is used as the broken bar signature in motor current signature analysis (MCSA). This component represents the cyclic variation of current and results in speed and torque pulsations at 2sf [3, 51, 55].

Since the LSBC contains the highest energy compared to the other fault related components, we will focus on this component for the fault diagnosis purpose. The synchronous motor was examined under different load conditions with healthy and 1-5 contiguous broken damper bars at asynchronous steady state operation. The calculated current spectra with 10% load are demonstrated in Fig. 3.9 at different fault conditions. The current spectra show that the left side band components are exactly located at (1-2s)f with their corresponding slips listed in Table 3.1. It can be observed that even with a healthy damper winding and a light load the left side band component still exists. As mentioned previously, this phenomenon is due to the non-uniform distances between the bars. An increasing pattern exists in the variation of the slip with the fault severity. The magnitude of the LSBC however, does not seem to follow a certain pattern.

Increasing the load will move the left side band further from the fundamental component in each of the fault cases because of the increasing slip. Fig. 3.10 presents the current spectra for healthy and 1-5 broken damper bars when the motor is loaded with 40% of its rated value. Table 3.2 contains the simulation slip values for the severe cases of 4 and 5 broken bars with their corresponding theoretical sideband components given by (3.3).

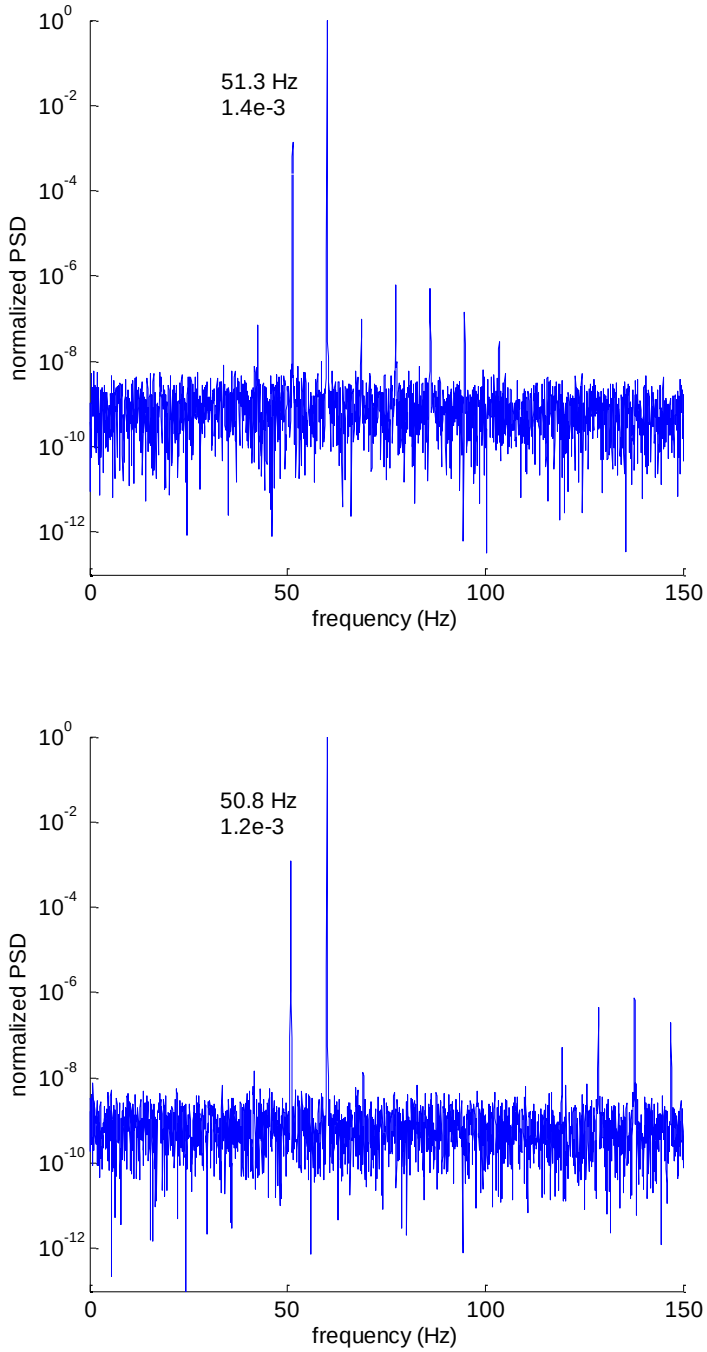

Figure 3.9 Current spectrum at asynchronous steady state speed with 10% load. Top figure to bottom: healthy, 1 broken bar to 5 broken bars.

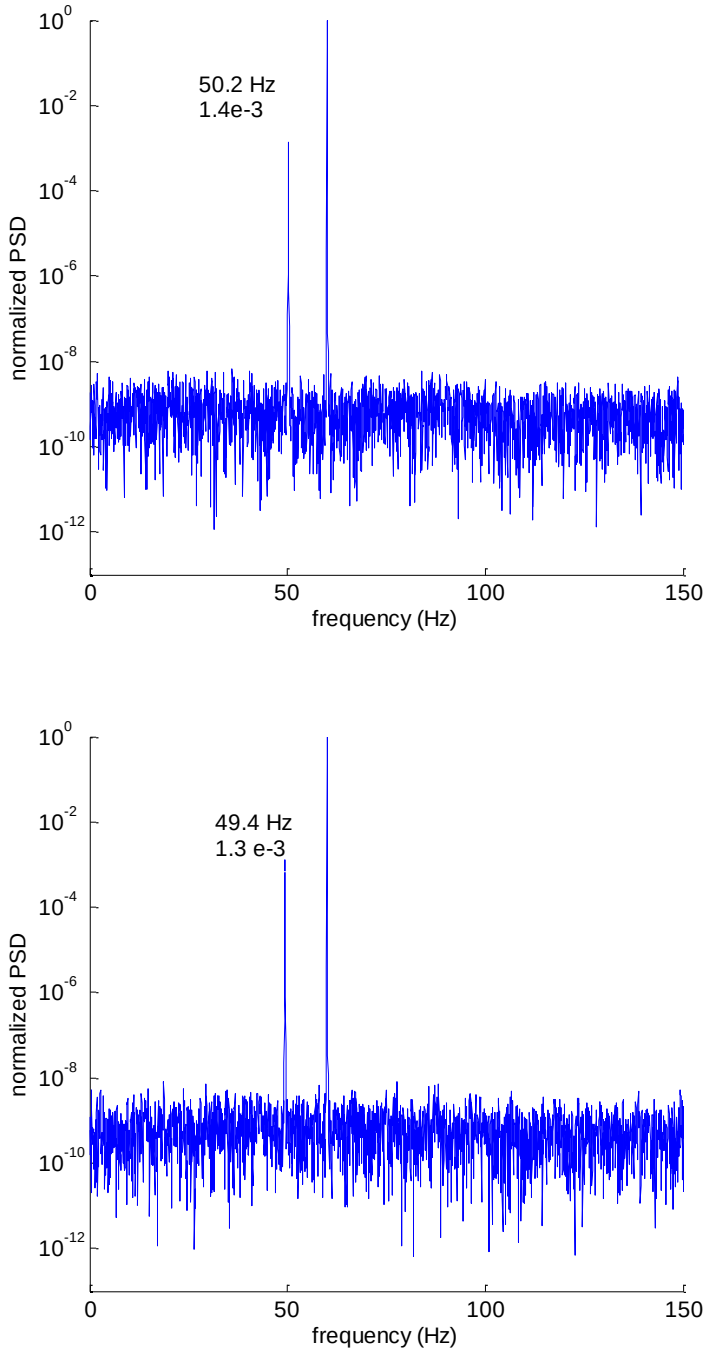

Figure 3.9 Continued.

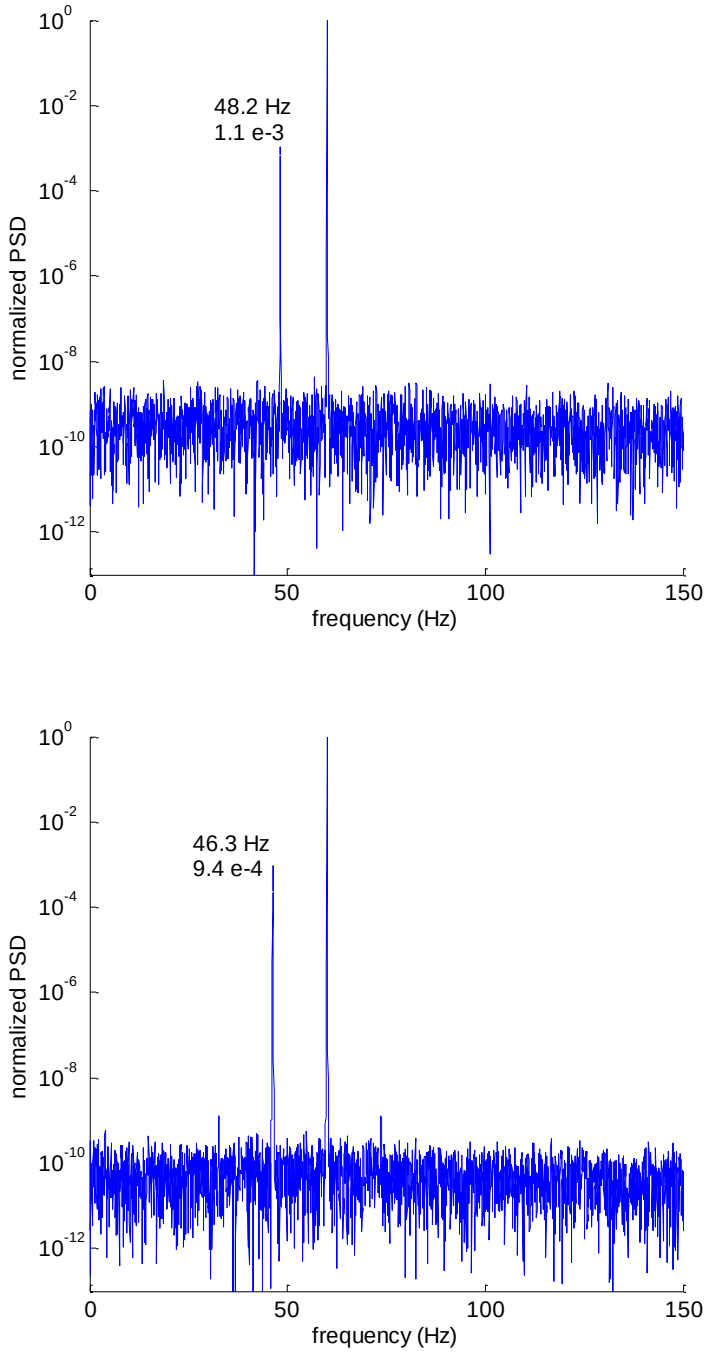

Figure 3.9 Continued.

In the current spectrum, for the severe case of 5 broken bars in Fig. 3.10, the motor slip is very high around 0.91. This is due to the heavily loaded motor in addition to the extreme asymmetric damper winding. Since the slip exceeds 0.5, the LSBC at (1-2s)f becomes negative which is reflected to the positive side in the spectrum at 49 Hz. This sideband component should not be interpreted as motor having a lower slip of 0.091 since both slip values of 0.91 and 0.09 generate the same sidebands in the spectrum. In the spectrum of the 5 broken bar case, there are some other components near the fundamental which are actually the sidebands around the 5^{th} and 7^{th} harmonics moved near the fundamental due to large motor slip. If the speed dependent components given by (3.3) are evaluated at s=0.91 for k/p=5 and k/p=7, the same frequency components appearing in the spectrum can be obtained. For the case of 4 broken bars the motor slip is 0.46 which locates the LSBC at a low frequency near zero. If the rotor slip is 0.5, the LSBC fades out because its magnitude is proportional to |1-2s| as will be shown in section 5.

Table 3.2 Slip and sideband components for 4 and 5 broken bars with 40% load.

	Slip	**LSBC(Hz) (1-2s)f**	**F1 (Hz) k/p=5 (5-4s)f**	**F2 (Hz) k/p=5 (5-6s)f**	**F1 (Hz) k/p=7 (7-6s)f**	**F1 (Hz) k/p=7 (7-8s)f**
4bb	0.46	4.8	189.6	134.4	254.4	199.2
5bb	0.91	-49.2	81.6	-27.6	92.4	-16.8

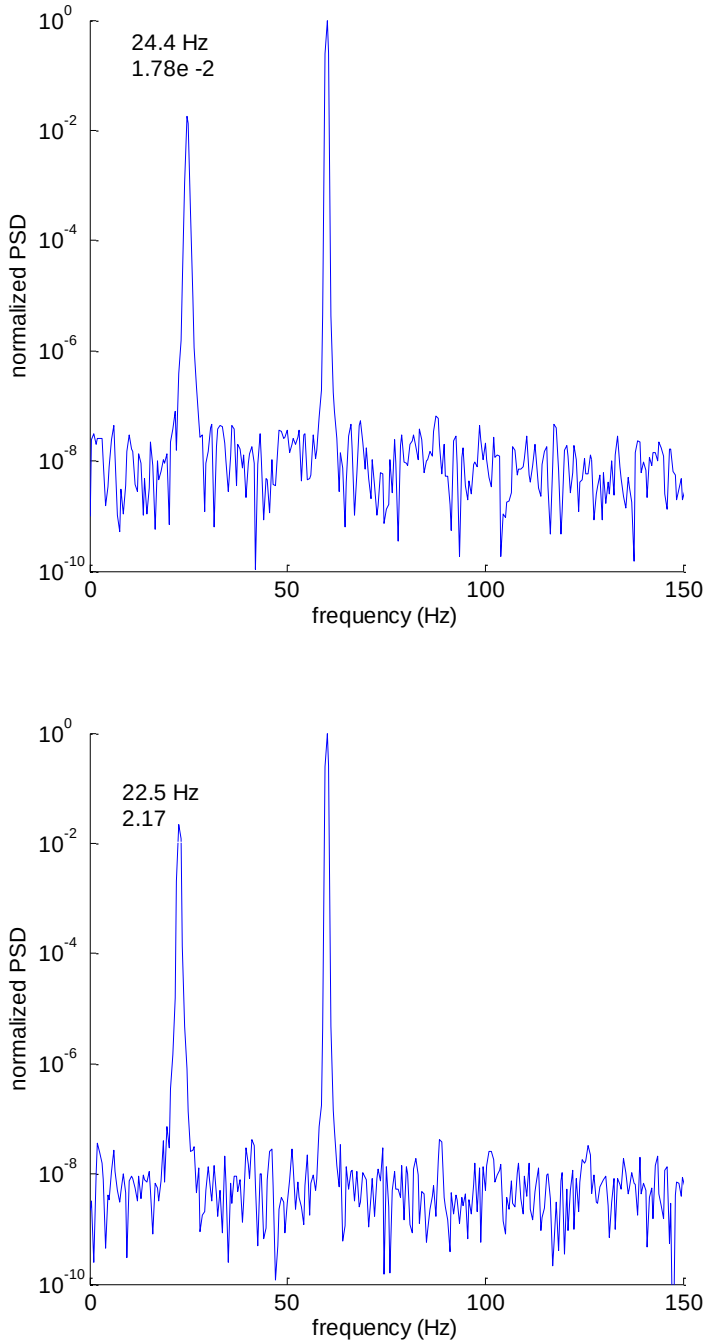

Figure 3.10 Current spectrum at asynchronous steady state speed with 40% load. Top figure to bottom: healthy, 1 broken bar to 5 broken bars.

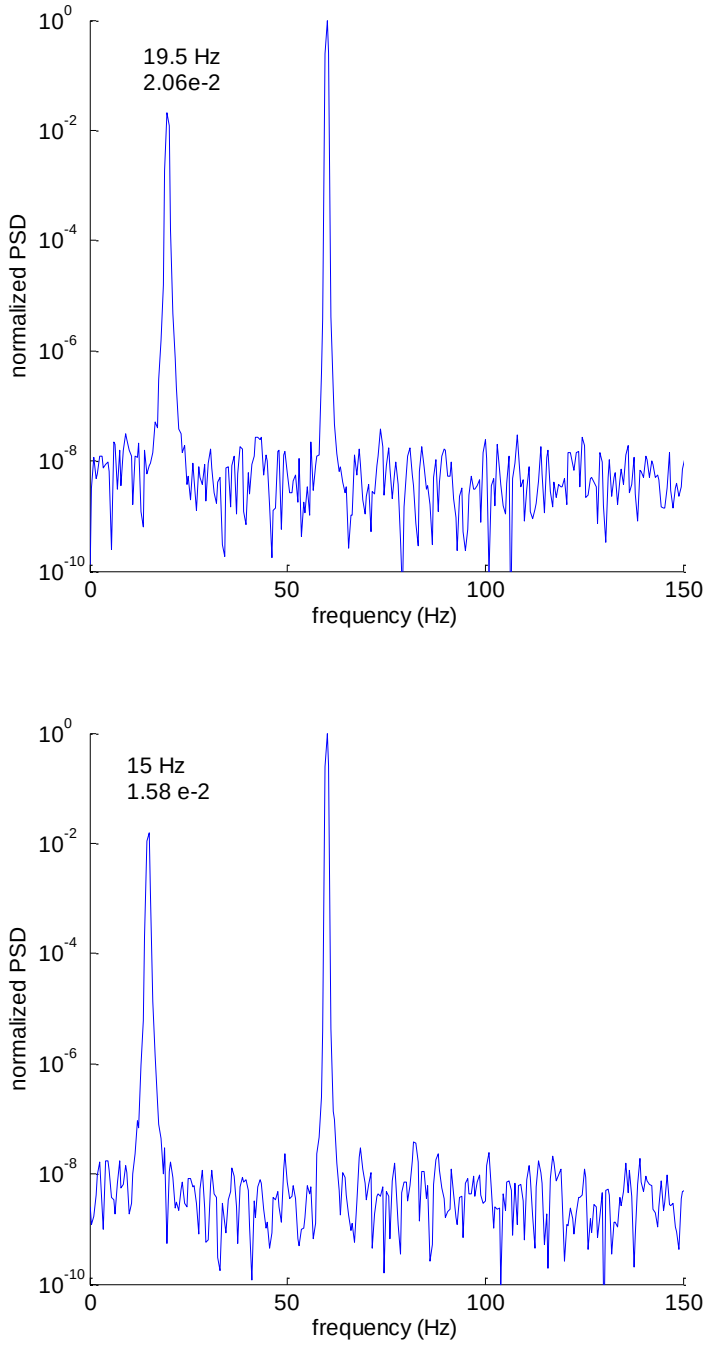

Figure 3.10 Continued.

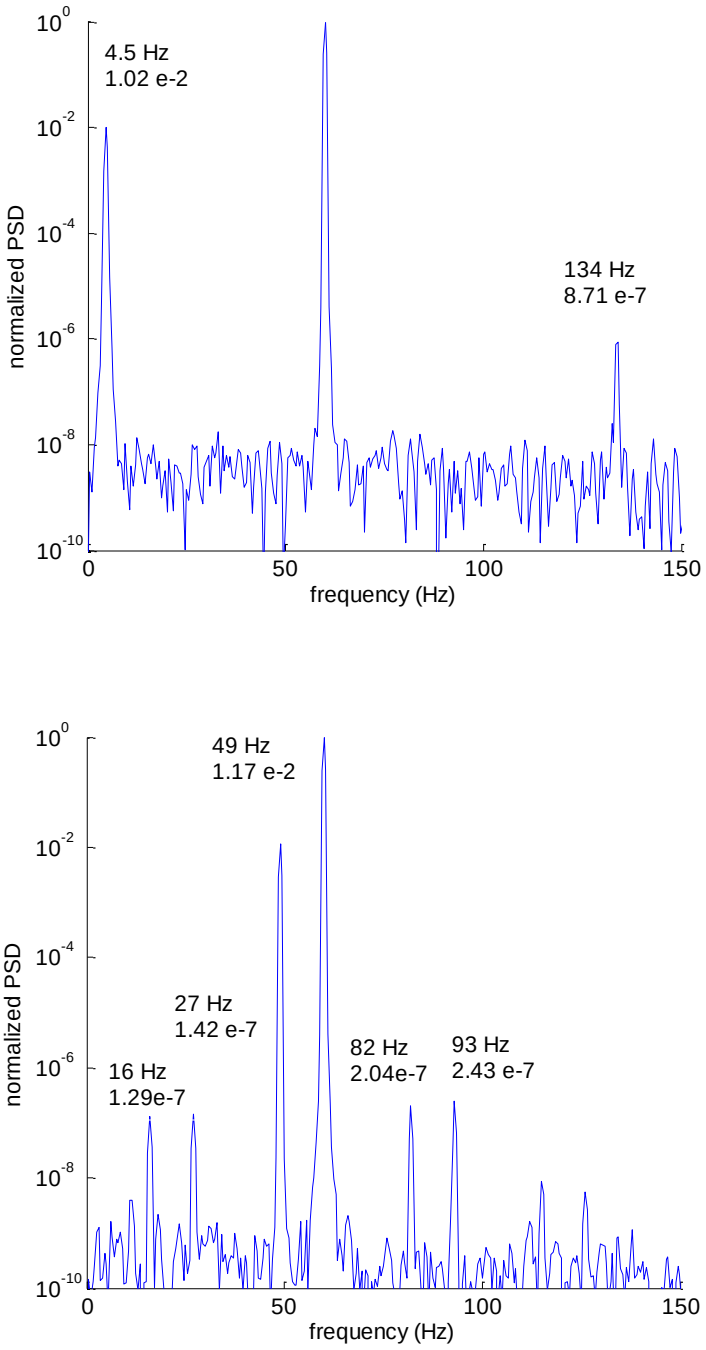

Figure 3.10 Continued.

3.3.1 Magnitude of the Left Side Band Component

For diagnosis of rotor bar failure in the cage induction motors, detection of the side band frequency is a reliable sign of rotor failure. That is why in the literature it has been mainly focused on the different techniques of signal processing to detect this signal. There have been limited studies on the variation of the sideband component magnitude with the number of broken bars. They have found that the magnitude of the LSBC increases almost linearly with the fault severity assuming the slip is near its rated value and the number of broken bars is low [56, 57].

As shown in the previous sections the LSBC which is known as the broken rotor bar signature in an induction machine does not indicate a fault in the damper winding of a synchronous machine because it always exists in the spectrum. A further investigation of the magnitude of the LSBC is needed in order to distinguish the healthy and faulty damper winding. The current spectra presented in subsection 3.3 show that in the asynchronous steady state operation, the magnitudes of the LSBC do not follow a clear pattern as the number of broken bars increases. An analytical justification for this behavior is presented in section 5 which shows that the left side band magnitude is proportional to $|1-2s|$.

Fig. 3.11 shows the simulation results of variations of the stator current LSBC amplitude with the number of broken bars under different load conditions. The slip corresponding to each fault and load conditions of this figure can be found in Fig. 3.12. The LSBC amplitude with 32.5% and 5 broken bars is very low. The reason is that the slip corresponding to this condition (see Fig. 3.12) is close to 0.5, which make the slip

factor |1-2s| close to zero. The same situation exists with 40% load and 4 broken bars. At 40 % load and 5 broken bars, the slip is well above 0.5 and |1-2s| becomes larger pulling the LSBC amplitude up.

Therefore, the assumption of higher LSBC amplitude at the presence of more severe fault is not valid in the case of the damper winding. This makes the broken damper bar diagnosis based on the LSBC not reliable unless some prior analysis is done based on the slip variations and the geometry of the damper winding.

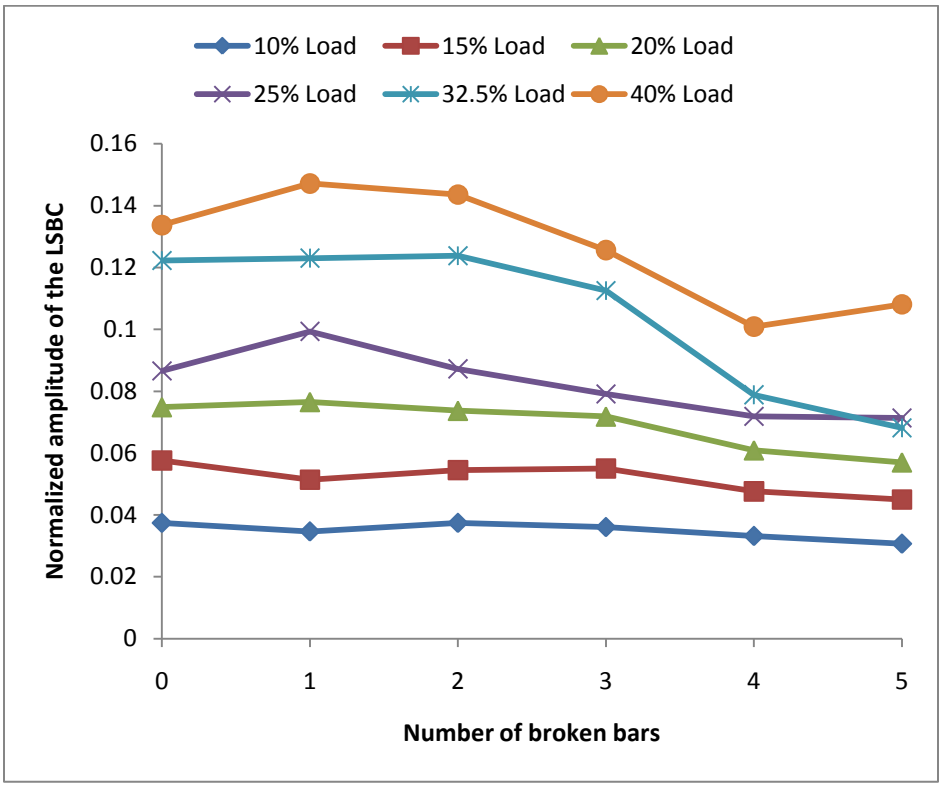

Figure 3.11 Variations of the left sideband frequency amplitude with the number of broken bars for different loads.

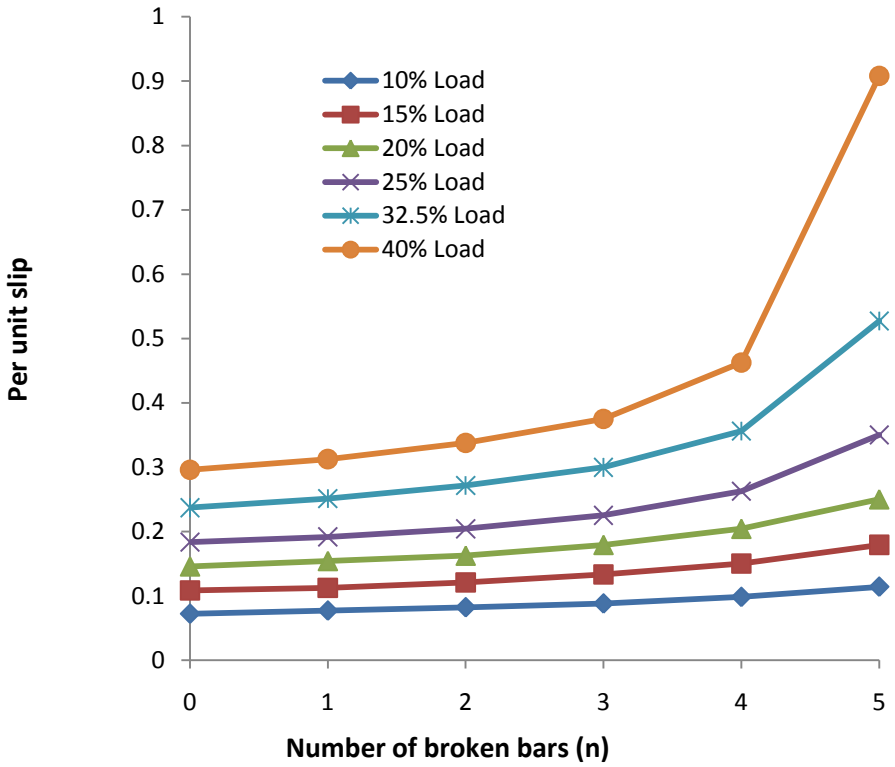

Figure 3.12 Variations of per unit slip with the number of broken bars for different loads.

Fig. 3.12 shows the slip variations as the damper bar failures expand from bar #1 to bar #5 for different loads. Under a constant load condition, the variation of slip depends on the number of broken bars. When the motor is lightly loaded, the slip increases almost linearly as the number of broken bars increases. At heavier loads however, the slip changes almost exponentially. An abrupt slip change can be observed when the 5th bar is broken at higher loads. Because when the 5th bar is broken one pole is completely failed. A big mesh will be created which is wider than a pole pitch. As the width of a mesh increases there will be more flux linked to the mesh, inducing higher

current. This is true as long as the mesh width is smaller than a pole pitch (π electrical angle). When the mesh expands over π, the field goes to the negative half cycle and the current induced in the faulted mesh drops. Therefore, when the failure expands to the 5th bar, in addition to the 5 missing field components, the induced current will also be reduced causing a poor rotor magnetization leading to a long transient time and a high slip.

3.3.2 Analysis of Speed Spectral Component

It is well known in the literature that the current spectral component of (1-2s)f produced by rotor asymmetry, generates 2sf torque component and consequently speed ripple [51-53]. This ripple appears in the speed spectrum at 2sf and can be used as a fault signature. In the case of the induction machines it has been shown that the increasing number of broken rotor bars leads to the increase of the speed spectral component amplitude at 2sf [58]. However, in synchronous machines with broken damper bars, the variation of 2sf component does not follow the same pattern. Fig. 3.13 presents the simulation results of the speed spectrum showing the 2sf spectral component for different fault conditions under 10% load. The motor slip corresponding to each case is given in Table 3.1. It can be observed that the speed spectral component due to asymmetry is at exactly located at 2sf which agrees to the theoretical value. It is worth mentioning that this component exists in all cases including the case of the healthy damper winding. Therefore, detecting the 2sf component does not necessarily indicate a

fault. The next component of 4sf is also visible but its amplitude is much smaller than the main speed spectral component.

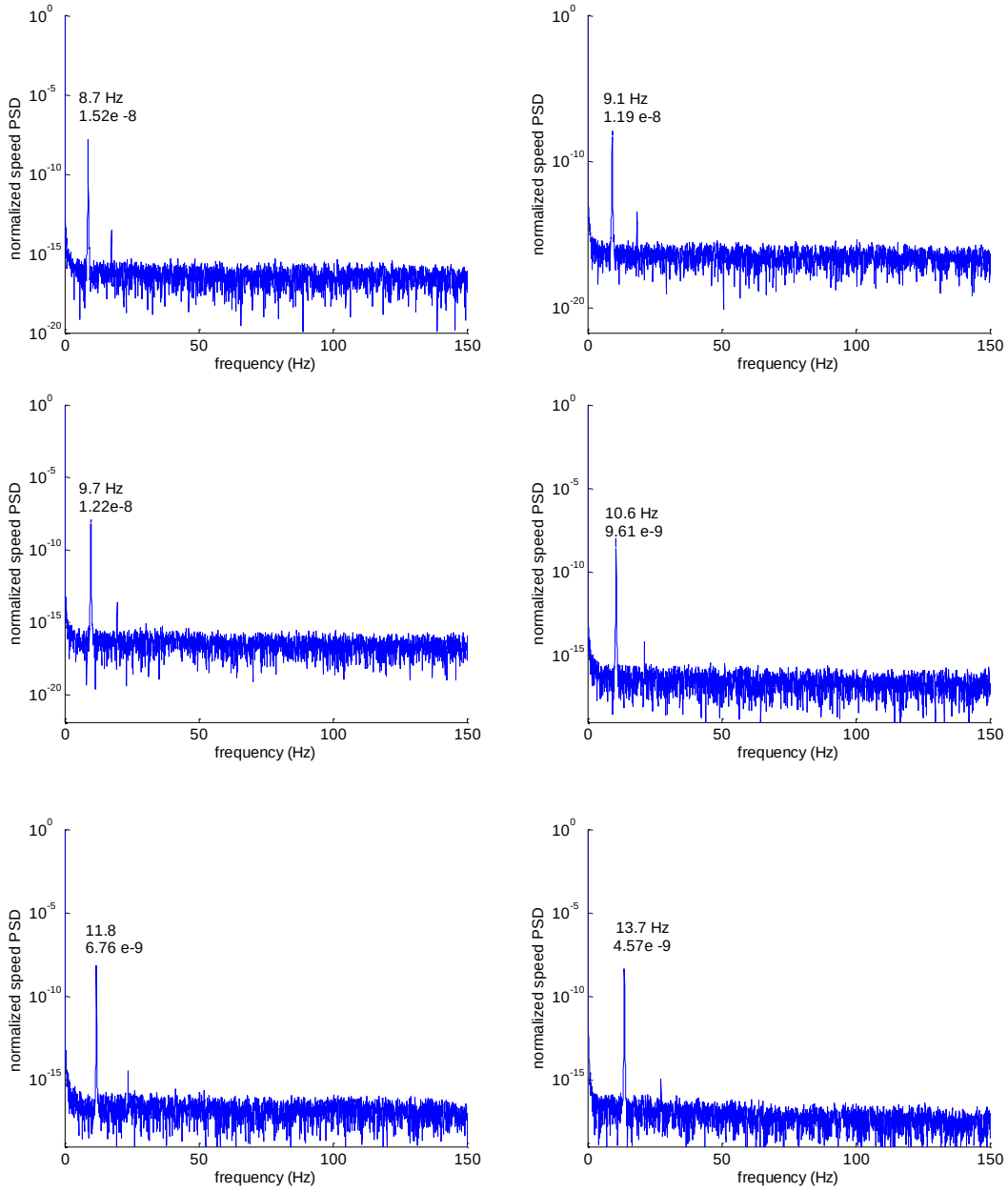

Figure 3.13 Speed spectra with 10% load. Top figure to bottom: healthy, 1 broken bar to 5 broken bars.

3.3.3 Effect of Fault on the Torque Speed Curve

The existence of the speed dependent components in the current spectrum of the faulted rotor is expected to affect the torque speed curve of motor. To the best of the author's knowledge there is no research publication on how a rotor failure influences the torque-speed curve. When there is an asymmetry in the rotor, the left side band component of the current at (1-2s)f is the highest magnitude next to the fundamental. Considering only this component of the current, it is expected that as the rotor speed increases toward its 50% rated value, corresponding to s = 0.5, the amplitude falls to zero [59]. The reason is that at this speed the fault related negative rotating field which revolves at speed |(1-2s)f| with respect to stator, becomes zero, inducing no current in it. As the rotor speed increases further, the speed of the negative rotating field rises, leading to higher magnitude of the left side band component.

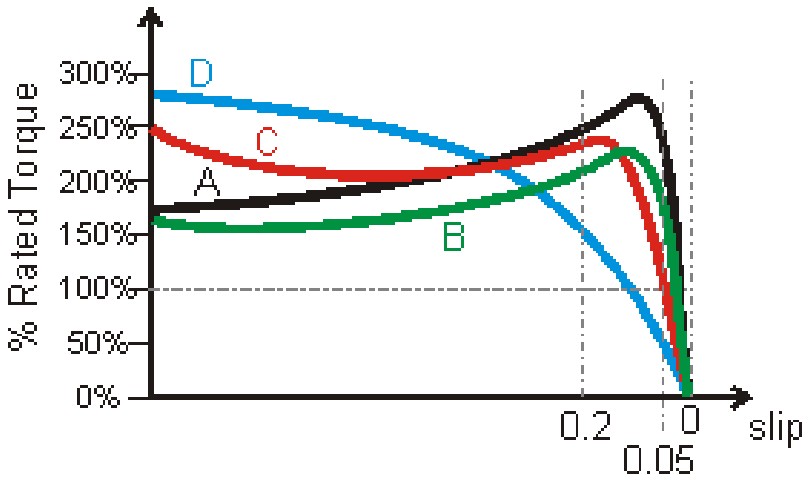

Figure 3.14 Typical torque speed curves for class A to D. (Andy Knight's lecture, University of Alberta)

The particular synchronous motor which has been studied in this research, when running with no field excitation as an induction motor, has the characteristics of the "class D" induction motors. Since different applications require different characteristics of induction motors, the National Electrical Manufacturers Association (NEMA), has specified different classes of induction motor, with different characteristics and torque-speed curves as shown in Fig. 3.14. "Class A" is designed to have low rotor resistance and "class D" has a high rotor resistance. Classes B and C are designed to have variable rotor resistances by utilizing the effect of skin depth. "Class D" motors have high starting torque, high slip and low efficiency which are used for high inertia applications such as punch.

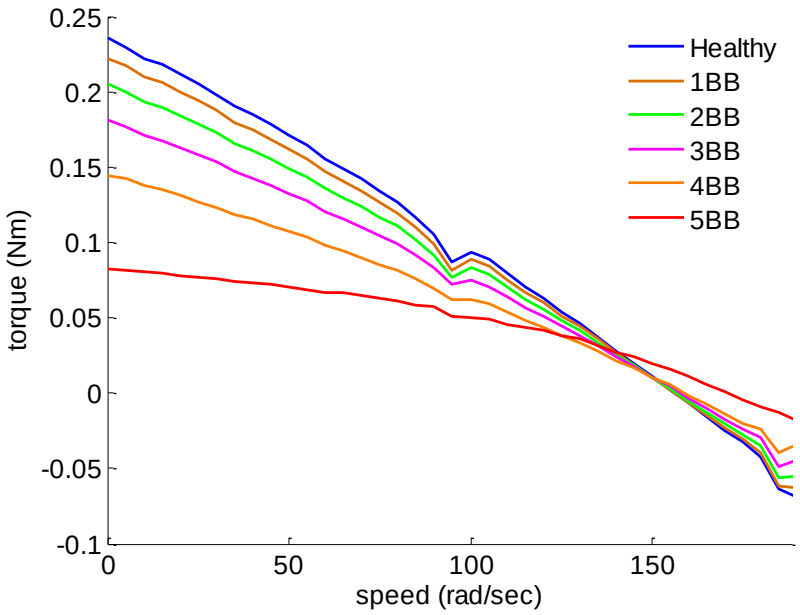

Figure 3.15 Torque speed curves of the synchronous motor under study. (without field excitation with healthy and 1-5 broken damper bars)

The torque-speed curves of the studied synchronous machine, at startup asynchronous operation are derived for the healthy and 1-5 broken damper bar conditions. As shown in Fig. 3.15, the motor has a "class D" torque-speed curve. These curves show that the starting torque falls as the number of broken increases. There are two dips in the torque-speed curves at 50% and 100% speeds which are due to the rotor asymmetry. At 50% speed, corresponding to s = 0.5, the magnitude of the fault related current component of (1-2s)f is zero, and at full speed this component disappears because it would be no different than the fundamental frequency f. Fall of the magnitude of this component to zero pulls down the torque at half and full speeds.

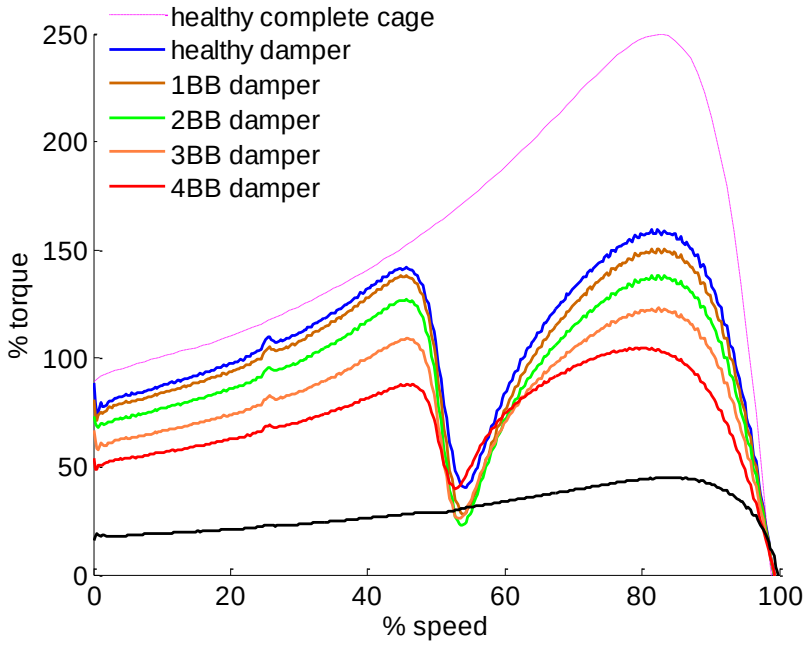

Figure 3.16 Torque speed curves of "class A" synchronous motor. (no field excitation with healthy and 1-5 broken damper bars compared to the torque-speed curve of a healthy cage rotor induction motor having the same parameters.

To investigate the effect of fault on the torque-speed curve of a synchronous machine when running without field excitation as a “class A” induction motor, the damper bar resistance is reduced in Matlab program. The calculated torque-speed curves of such a motor are presented in Fig.3.16. The dashed line in this figure shows the torque-speed curve of a healthy cage induction motor having the same parameters. In other words, it is the same machine with the missing bars added to the damper winding to make it a complete cage.

The dips in the torque-speed curves of “class A” synchronous motor are deeper, compared to “class D”. Since in this case the damper bar resistances are lower, a bar breakage which is an effective large resistance, seems a more severe change to the motor compared to “class D” with higher bar resistances. This leads to higher amplitude of the LSBC of the current spectrum causes the torque to drop severely. It should be noticed that in the case of a complete damper winding (cage induction motor) there is no dip in the torque-speed curve, because the rotor has a perfect symmetry and there is no side band component at (1-2s)f to pull it down at half speed.

Now let’s investigate the torque-speed curves of a cage induction machine with healthy and faulty rotor bars. Again the induction machine has the same parameters as the synchronous machine under study with its bar resistances reduced (to make it a “class A” motor), its field winding open. Some extra bars are placed in the gaps of the damper winding to make it a complete and symmetric cage with 9 bars per pole. The torque-speed curves of such an induction motor are shown in Fig. 3.17.

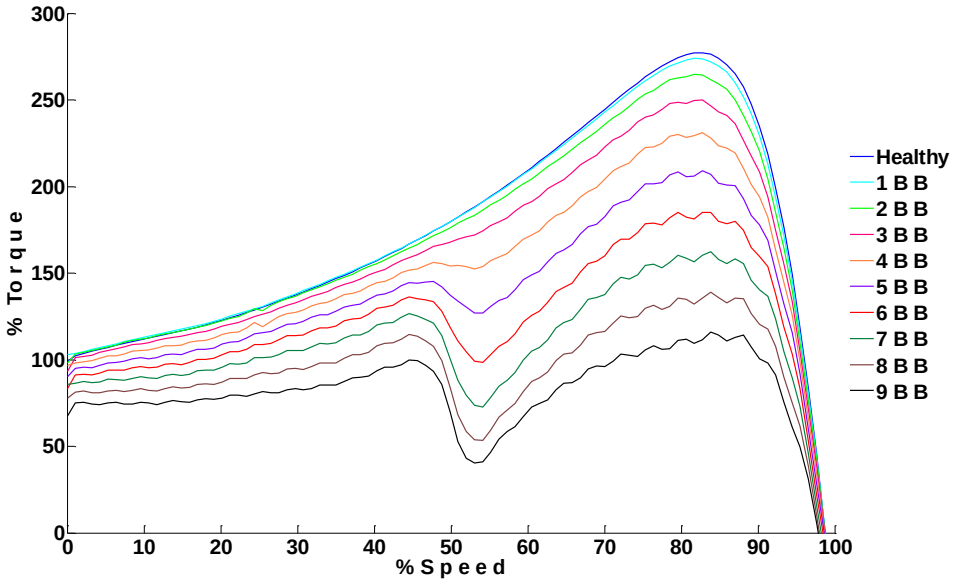

Figure 3.17 Torque speed curves of induction motor with 9 bars per pole under healthy and 1-9 broken rotor bar conditions.

The fault signature of an induction machine with broken rotor bars is known to be the current spectral sideband components around the fundamental frequency. It has been shown in the literature that more severe fault in the rotor leads to higher magnitude of the fault signature and also higher magnitude of the 2sf spectral component of rotor speed. These phenomena are reflected on the torque-speed curve as well. The increasing side band component magnitude creates bigger dip as the number of broken bars increases. Similarly, the increasing oscillation of the torque is due to the increasing of the speed spectral component at 2sf with higher fault severity.

3.4 Conclusions

There are four possible operational conditions that the damper winding of a synchronous motor comes in to effect: startup transient, field excitation transient, load change transient and asynchronous steady state operation. For analysis of damper bar failure the motor signals can be investigated at each of these operational conditions. In this subsection the simulation results of the stator current time-frequency analysis during three different transient conditions were studied using Short Time Fourier Transform (STFT). The stationary signal of the stator current at asynchronous steady state was examined through Fast Fourier Transform (FFT). The spectral components found during transient agreed with the expected theoretical components but were not easy to establish a metric indication of the rotor condition. In the asynchronous steady state, the LSBC was found to be present in all healthy and faulty cases of damper winding and the amplitude variation of this spectral component with the number of broken damper bars did not have a clear pattern. However the transient time and rotor slip were directly correlated with the fault severity. The speed spectral component at 2sf was also present in the healthy and faulty cases.

The effect of damper bar failure on the torque speed curve was studied for different fault severities. The torque speed curves were calculated with no field excitation for “class D” and “class A” synchronous motors. For deriving the torque-speed curve of an induction motor the damper winding was modified to the form of a symmetric complete cage to resemble an induction motor with the same parameters.

4. EXPERIMENTAL RESULTS OF THE DAMPER WINDING FAILURE ANALYSIS

4.1 Introduction

The effects of the damper bar breakage were studied in section 3 through simulation using the model described in section 2. In this section some experimental results will be presented and discussed. An inverted synchronous motor with damper winding is designed for the experimental setup.

4.2 Inside-Out Synchronous Machine

To measure and analyze the signals of a synchronous machine with defected damper winding, a special inside-out synchronous machine (IOSM) was built. The armature windings of the IOSM are wound on the round rotor, connected to the supply via slip rings, and its field winding is mounted in some of the stator slots. The copper bars of the damper cage are placed in the remaining stator slots aligned with the pole faces. The IOSM was originally a 0.1 kw, 1800 rpm, doubly fed induction motor. The original three phase winding on the rotor was used as the armature winding and remained unchanged. The stator winding, was removed and replaced with a field winding in some of the stator slots. A copper damper cage was built to be placed in the remaining stator slots. The cage end ring was fixed on one side and is removable on the

other side. This made it possible to disconnect any of the bars from the end ring for the broken bar test. Fig. 4.1 shows different parts of the special IOSM.

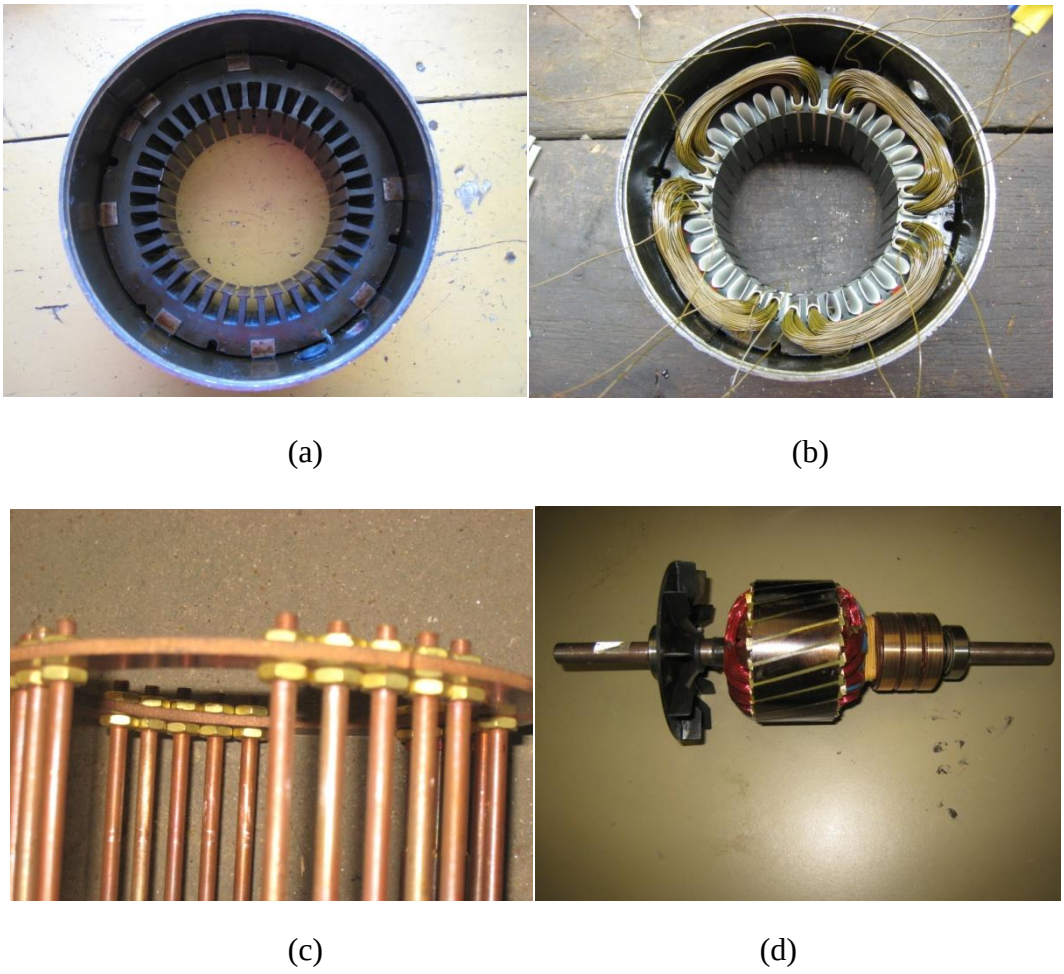

(a) (b)

(c) (d)

Figure 4.1 Different parts of IOSM. (a) stator of the original doubly fed IM with its winding removed, (b) new field winding on the stator, (c) damper cage with the removable end ring for broken bar experiment, (d) original rotor windings used as the armature windings of the IOSM.

The machine has 4 poles, 36 stator slots, 24 rotor slots and 20 damper bars. The winding configurations of the field and armature windings are presented in section 2. The assembled IOSM is shown in Fig. 4.2. As shown in this figure the damper winding is made longer than the motor to be brought out of the motor end bell for the easy accessibility.

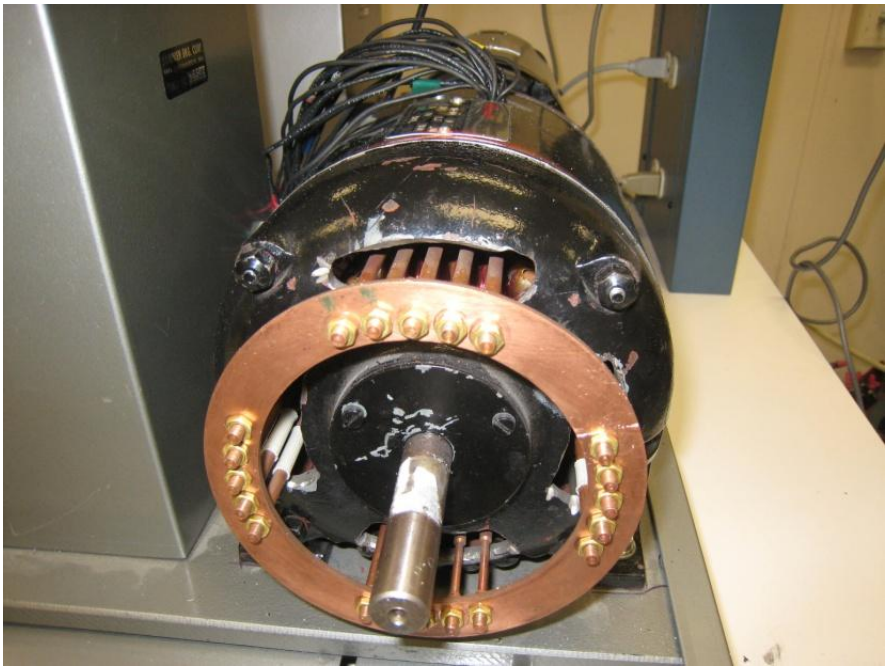

Figure 4.2 Assembled inside-out synchronous motor.

To introduce a breakage on a bar, it should be electrically disconnected from the end ring. The bar is unscrewed from the end ring and an insulator sleeve wrapped around the bar disconnects it from the ending.

4.3 Experimental Setup

Fig. 4.3 shows the experimental set up consists of an inside out synchronous motor with damper winding, 3-phase transformer, hysteresis breaks, torque meter, shaft encoder and data acquisition card connected to a computer. The armature windings of the IOSM are supplied from a 3-phase transformer which is connected to the line voltage, and the field winding is connected to the dc power supply. A braking torque is applied on the motor shaft by the hysteresis break which is measured by the torque meter. The shaft encoder is fed from a dc power supply and is used to measure the rotor speed.

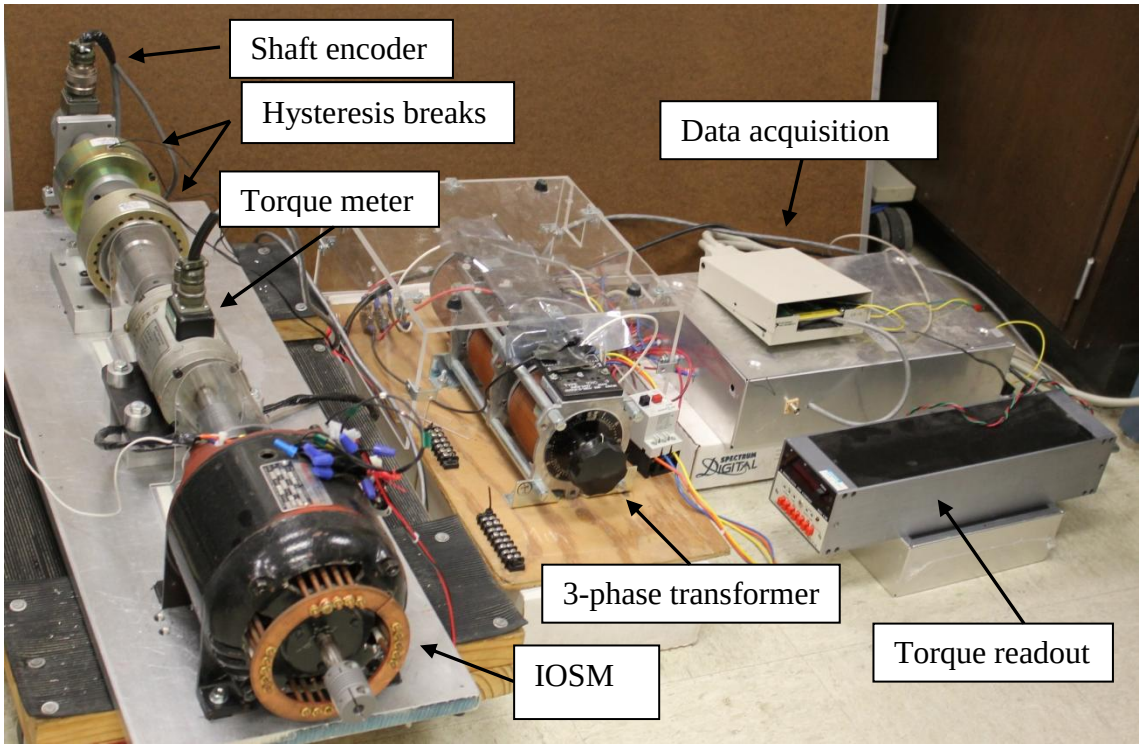

Figure 4.3 Experimental setup.

4.4 Experimental Results during Transient Operations

The time domain armature current at startup with no field excitation is expected to start with a high current and then decrease to the steady state value. As the rotor speeds up the slip is reduced and in the equivalent circuit the rotor resistance r/s increases leading to lower current at steady state.

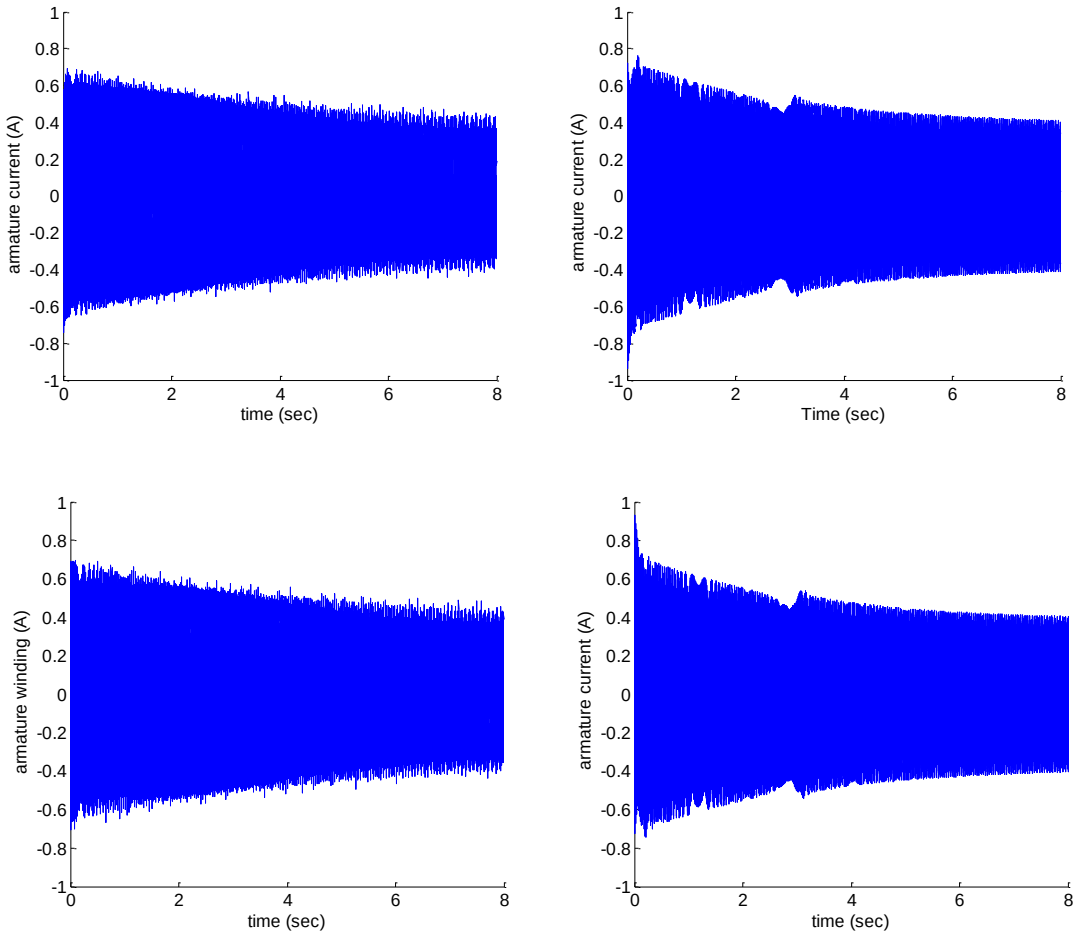

Figure 4.4 Armature current at startup, no-field, under 10% load. (left) experimental, (right) simulation, top to bottom: healthy, 1bb and 4bb.

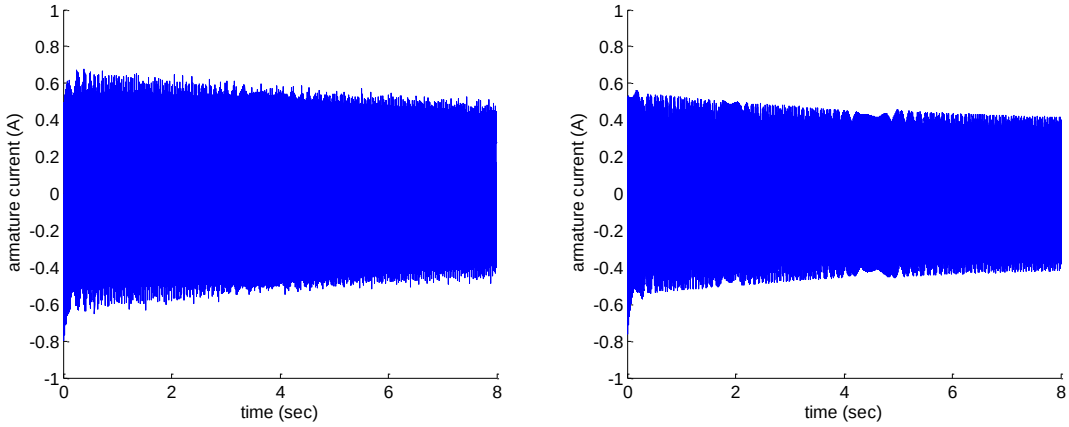

Figure 4.4 continued.

Fig. 4.4 shows the measured and simulated transient motor current at startup for the healthy, 1 and 4 broken bar cases. The simulation and experimental transient currents are in close agreement with each other in terms of the both the initial and the steady state amplitude. They are also similar in terms of the transient time.

It was shown in the previous subsection that the rotor slip increases with fault severity especially when the motor is heavily loaded. This will affect the time domain armature current as well. It was found that the effect of load on the time domain current is more noticeable at steady state. The motor current at different load conditions have the same magnitude at startup but at steady state the higher load draws more current. This is true for any fault condition. The currents corresponding to the healthy and 3 broken damper bars are presented in Fig. 4.5 for 10% and 40% load conditions.

For the same load conditions, the time domain currents in the healthy and faulty motors seem to have the same magnitude at the steady state. However, at startup a

healthy motor have a higher current. This behavior is shown in Fig. 4.6 for healthy and 3 broken damper bar case, when loaded with 10% and 40% of the rated value.

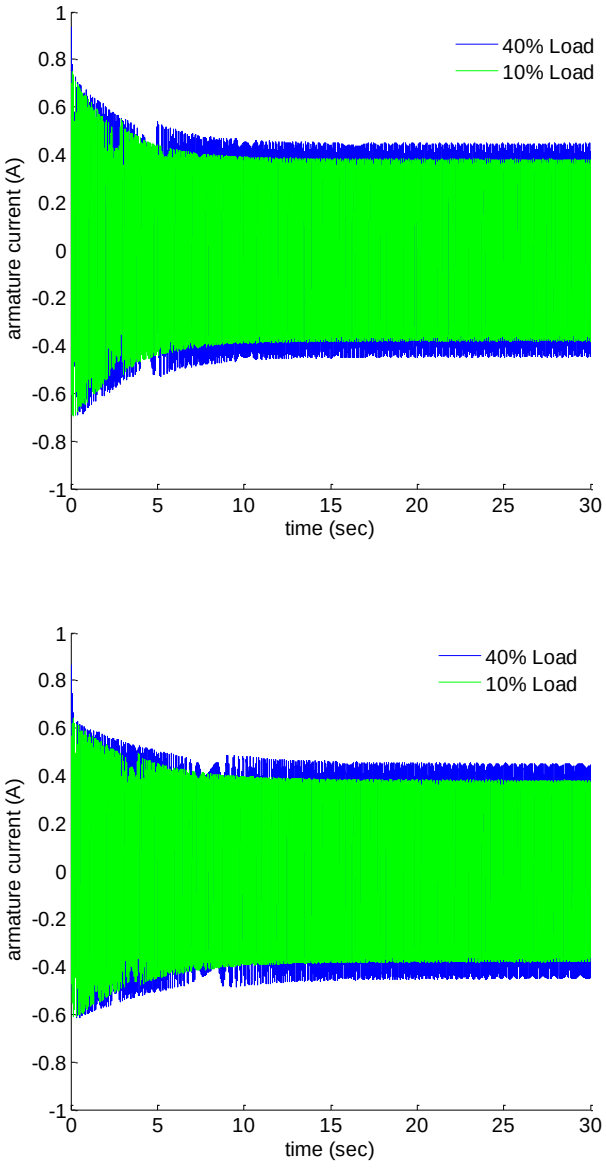

Figure 4.5 Effect of load on the time domain current. (top) healthy damper, (bottom) 3 broken damper bars.

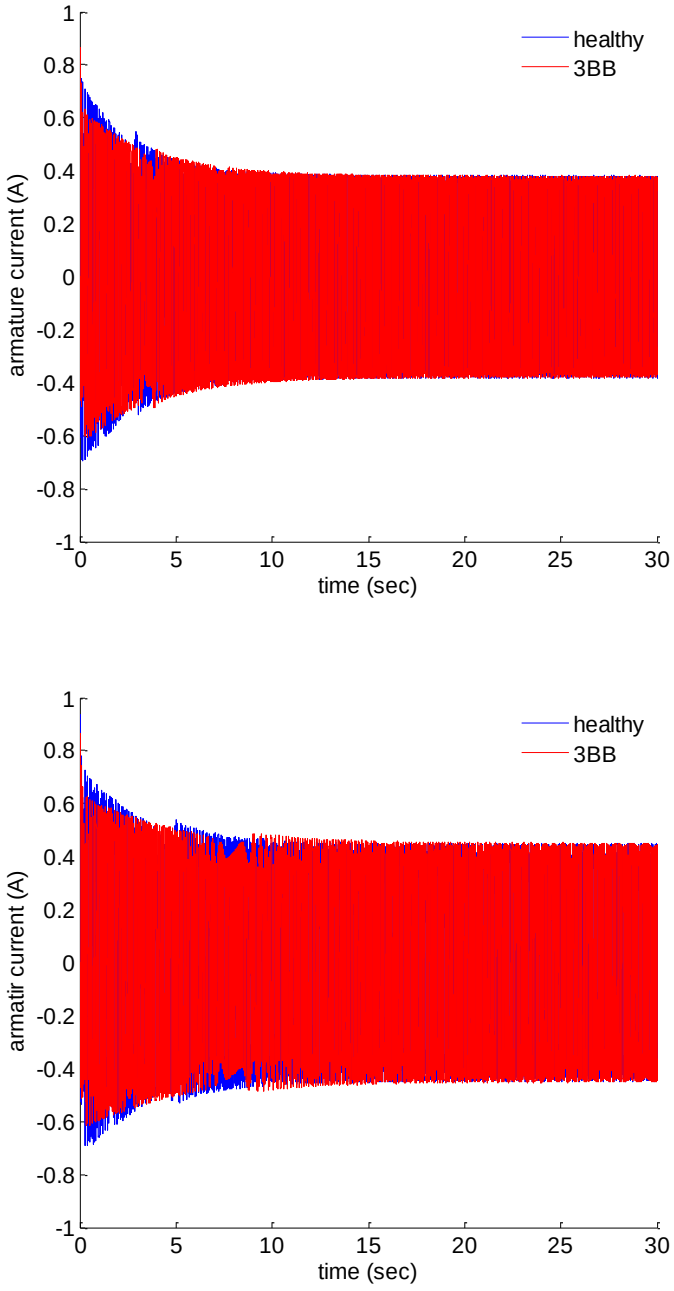

Figure 4.6 Effect of fault on the time domain current. (top) 10% load, (bottom) 40% load.

For the frequency analysis during transient the motor current data was acquired to be used for Short Time Fourier Transform (STFT) analysis. Due to the memory limitations a low sampling was selected for a few seconds of data. Fig. 4.7 presents a 3-dimmentional spectrogram for the healthy and 3 broken damper bar cases. Compared to the calculated spectrograms in section 3, there are more harmonics exist in this figure. In practice there are many imperfections in the motor, especially in the IOSM used for experiment. The non-idealities that are not included in simulations are: saturation, slotting effect, slightly unbalanced supply, air gap eccentricities and other poor manufacturing or operation conditions.

The main spectral component corresponding to the rotor asymmetry is the left side band of the fundamental component which is observed in the spectrograms. Also the sidebands of the 5^{th} and 7^{th} harmonics, starting from –f and propagate toward 300 and 420 Hz, exist in the spectrograms. The LSBC in the 4bb case has lower amplitude compared to the healthy case, but a certain pattern cannot be established for all fault cases. As discussed in section 2, even in the healthy case, the LSBC exist due to the non-uniform structure of the damper winding. This behavior was observed in the simulation results and is also confirmed by the experimental results.

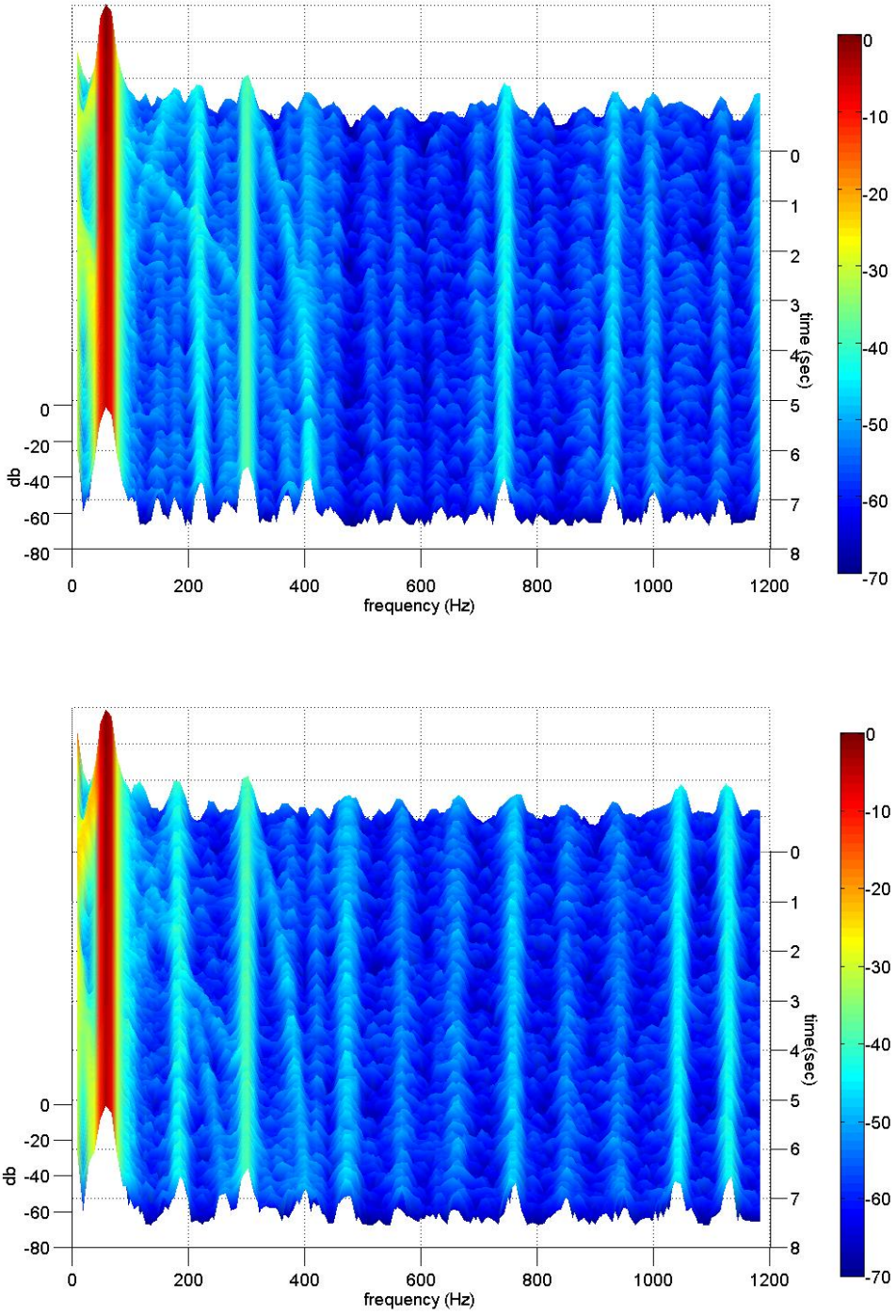

Figure 4.7 Experimental STFT during startup transient. (top) healthy, (bottom) 3bb.

For the field excitation transient, the motor is started with open field. When the rotor speed nears the synchronous speed, the field winding is connected to the dc power supply. At this time motor current data are acquired for time-frequency analysis. After a very short transient time the rotor locks into the synchronous speed. Then a full load torque is suddenly applied using the hysteresis break. The motor current data are acquired right after applying the load torque and used for the STFT.

The experimental spectrogram of the healthy and 3 broken bar cases are shown in Fig. 4.8 for the field excitation transient and in Fig. 4.9 for the load change transient. As discussed in the case of the startup transient, there are some extra frequency components in the experimental spectrograms due to the imperfections of the experimental motor. Since when the field is being excited the rotor speed is already close to the synchronous speed, the slip is very small at the beginning. This moves the LSBC of (1-2s)f very close to the fundamental component making their separation difficult. That is why the LSBC is not visible even at the beginning. The next significant components which are the 5^{th} and 7^{th} harmonics can be observed in the spectrograms. During the short transient period some oscillations are observed due to sudden application of the field current. This behavior was detected in the simulation results as well. For some spectral components these fluctuations are superimposed on the harmonics generated by motor non-idealities. These harmonics mask some of the fluctuations in the especially in the lower order harmonics.

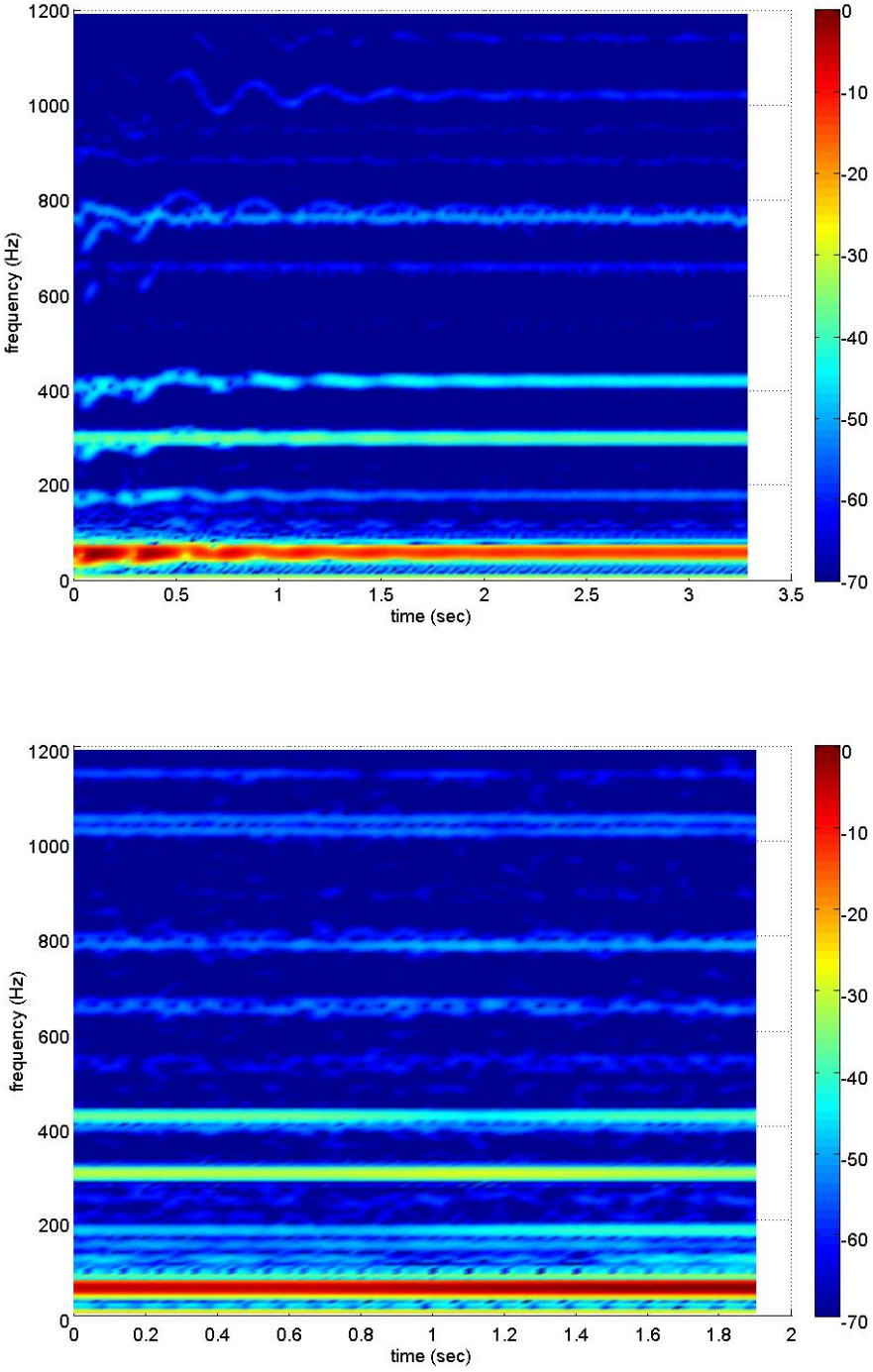

Figure 4.8 Experimental STFT during field excitation transient. (top) healthy, (bottom) 3bb.

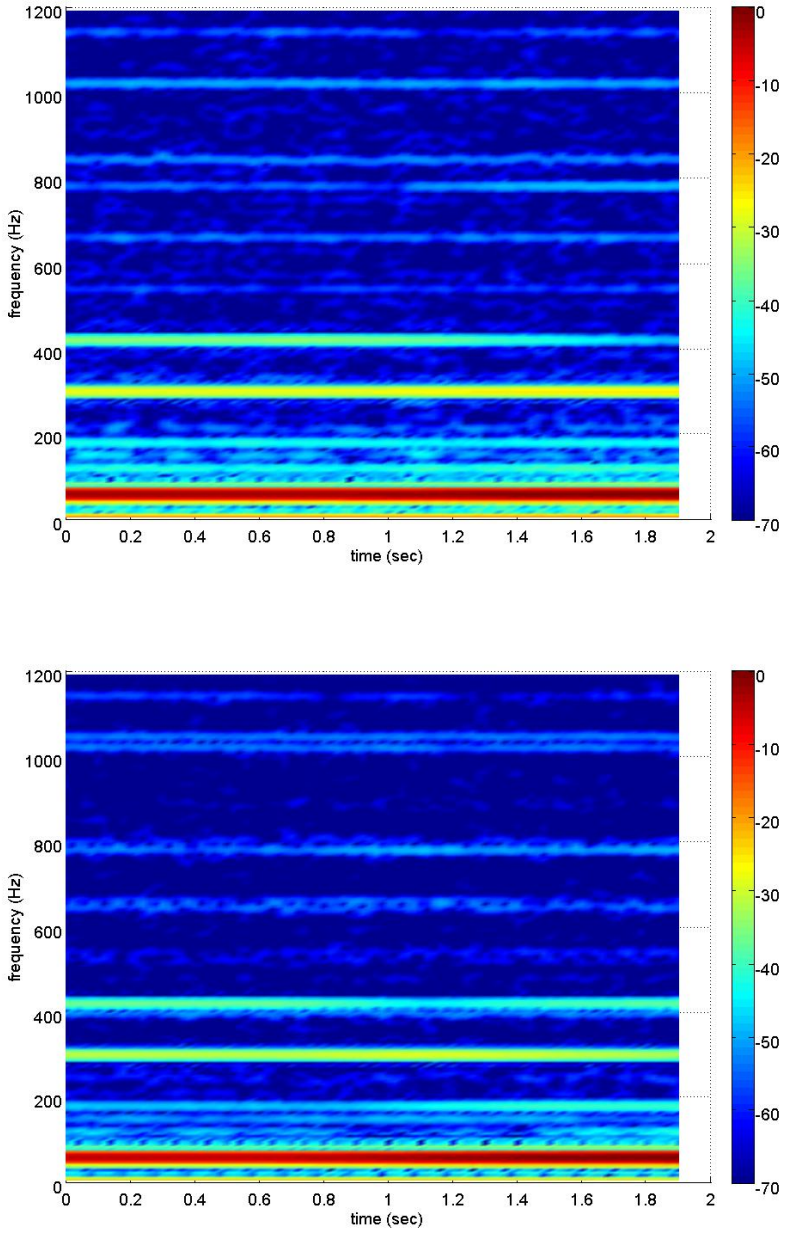

Figure 4.9 Experimental STFT during load change transient. (top) healthy, (bottom) 3bb.

4.5 Experimental Results at the Steady State Asynchronous Operation

If the field winding of the synchronous machine is not connected to the supply, the machine will operate like an induction machine and can never reach the synchronous speed. The machine will be running with a constant slip depends on the load and machine parameters. Since damper winding failure changes the rotor parameters, it will affect the rotor slip as well. In this subsection the experimental results of the motor current spectrum are presented. Figure 4.10 compares the measured and calculated current spectrum of the healthy and 1 broken bar cases under 15% load. It shows that the left side band frequency decreases due to the slip increase in the faulty case. Although the synchronous motor in this mode of operation is similar to an induction motor, their LSBC amplitude behaviors for different cases of bar failures are not similar. It has been shown in the literature that the fault signature amplitude increases with number of broken bars in a cage rotor induction machine, if the number of broken bars is small compare to the number of bars per pole. However in the synchronous machine with broken damper bar, this is not necessarily true. The detailed analysis of this behavior will be presented in section 5.

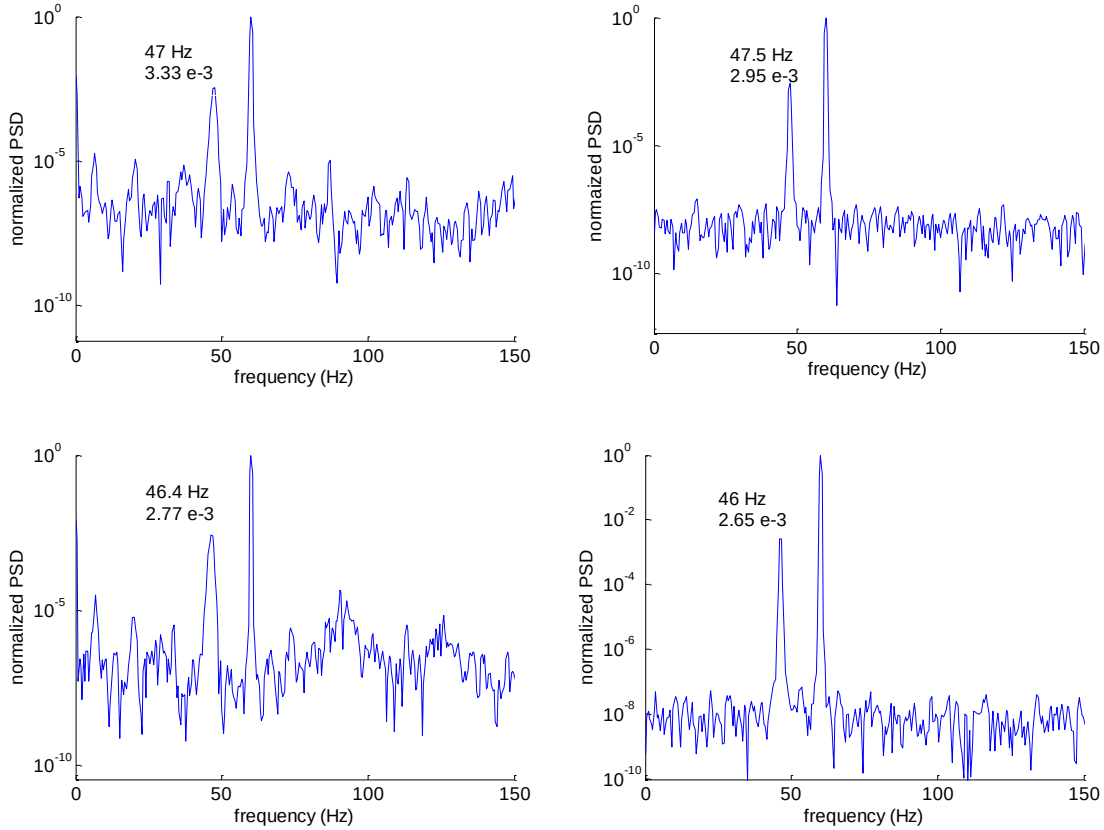

Figure 4.10 Experimental (left) and calculated (right) current spectrum. Top figure to bottom: healthy and 1 broken bar, 15% load.

The variation of the normalized LSBC amplitude and the corresponding rotor slip with the number of broken bars are shown in Fig. 4.11. The discrepancy between the simulation and experimental results is due to the intrinsic manufacturing asymmetry like eccentricity, shaft misalignment and slight difference between the reactance and resistance of the individual damper bars. Unlike the LSBC amplitude, the slip variation with the fault severity shows an upward trend as the number of broken damper bars increases.

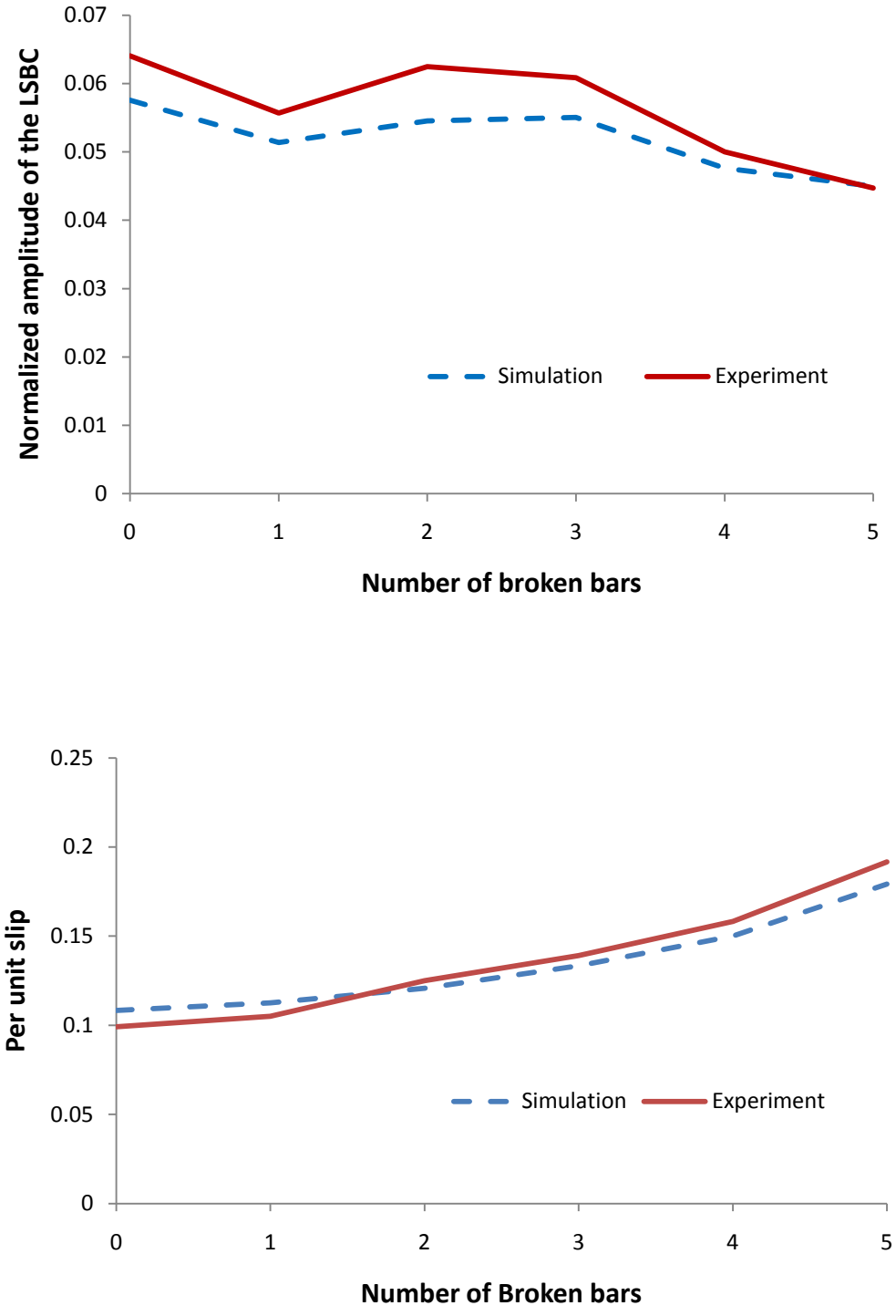

Figure 4.11 Simulation and experimental results under 15% load. (a) normalized LSBC amplitude, (b) per unit slip.

4.6 Conclusions

The experimental results of several tests with different damper fault conditions confirm that even with a healthy damper winding the left side band component of the fundamental frequency in the motor current spectrum exists. Therefore, as oppose to the case of an induction machine rotor bar failure, this component cannot be used as a fault signature. The presence of this component is not sufficient for detection of the damper bar failures. It requires further knowledge of the LSBC amplitude which will be discussed in section 5. The variation of the LSBC component amplitude does not have a specific trend as the number of broken damper bars increases. The rotor slip however, shows an increasing pattern with increasing fault severity.

5. ANALYTICAL APPROACH OF CORRELATING THE LEFT SIDE BAND COMPONENT AMPLITUDE WITH THE FAULT SEVERITY

5.1 Introduction

It was shown in the previous sections that the left side band component (LSBC) cannot be used as a feature to detect damper winding failures because it always exists in the current spectrum due to the non-uniform structure of the damper winding. Further knowledge about the correlation of the LSBC amplitude with the number of broken damper bars is needed.

It has been shown in many diagnostic research publications that any asymmetry in the cage rotor of an induction machine leads to the LSBC in the stator current spectrum [51-52]. The frequency of this speed related component is known to be at (1-2s)f. However, there are not many publications on the quantitative evaluation of the amplitude of the LSBC as a function of the number of broken bars. To the best of the author's knowledge, there is no research publication about this correlation for the damper winding of a synchronous machine.

In this section, a novel approach of deriving the amplitude of the LSBC as a function of the number of broken bars is presented. This method is based on fundamental electromagnetic field theory and the characteristics of the multi-phase unbalanced circuits. The derivation is inclusive and can be applied to the cage induction machine as well as synchronous machines with damper windings.

5.2 Rotor Asymmetry and the Backward Rotating Field

A three phase symmetrical stator winding fed from a balanced three phase supply will produce a forward rotating magnetic field in the air gap at synchronous speed. The existence of any asymmetry will result in a backward rotating field component. This can be applied to the rotor winding of an induction machine as well. The difference is that the induced electromotive force (emf) in the rotor circuit is at slip frequency. The induced currents in a cage rotor winding results in magnetic field rotating at slip frequency with respect to the rotor. In the case of rotor asymmetry, a backward rotating field at slip frequency (-sf) will appear. This backward rotating field will induce an emf in the stationary stator winding at (1-2s)f. This is known as the left sideband component of the stator current spectrum due to broken rotor bars. The left sideband component represents the cyclic variation of current and results in torque pulsation at 2sf which in turn creates speed oscillation at the same frequency. Due to this rotor speed oscillation a right sideband at (1+2s)f will be induced in the stator winding which is a function of the inertia [3, 51, 55].

The left sideband component of the stator current is known as the broken bar signature in motor current signature analysis (MCSA) for fault diagnosis. Extensive work has been developed on the subject of detecting this component for broken rotor bar diagnosis in induction machines. However, the quantitative correlation between the fault severity and amplitude of the left sideband component still needs to be investigated. Some relations are given in [56] without any explanation and derivation. Also a model based equation is developed to link the amplitude of the sideband component and the

fault severity in [57]. For deriving such correlations, some assumptions were involved such as small number of broken bars with respect to the number of bars per pole, neglecting the end ring impedance and the slip being close to the rated slip. Therefore, it is not valid for severe fault cases when there are several broken bars or higher rotor slip.

5.3 Fault Signature Amplitude Derivation

A novel method has been developed that correlates the amplitude of the LSBC with the fault severity. This method is based on the fact that any rotor asymmetry produces a current spectral component at (1-2s)f. Therefore, the derivation is focused on the effect of this component on the LSBC.

5.3.1 Current Induced in a Faulted Rotor Mesh

Consider a symmetric cage rotor, having N bars with angular distance $\alpha=2\pi/N$ between any two adjacent bars, as shown in Fig. 5.1a. The rotating magnetic field B moving against a rotor mesh is shown in Fig 5.1b. At steady state, the sinusoidal air gap field is rotating at frequency sf with respect to the rotor mesh and can be expressed as:

$$B(\theta,t) = b\,cos(\ p\theta - 2\pi sft) \tag{5.1}$$

where, b is the amplitude of the rotating field produced by the symmetric stator current in the air gap, p is the number of pole pairs, θ is the mechanical angle, s is the rotor slip and f is the excitation frequency.

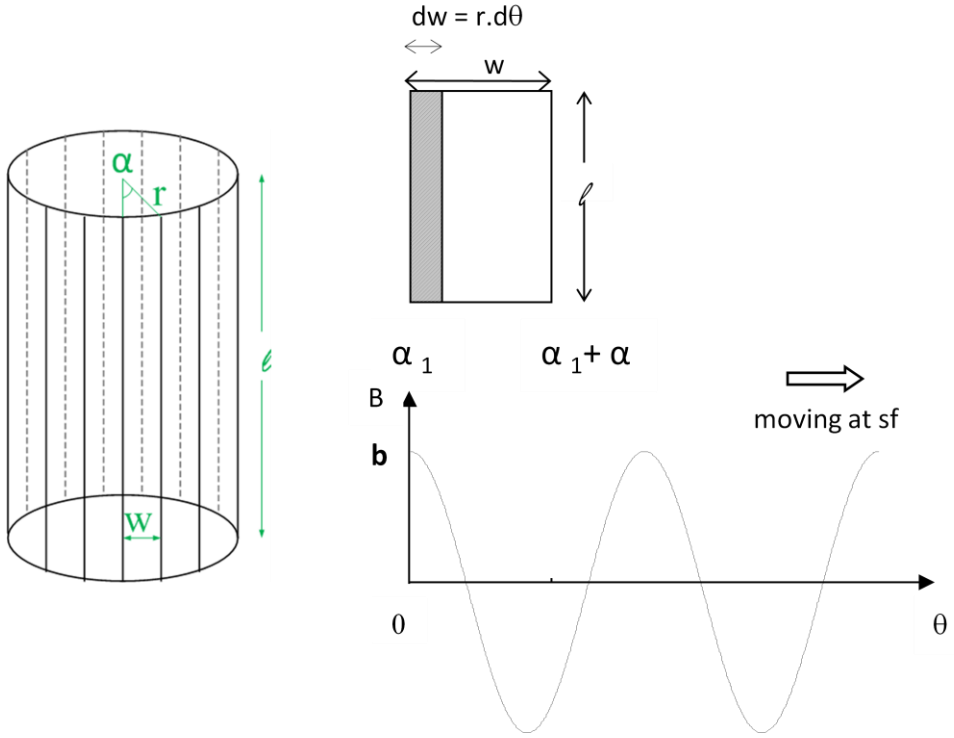

(a) (b)

Figure 5.1 Rotating field inducing emf in a rotor mesh. a) rotor cage schematic, b) rotating field moving at sf with respect to one rotor mesh.

The flux linking any rotor mesh with the width of w covering mechanical angle α, is:

$$\emptyset(t) = \int B.dA = \int_{\alpha 1}^{\alpha 2} b\, cos(p\theta - 2\pi sft)\; l\, r d\theta \tag{5.2}$$

$$\emptyset(t) = \frac{blr}{p}\,[sin(p\alpha_2 - 2\pi sft) - sin(p\alpha_1 - 2\pi sft)] \tag{5.3}$$

Using the trigonometric identity of (5.4), equation (5.3) can be simplified into (5.5).

$$sin\, u - sin\, v = 2\, cos\frac{u+v}{2} sin\frac{u-v}{2} \tag{5.4}$$

$$\emptyset(t) = \frac{2blr}{p}\; sin\left(\frac{p\alpha}{2}\right)\; cos\;(2\pi sft - \frac{p\alpha_m}{2}) \tag{5.5}$$

where, A is the area of the mesh, l is the length of the rotor, $\alpha_2 = \alpha_1+\alpha$, $\alpha_m = (\alpha_1 + \alpha_2)/2$, and r is the rotor radius.

The emf induced in this rotor circuit is the time derivative of the flux linking it.

$$E_r(t) = -\frac{d}{dt}\emptyset(t) \tag{5.6}$$

$$E_r(t) = \frac{4\pi f b l r}{p}\, s\ \ sin\left(\frac{p\propto}{2}\right) sin(2\pi s f t - p\alpha_m) \tag{5.7}$$

Since b which is the air gap field magnitude is proportional to the stator current amplitude, it can be replaced by $k_i\,|I|$. Then, the emf induced in the rotor mesh would be

$$E_r(t) = k_1\,|I|s\ \ sin\left(\frac{p\propto}{2}\right) sin(2\pi s f t - p\alpha_m) \tag{5.8}$$

where, $k_1 = 4k_i\pi flr/p$ is a constant. Therefore, for a given current, the emf induced in each mesh is a function of slip and the mesh angle α.

In the case of n contiguous defected bars, the faulted mesh angle will increase to $\alpha_n=(1+n)\alpha$. As n increases, the rotor becomes less magnetized which causes the slip to increase to s_n. Because of the asymmetry in the defected rotor, the induced current in the faulted mesh is different from the other healthy meshes. The anomalous currents induced in the rotor circuits result in an effective unbalanced three-phase magnetic field at slip frequency which gives rise to two counter rotating fields at ± sf with respect to rotor. With n contiguous broken bars, the amplitude of the current induced in the faulted mesh is the emf divided by the resistance of the mesh.

$$I_{r,n} = \frac{E_{r,n}}{R_{r,n}} = \frac{k_1}{R_{r,n}}\,|I|\,s_n\ \sin\frac{p\alpha_n}{2}\ \ sin\left(2\pi s_n f t - p\alpha_{mf}\right) \tag{5.9}$$

where, $I_{r,n}$, $E_{r,n}$, $R_{r,n}$ are the current, emf and resistance corresponding to the faulted mesh enclosing n broken bars. s_n is the slip with n broken bas, α_n is the angle of the faulted

mesh and α_{mf} is the midpoint of the faulted mesh. Assuming the bars and end rings have the same resistance per unit length, $R_{r,n}$ will be proportional to the perimeter of the mesh.

$$R_{r,n} = \frac{\rho \ pr}{A_b} \tag{5.10}$$

where, ρ is the resistivity, A_b is the bar cross sectional area and pr is the perimeter of the mesh.

$$I_{r,n} = k_1 \frac{A_b}{\rho} |I| \frac{S_n}{pr} \sin\frac{p(1+n)\alpha}{2} \sin\left(2\pi s_n f t - p\alpha_{mf}\right) \tag{5.11}$$

and, the perimeter of the mesh is:

$$pr = 2\,(l + w_n) \tag{5.12}$$

5.3.2 Field Components Produced by the Rotor Mesh Currents

The sinusoidal current induced in each mesh will produce a sinusoidal field component in the air gap which can be represented by a vector rotating at sf. The magnitude of each field vector is proportional to magnitude of the current in (5.11) and oriented toward the center of the mesh. The magnitude of the field component generated by each mesh can be approximated as the field at the center of a current carrying circular loop which is given by:

$$B_{r,k} = \frac{\mu_o I_{r,n}}{r_{mesh}} \tag{5.13}$$

where, μ_o is the permeability of free space and r_{mesh} is the effective radius of the mesh if it was a circle. It can be approximated as:

$$r_{mesh} = \frac{1}{2}(l + w_n) \tag{5.14}$$

Therefore, the size of the mesh has a squared effect in reducing the field component produced by that mesh. Now, the field component produced by the faulted mesh current is:

$$B_{r,n} = k_1 \frac{\mu_o}{r_{mesh}} \frac{A_b}{\rho} |I| \frac{S_n}{pr} \sin\frac{p(1+n)\alpha}{2} \sin\left(2\pi s_n f t - p\alpha_{mf}\right)$$

$$= k |I| \frac{S_n}{(l+w_n)^2} \sin\frac{p(1+n)\alpha}{2} \sin\left(2\pi s_n f t - p\alpha_{mf}\right) \quad (5.15)$$

where, $k = k_1 \frac{\mu_o A_b}{\rho}$.

If the ratio of the length to the width of a healthy mesh is c= ℓ / w, then

$$l + w_n = cw + (1+n)w = (1+c+n)r\alpha \quad (5.16)$$

Then the field equation can be rewritten in terms of the number of broken bars n.

$$B_{r,n} = k |I| \frac{S_n}{((1+c+n)r\alpha)^2} \sin\frac{p(1+n)\alpha}{2} \sin\left(2\pi s_n f t - p\alpha_{mf}\right) \quad (5.17)$$

The field contribution of a healthy mesh can be obtained by setting n=0 in (5.17).

5.3.3 Field Vectors Arrangement

A symmetric N-bar rotor cage is, in essence, an N-phase balanced circuit, phase shifted by α=2π/N in space, each one carrying a sinusoidal current phase shifted by α. In this case, the resulting rotating field produced by rotor currents has a constant magnitude. In the event of any rotor asymmetry, however, the magnitude of the rotating field does not remain constant and starts oscillating. This rotating field with an oscillatory magnitude can be represented by the superposition of a forward rotating field with a constant magnitude and a backward rotating field with another constant

magnitude. The key point here is to correlate the magnitude of the backward rotating field which is related to the fault signature, with the number of defective phases.

The field components produced by a symmetric cage rotor can be represented by *N* balanced vectors as:

$$B_h = \ k\ |I|\ \frac{s}{((1+c)r\alpha\,)^2} sin\frac{p\alpha}{2} \angle -(h-1)\alpha \qquad , for\ h=1, 2, 3, \ldots N \tag{5.18}$$

In the event of *n* contiguous rotor failures in locations n_1 to n_1+n-1, the field vectors corresponding to the healthy meshes remain unchanged and the *n+1* vectors related to the *n* broken bars are replaced with a new fault vector B_f. In this case slip will increase to s_n due to the defective rotor, and the *N-n* field vectors will be:

$$\begin{cases} B_h = k\,|I|\ \frac{s_n}{((1+c)r\alpha\,)^2}\ \ sin\frac{p\alpha}{2}\angle -(h-1)\alpha \quad , for\ h < n_1 - 1\ or,\ h \geq\ n_1\ + n \\ B_f = k\ \ |I|\frac{s_n}{((1+c+n)r\alpha\,)^2}\ \ sin\frac{p(1+n)\alpha}{2}\angle -(n_1 - 1 + \frac{n}{2})\alpha \end{cases} \tag{5.19}$$

where, B_h is the field vector produced by the h^{th} healthy mesh, B_f is the single fault vector produced by the faulted mesh, n is the number of broken bars, n_1 is the index of the first broken bar, and $\alpha = 2\pi/N$. The fault vector B_f is substituted for the n+1 contiguous field vectors corresponding to the n broken bars. For simplicity, these vectors can be normalized with respect to the healthy field vector amplitude.

$$\begin{cases} B_h = 1\ \angle -(h-1)\alpha \qquad\qquad , for\ h < n_1 - 1\ or,\ h \geq\ n_1\ + n \\ B_f = \frac{(1+c)^2}{(1+c+n)^2}\ \ \frac{sin\,(\frac{p(1+n)\alpha}{2})}{sin\left(p\frac{\alpha}{2}\right)}\ \angle -(n_1 - 1 + \frac{n}{2})\alpha \end{cases} \tag{5.20}$$

The magnitude of the fault vector comprises two terms. The first term is the squared ratio of a healthy loop perimeter to the faulted loop perimeter, and the second term is the sine ratio of the faulted mesh electrical angle to a healthy mesh electrical angle. If

$$K(n) = \frac{c+1}{c+n+1} \quad , c = l / w \tag{5.21}$$

and,

$$A_n = \frac{sin\,(p(1+n)\alpha/2}{sin\,(p\frac{\alpha}{2})} \tag{5.22}$$

Then the field vectors can be simplified in the final form of:

$$\begin{cases} B_h = 1 \angle \emptyset_h & , \emptyset_h = -(h-1)\alpha \\ B_f = K(n)^2\, A(n) \angle \emptyset_f & , \emptyset_f = -(n_1 - 1 + \frac{n}{2})\alpha \end{cases} \tag{5.23}$$

Therefore, the normalized healthy field vectors having unity amplitudes are phase shifted by α with respect to each other. The fault vector, which is substituted for the field vectors corresponding to the n broken bars, has the magnitude of $K(n)^2\, A(n)$ and directed to the middle of the faulted mesh. It should be noted that only the fault vector is affected by the number of broken bars.

The rotating field at each instant of time is determined by the vector sum of the *N-n* individual field vectors defined by (5.23) as follows.

$$B_{rot.}(t) = B_f\, e^{j\ \emptyset_f} + \sum_{all\ h} B_h\, e^{j\ \emptyset_h} \tag{5.24}$$

It is worth mentioning that B_f and B_h are the sinusoidal function of time, all having frequency sf.

As an example, the field vector representation of an 8-bar cage with one broken bar is shown in Fig. 5.2. It should be noticed that each field vector shown in the figure is located between the two neighboring bars. For example B1, which is the field component produced by the current in the mesh of bar 8 and bar 1, is located between bar 8 and bar1. There are six healthy vectors having unity amplitudes, phase shifted by

$\alpha = \pi/4$, and the two vectors surrounding the broken bar #6, are replaced by the fault vector B_f. Assuming c=15 and p=2, and using (5.23) the fault vector amplitude will be $A(2)\ K(2)^2 = \frac{\sin(2\alpha)}{\sin(\alpha)}\ (\frac{C+1}{C+2})^2 = 1.24$, and the fault phase angle is $\phi_f = -11\pi/8$.

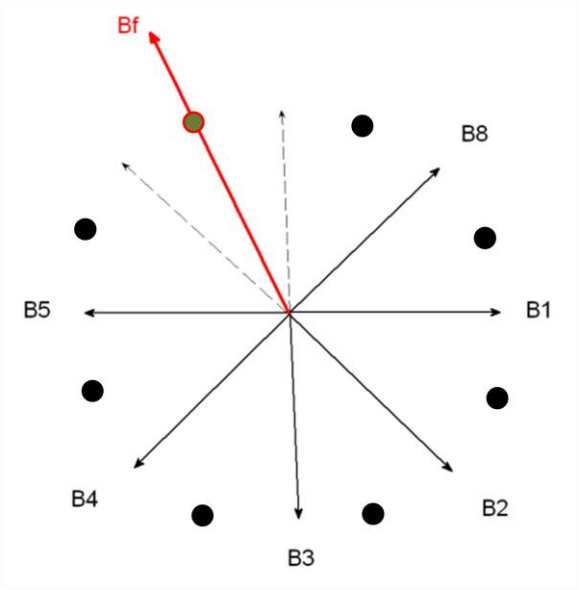

Figure 5.2 Field vector representation produced by an 8-bar cage with one broken bar.

The sinusoidal representation of the field components in this example is shown in Fig. 5.3, with the amplitudes normalized with respect to the amplitude of the healthy field components. The resultant rotating field obtained from the vector sum in (5.24) is also presented in this figure. The oscillatory amplitude of the rotating field is due to the rotor asymmetry which produces two counter rotating fields at sf and -sf, with constant amplitudes.

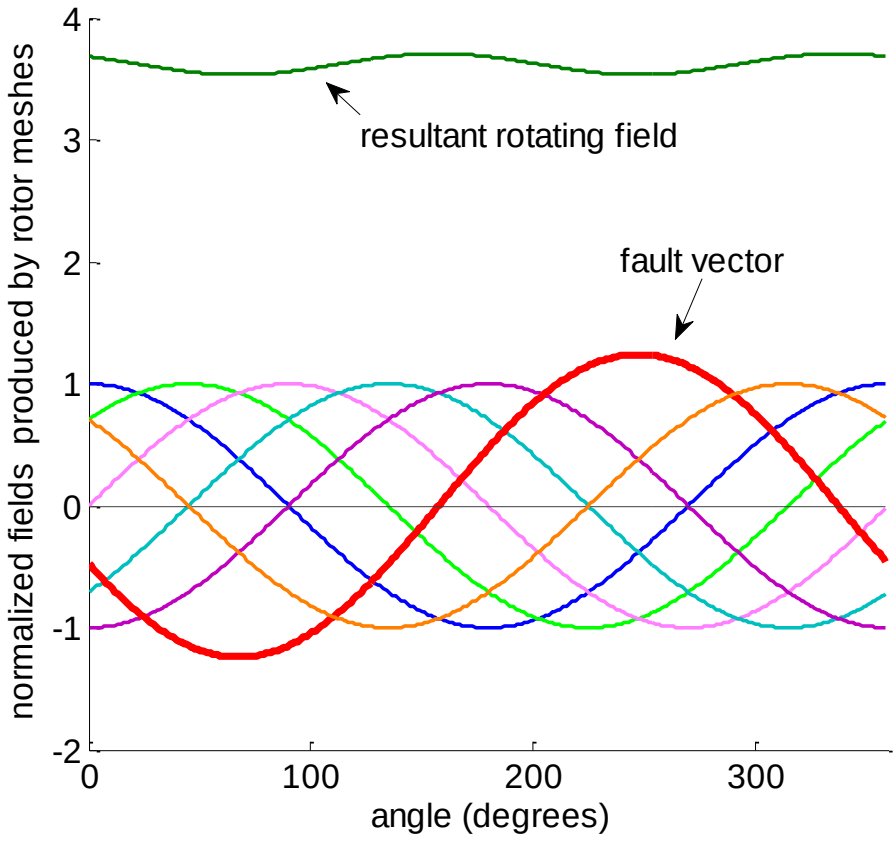

Figure 5.3 Field components generated by the healthy and faulty meshes and the resultant rotating field.

The two counter rotating field components are presented in Fig. 5.4. If the amplitude of the positive rotating field is denoted by B_p and for the negative one is B_n then during one revolution there will two points that theses two vectors meet, causing the total amplitude of the rotating field to be B_p+B_n . There are two other incidents that these vectors are directed against each other, leading to the resulting amplitude of B_p-B_n. Therefore, the maximum amplitude of the rotating field, B_{max}, is the sum of B_p and B_n

and the minimum amplitude, B_{min}, is the difference between B_p and B_n. Then assuming $B_p > B_n$, the positive and negative rotation field amplitudes can be easily obtained by:

$$B_p = \frac{B_{max}+B_{min}}{2} \tag{5.25}$$

$$B_n = \frac{B_{max}-B_{min}}{2} \tag{5.26}$$

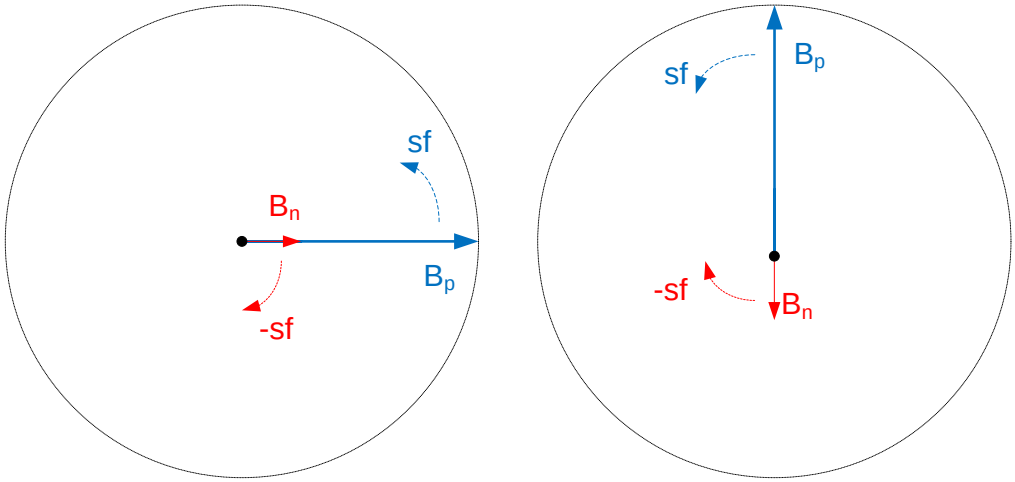

Figure 5.4 Two counter rotating fields. (left) in the same direction creating B_{max}, (right) in opposite directions creating B_{min}.

5.3.4 Stator Current Component Generated by the Backward Rotating Field

In order to find the effect of the negative rotating field component on the stator current, let's assume this component to be the only field in the air gap. The backward rotating field component, having the magnitude of B_n, rotates at $-s_nf$ with respect to rotor and $(1-2s_n)f$ with respect to the stator. Now consider this field moving against the stator

winding with the constant width of a pole pitch at rotational speed of (1-2s_n)f as shown in Fig. 5.5. The field can be expressed as:

$$B'(\theta, t) = B_n \cos(p\theta - 2\pi(1 - 2s_n)ft) \quad (5.27)$$

where, p is the number of pole pairs, θ is the mechanical angle, s_n is the rotor slip at faulty condition, f is the excitation frequency and n is the number of broken bars. The flux linking a full pitch stator winding with the angular width of π/p can be written as:

$$\emptyset'(t) = \int B' \, dA' = \int_0^{\pi/p} B_n \cos(p\theta - 2\pi(1 - 2s_n)ft) \, l \, r_s d\theta \quad (5.28)$$

$$\emptyset'(t) = \frac{2B_n l r_s}{p} \sin(2\pi(1 - 2s_n)ft) \quad (5.29)$$

where, A' is the area of the winding and r_s is the stator radius.

The emf induced in stator winding circuit can be derived by differentiating the flux linking it.

$$E_s(t) = -\frac{d}{dt}\emptyset'(t) \quad (5.30)$$

$$E_s(t) = -\frac{4}{p} l r_s \pi f B_n (1 - 2s_n) \cos(2\pi(1 - 2s_n)ft) \quad (5.31)$$

The component of the stator current produced by the negative rotating field, known as the LSBC, can be obtained by dividing the emf in (5.31) by the stator winding resistance R_s.

$$I_{s,n}(t) = \frac{E_s(t)}{R_s} = K_s B_n (1 - 2s_n) \cos(2\pi(1 - 2s_n)ft) \quad (5.32)$$

where, $K_s = \frac{4}{p R_s} l r_s \pi f$ (constant).

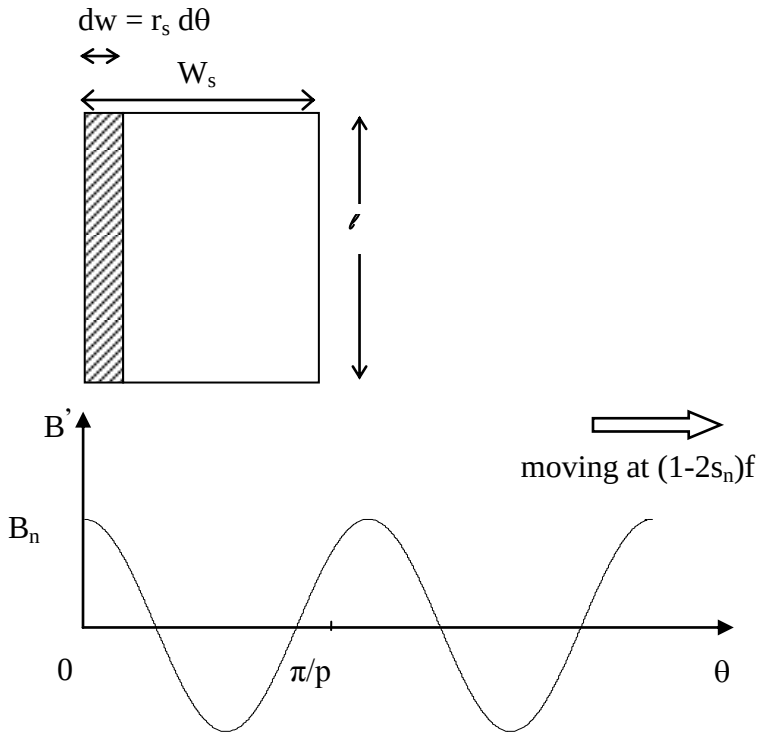

Figure 5.5 Fault related field component moving at $(1\text{-}2s_n')f$ with respect to the full pitched stator winding.

The equation of the left sideband component of the stator current given by (5.32) indicates that the magnitude of this component is a function of $(1\text{-}2s_n)$ and B_n, which itself is a function of slip and n. Since B_n was found by normalizing the field vectors with respect to the healthy field vector magnitude in (5.20), the actual magnitude of the LSBC as a function of the number of the broken bars, n, is:

$$|LSBC| = K_s \; k \; |I| \frac{s_n}{((1+c)r\alpha)^2} \; sin\frac{p\alpha}{2} \; (1-2s_n) \; B_n \tag{5.33}$$

Therefore, the actual magnitude of the left side band component of the stator current can be simplified in the final form of:

$$|LSBC| = K_t \; s_n \; (1-2s_n) \; B_n \; |I| \tag{5.34}$$

where, $K_t = \frac{K_s.k}{((1+c)r\alpha)^2} \ sin\frac{p\alpha}{2}$

The amplitude of the LSBC can be normalized with respect to the amplitude of the stator current as follows.

$$\frac{|LSBC|}{|I|} = K_t.\ s_n\ (1-2s_n)\ B_n \tag{5.35}$$

$$\frac{|LSBC|}{|I|} \propto \ s_n\ (1-2s_n)\ B_n \tag{5.36}$$

The constant K_t is determined by the machine parameters. The normalized amplitude of the LSBC is a non-linear function of the rotor slip. It is also a function of the negative rotating field amplitude, B_n, which is a non-linear function of the number of broken bars, n.

5.4 Analytical and Simulation Results Applied to the Broken Rotor Bars in Induction Machines

The normalized field component produced by the faulted mesh, as the number of the contiguous broken bars increases, is given by (5.23). This is the fault vector magnitude normalized with respect to the healthy vectors and is the product of A(n) and $K^2(n)$. Fig. 5.6 shows the variations of A(n), $K^2(n)$ and the fault vector B_f which is the product of the two functions, for a 4-pole, 36-bar induction motor. A(n) is the normalized emf induced in the faulted mesh enclosing n broken bars, and K(n) is the inverse of the normalized perimeter of the faulted mesh. It can be observed that the maximum emf is induced in the mesh when there are 8 broken bars. This is when the width of the faulted mesh is 9α or one pole pitch. As the number of broken bars

increases above *N/2p – 1=8*, the flux linking the mesh is reduced due to the negative half cycle of the air gap field, leading to less emf induced in the mesh. Due to the effect of K(n), which is related to the faulted mesh size, the maximum amplitude of the fault vector is shifted back at n< *N/2p – 1*. The amount of the shift depends on the constant c, which is the ratio of the length to the width of a healthy mesh.

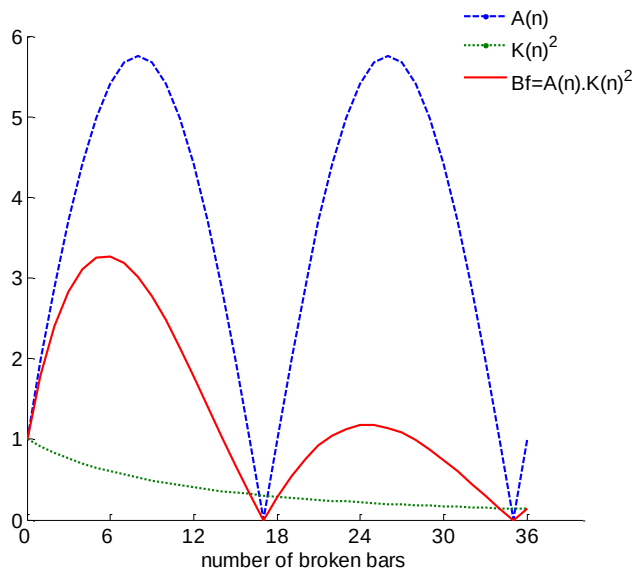

Figure 5.6 Variation of the field component generated by the faulted mesh with n broken bars. (for a 4-pole 36 bar cage and c= ℓ / w =20)

A program has been developed to calculate the normalized healthy and faulty vectors as the number of contiguous broken bars increases using (5.23). After the field vectors are arranged, the sum of all vectors at each instant of time is calculated as given by (5.24). The vector sum over one revolution gives the air gap rotating field which has forward and backward components in the case of rotor asymmetry. Then the positive

and negative rotating field amplitudes are obtained from the maximum and minimum value of the rotating field using (5.25) and (5.26).

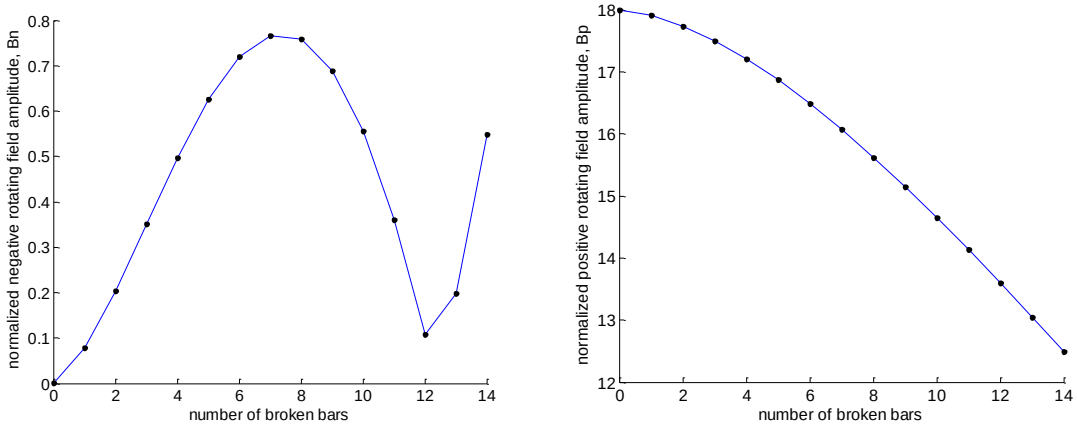

Figure 5.7 Normalized magnitudes of the rotating field components. (left) backward rotating field, (right) forward rotating field.

When the normalized negative rotating field magnitude B_n is found, the normalized LSBC can be correlated to the number of the broken bars by multiplying B_n by $s_n(1\text{-}2\ s_n)$. For the rotor slip, s_n, under different fault conditions, the simulation slip values are used.

Using the analytical method explained in this section, the normalized negative and positive rotating field amplitudes are obtained and presented in Fig. 5.7 for a 4-pole 36 bar induction motor and for 0 to14 broken bars. Using (5.36) and the slip values from simulation under lightly loaded condition, the normalized amplitude of the left side band component of the stator current is calculated and shown in Fig. 5.8.

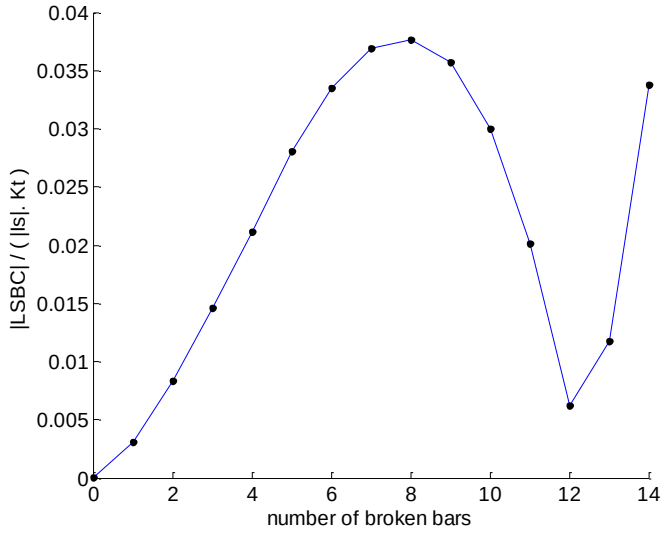

Figure 5.8 Normalized LSBC amplitude with respect to the motor constant K_t and the stator current amplitude. ($|LSBC| / (|I| K_t)$)

Intuitively speaking, the positive rotating field B_p is related to the rotor magnetization which in turn is related to the slip. A higher B_p leads to higher magnetized motor and as a result a lower slip. Therefore, it is expected that the rotor slip is inversely related to the positive rotating field magnitude.

The synchronous machine model explained in section 2 was modified to model an induction motor. The field winding was removed and four extra bars per pole were added in the gaps of the damper winding to make it a symmetrical cage with 36 bars. All the parameters remained the same as original values. Different conditions of healthy and 1 to 14 broken bars were simulated under 10% load. The magnitude of the normalized left side band components with respect to the fundamental frequency were recorded and plotted in Fig. 5.9.

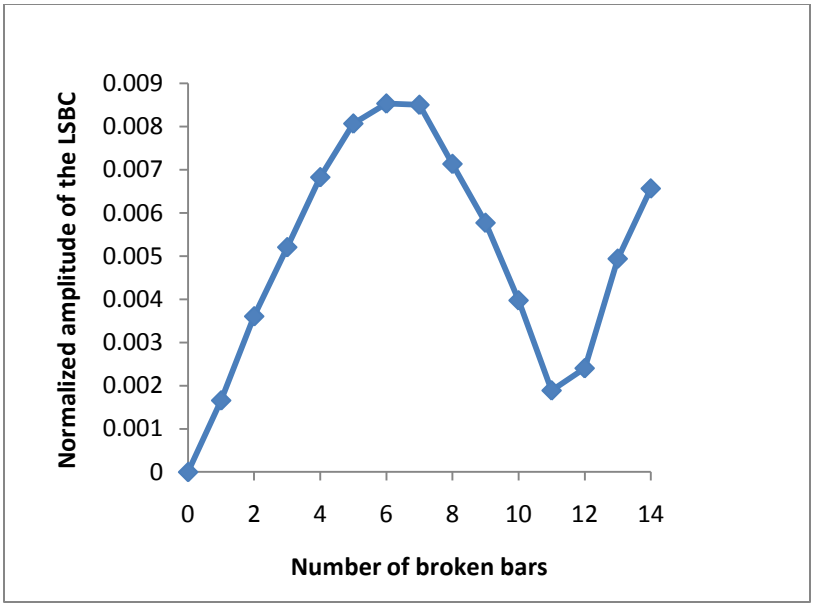

Figure 5.9 Simulation results of the normalized LSBC amplitude with respect to the stator current. (|LSBC| / |I|)

It should be noticed that the analytical plot and the simulation plot have similar patterns. The difference in amplitudes is due to the motor constant K_t which was automatically included in the simulation results.

5.5 Analytical and Simulation Results Applied to the Broken Damper Bars in Synchronous Machines

The field arrangement method can also be applied to a synchronous motor with damper winding when it is running with no field excitation. It will help to predict the pattern of the LSBC amplitude variation with the number of broken bars. The correlation between the LSBC and n is more complicated in the case of a synchronous

motor. The reason is that a healthy damper winding has already some missing bars between the poles which generate the left side band component. Fig. 5.10 shows the field vector arrangement for the healthy and one broken bar damper winding.

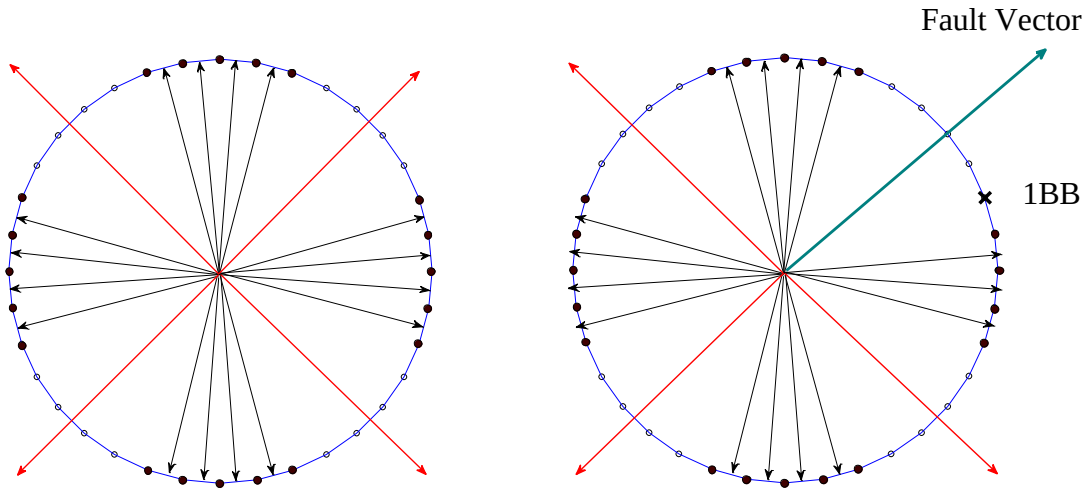

Figure 5.10 Field vectors arrangement for (left) healthy damper winding and (right) one broken damper bar.

In the healthy damper winding, there are 16 healthy and 4 fault vectors. When one bar is failed, the number of healthy vectors reduces to 15, and one of the fault vectors is changed in amplitude and phase shifted by $\alpha/2$. The fault vector amplitude may increase or decrease depending on the width of the mesh created after the bar breakage. In this case the width of the mesh after one bar failure will be 6α which is similar to the mesh with 5 broken bars. The fault vector amplitude can be found from (5.23) at n=5.

The negative rotating field B_n is a measure of asymmetry and is dependent on the number of vectors, fault vector amplitude, and fault vector phase angle. Therefore, the LSBC, which is a function of B_n and slip, is not easily predictable.

The analytical results of the per unit LSBC amplitudes versus n, using the slip values of 15% load conditions, is presented in Fig. 5.11. The variation pattern is similar to the simulation and experimental results of Fig. 4.11.

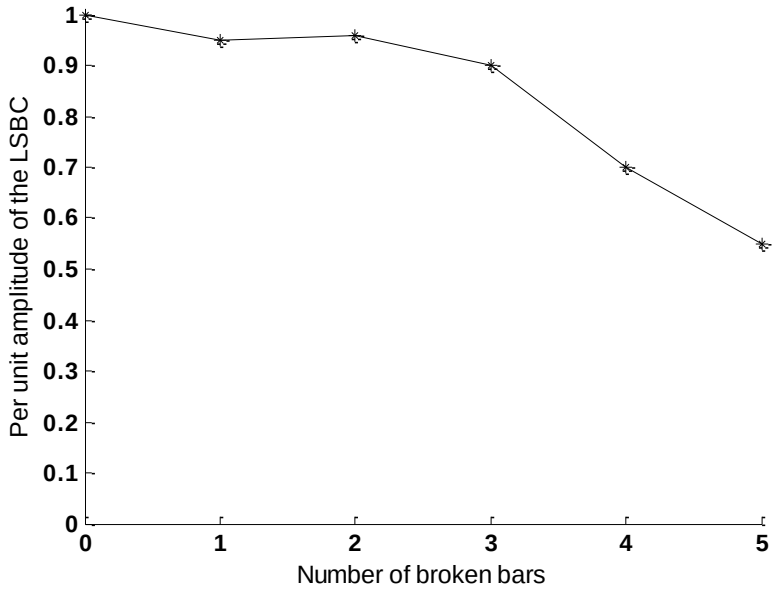

Figure 5.11 Per-unit amplitude of the LSBC for healthy and 1 to 5 broken damper bars.

5.6 Conclusions

In this section an analytical approach for correlating the LSBC amplitude with the number of broken bars was developed. This method was based on the rotating field theory and unbalanced multi-phase systems. It can be applied to the cage rotor induction

machines as well as the synchronous machines with damper windings. It was found that for an induction machine, the LSBC amplitude increases with n, if n is small. For a synchronous motor, a damper bar failure may cause increasing or decreasing of the LSBC. It depends on the damper winding geometry, the location of the broken bars, and the rotor slip.

6. CONCLUSIONS AND FUTURE WORK

In this section, a summary of the research work discussed in earlier sections is presented. This dissertation was mainly concerned with developing a diagnosis technique for the damper winding failure of the synchronous machines. Since there is very limited research on this subject, this research focused on the effects of damper winding failure on the motor current spectrum at steady state and transient conditions. It also investigated the effects of the broken damper bars on the speed spectrum, transient time, torque-speed curve and rotor slip.

6.1 Summary and Conclusions of the Research

Intensive research efforts have been aimed at detecting mechanical and electrical failures in induction machines, including rotor bar failure. However, there are very limited research publications on diagnosis of damper winding failures in synchronous machines. In these few studies, flux probes were attached to the stator bore surface for measurement of the air gap flux waveforms at startup. This method of fault diagnosis is intrusive and is not preferred because it requires opening the machine and installing sensors inside it. The motor current signature analysis (MCSA) is the most popular non-intrusive diagnosis method because the motor current can be easily accessed. The main research objective of the work reported in this dissertation was to find a signature in synchronous machines from non-intrusive measurements indicating the existence of failures in damper windings.

In section 1, a brief overview of common failures of induction motors and synchronous motors, their causes, and detection techniques was presented.

In section 2, a method was introduced for modeling synchronous machines with damper windings using the winding function approach. In this model, the actual winding distribution was used, which does not require neglecting the harmonics of the stator winding distribution. The proposed model can be used to simulate the machine under different fault conditions such as broken damper bars and end rings, eccentricities and inter-turn faults. All machine inductances were calculated as a function of the rotor position using the winding function method, based on the geometry of the machine and its winding configuration. A simple method of modeling the skewed rotor was also presented which improved the accuracy of the waveforms. A damper winding with n bars and two end rings was modeled as a network with $(n+1)$ independent meshes, each treated as a short pitched single turn winding. There were three sets of electromagnetic circuits mutually coupled together: armature windings, field winding and damper winding. The electromagnetic torque equation was derived, and the machine differential equations were given which are solved using Matlab. This model was capable of predicting the machine behavior during transients and steady state operations. The simulated machine waveforms were presented for the cases during startup, during excitation of the field winding, and during connection of the load.

In section 3, studies were discussed using the proposed model of synchronous machines, to study the effect of damper winding failures on the motor current spectrum during steady state and transient conditions. When the motor was running at

synchronous speed, there was no current induced in the damper winding, and it had no effect on the motor operations. Therefore, a failed damper winding was not expected to affect the machine waveforms during steady state synchronous operation. For diagnosis purposes, the waveforms during (1) startup transient, (2) field excitation transient, (3) load change transient, and (4) asynchronous steady state operation with open field winding were examined. For spectral analysis of the stator current, Short Time Fourier Transform (STFT) analysis was employed during transient, and Fast Fourier Transform (FFT) analysis was used during steady state operations.

The spectral components found during transients agree with the expected theoretical components. However, the transient analysis did not provide a feature for identification of the rotor condition. In asynchronous steady state condition, the left side band component (LSBC) was found to be present in all healthy and faulty cases of damper windings, and the amplitude variation of the spectral components in relation to the number of broken damper bars did not have a clear correlation. However, the transient time and rotor slip were directly correlated with the fault severity. The speed spectral component at 2sf was also present in the healthy and faulty cases.

The effect of damper bar failures on the torque speed curve was studied for different fault severities. The torque speed curves were calculated when operating with open field, like an induction motor. At 50% speed, corresponding to $s = 0.5$, the magnitude of the fault related current component of $(1-2s)f$ was zero. Zero magnitude of this component pulls down the torque and creates a notch at half speed.

Experimental results were presented in section 4. To measure and analyze the signals of a synchronous machine with a failed damper winding, a special inside-out synchronous machine (IOSM) was built. The armature windings of the IOSM were wound on the round rotor, connected to the supply via slip rings, and its field winding was mounted in some of the stator slots. The copper bars of the damper cage were placed in the remaining stator slots aligned with the pole faces. The experimental setup consists of the IOSM, a 3-phase transformer, hysteresis breaks, torque meter, shaft encoder and data acquisition card connected to a computer.

The experimental results of several tests with different damper fault conditions confirmed that, even with a healthy damper winding, the left side band component of the motor current exists. Therefore, as opposed to the case of an induction machine rotor bar failure, this component cannot be used as a fault signature. The variation of the LSBC component does not convey a specific trend. The rotor slip, however, shows an upward trend as the number of broken damper bars increases.

Since the presence of the LSBC did not necessarily indicate a failure, to detect a damper winding fault and its severity from the motor current spectrum, some knowledge about the left side band component amplitude was needed at healthy and faulty damper conditions. It was important to find a correlation of LSBC amplitude with the health condition of the damper winding. A novel analytical method was proposed in section 5, to correlate the left side band component of the stator current amplitude with the number of broken bars. This method can be applied to the cage induction motors as well as to synchronous motors with damper windings. It is based on fundamental electromagnetic

field theory and the characteristics of multi-phase unbalanced circuits. The method presented details on how the LSBC was generated when there was an asymmetry in the rotor structure. It was shown that the LSBC magnitude was a nonlinear function of the rotor slip and also a function of the negative rotating field amplitude; both are affected by the number of broken bars. In order to find the negative rotating field magnitude, the total rotating field was calculated by sum of all field vectors. Each field vector represented a sinusoidal magnetic field produced by the corresponding rotor mesh. When *n* contiguous bars were broken, a larger mesh was formed, producing a different field vector component called fault vector. The magnitude and phase of the fault vector produced by the faulted mesh was derived in terms of the number of broken bars and the machine parameters.

When there was a rotor asymmetry, the field vectors did not represent a balanced sinusoidal set of fields. In this case, the magnitude of the air gap rotating field fluctuates due to the backward and forward rotating field components, which were added or subtracted at different points in a revolution. The negative and positive rotating field components were found from the maximum and minimum values of the oscillatory magnitude of the air gap rotating field.

The analytical results of the LSBC variation with various fault severity were presented for a broken bar in induction motor as well as a broken damper bar in synchronous motor. The field vector arrangement seemed to be a powerful method for deriving the air gap rotating field and the resulting LSBC in various fault cases of cage rotor induction machines and synchronous machines with a damper winding. Since the

LSBC was not a damper fault indicator by itself, prior knowledge of its magnitude at different fault conditions provided some information of the motor health.

The non-intrusive method of motor current signature analysis is not sufficient for damper winding fault detection. However, combining the motor current spectrum information with prior analysis of the expected LSBC amplitude under different health conditions, made the fault diagnosis possible in a non-intrusive way. The LSBC amplitude for each fault condition can be determined using either the model proposed in section 2, or the analytical approach presented in section 5.

Because of the asymmetrical structure of damper winding, the left sideband component in the stator current spectrum of synchronous machine during steady state asynchronous operation is not similar to that of the induction machine with broken bars. As a result, the motor current signature analysis (MCSA) for detection rotor failures in induction machine was not able to be used to detect broken damper bars in synchronous machines. However, a novel intelligent-systems based approach was developed that can identify the severity of the damper winding failure. This approach potentially could be used in a non-invasive condition monitoring system to monitor the deterioration of a synchronous motor damper winding as the number of broken bars increase over time.

6.2 Future Work

There are many other issues related to this study that can be investigated in the future to be a welcome addition to this research work.

In this research, a damper winding with continuous end rings was studied, while for large high speed synchronous machines interrupted end rings are often used. The proposed model can be used to simulate different damper winding failures when interrupted end rings are used. The field vectors arrangement approach can be applied to the case of damper winding with interrupted end rings in order to find the magnitude of the LSBC and its correlation with the number of broken bars.

While it is more likely that when one bar is broken, the fault propagates through the adjacent bars, it is also possible that the fault occurs in separate locations. The non-contiguous broken damper bars can also be investigated in the future.

The location of the broken bar will affect the current induced in the faulted mesh and therefore, will affect the LSBC amplitude. For the same number of broken bars, the effects of the fault location can be studied.

Besides the bar failures in damper windings, the end rings can also fail. This type of failure can be studied with both cases of continuous and interrupted end rings. The field vectors arrangement approach can be used to predict the LSBC amplitude in different cases of end ring faults.

The positive rotating field amplitude, which can be found by the field vectors arrangement approach, seems to be correlated with the rotor slip when a damper winding fails. This correlation can be investigated for damper winding failures in synchronous machines and cage rotor failures in induction machines. If this correlation is determined the rotor slip variations with the number of broken bars can be found. Then, the rotor slip which is needed for the LSBC amplitude calculation can be directly obtained from

the positive rotating field within the field vector arrangement approach, without the need of simulated slip values.

A possible diagnostic method for detecting the damper failures, by performing standstill tests can also be examined. The diagnosis might be possible by means of a special kind of signal injected to the stator terminals. The excitation should be large enough to drive a significant current in the stator windings without starting the machine. The axial flux produced by the injected signal can be measured using an external search to detect any asymmetry in the damper winding. This method has been applied for diagnosis of induction machines rotor faults [60].

REFERENCES

[1] P. Vas, *Parameter Estimation, Condition Monitoring, and Diagnosis of Electrical Machines*, Oxford, U.K. Clarendon, 1993.

[2] G. B. Kliman, and J. Stein, "Induction motor fault detection via passive current monitoring," in *Proc. Int. Conf. Electrical Machines*, Cambridge, MA, pp. 13–17, 1990.

[3] S. Nandi, H. A. Toliyat, and X. Li, "Condition monitoring and fault diagnosis of electrical motors: A review," *IEEE Trans. Energy Convers*, vol. 20, no. 4, pp. 719–729, 2005.

[4] R. Schoen, T. Habetler, F. Kamran, and R. Bartfield, "Motor bearing damage detection using stator current monitoring," *IEEE Trans. on Industry Applications*, vol. 31, no. 6, pp. 1274–1279, 1995.

[5] Austin Bonnett, and Chuck Young, "Surveys can't answer all of your motor failure questions, but a thorough root cause analysis can help fill in the gaps," *Electrical Construction & Maintenance (EC&M) magazine*, Oct. 2004.

[6] B. Yazici, and G. B. Kliman, "An adaptive statistical time-frequency method for detection of broken bars and bearing faults in motors using stator current," *IEEE Trans. on Industry Applications*, vol. 35, no. 2, pp. 442-452, 1999.

[7] W. Zhou, T. G. Habetler, and R.G. Harley, "Incipient bearing fault detection via motor stator current noise cancellation using Wiener Filter," *IEEE Trans. on Industry Applications*, vol. 45, pp. 1309-1317, 2009.

[8] H. Ocak, "Fault detection, diagnosis and prognosis of rolling element bearings: frequency domain methods and hidden markov modeling," Ph.D. Dissertation, School of Electrical Engineering, Case Western Reserve University, Cleveland, Ohio 2004.

[9] L. Eren, "Bearing damage detection via wavelet package decomposition of stator current," Ph.D. Dissertation, School of Electrical Engineering, University of Missouri-Columbia, Columbia, Missouri, 2002.

[10] J. R. Stack, R. G. Harley, and T. G. Habetler, "An amplitude modulation detector for fault diagnosis in rolling element bearings," *IEEE Trans. on Industrial Electronics*, vol. 51, no. 5, pp 1097-1102, 2005.

[11] J. Douglas, "Hydro generator failure," *IEEE Power Engineering Review*, vol. 8, no. 11, pp. 4-6, 1988.

[12] G. Stone, and J. Kapler, "Stator winding monitoring," *IEEE Industry Applications Magazine*, vol. 4, pp 15-20, 1998.

[13] A. Siddique, and G. S. Yadava, B. Singh, "A review of stator fault monitoring techniques of induction motors," *IEEE Trans. On Energy Conversion*, vol. 20, pp. 106-114, 2005.

[14] S. Nandi, M. Bharadwaj, and H. A. Toliyat, "Performance analysis of a three phase induction motor under mixed eccentricity condition," *IEEE Transactions on Energy Conversion*, vol. 17, pp. 392-399, 2002.

[15] D. G. Dorrell, W. T. Thomson, and S. Roach, "Analysis of air gap flux, current, vibration signals as a function of the combination of static and dynamic air gap

eccentricity in 3-phase induction motors," *IEEE Transactions on Industry Applications*, vol. 33, pp. 24–34, 1997.

[16] M. J. DeBortoli, S. J. Salon, and C.J. Slavic, "Effect of rotor eccentricity and parallel winding on induction machine behavior: A study using finite element analysis," *IEEE Transactions on Magnetics*, vol. 29, no. 2, pp. 1676–1682, 1993.

[17] G. McPherson, and R. D. Laramore, *Electrical Machines and Transformers*, New York, NY, John Wiley, 1990.

[18] P. Neti, and S. Nandi, "Analysis and modeling of a synchronous machine with structural asymmetries," *IEEE-Canadian Conference on Electrical and Computer Engineering*, Ottawa, Canada, pp. 1236-1239, 2006.

[19] P. Neti, and S. Nandi, "Stator inter-turn fault detection of synchronous machines using field current signature analysis," *IEEE-Industry Applications Conference*, Tampa, FL, pp. 1236–1239, 2006.

[20] N. A. Al-Nuaim, and H. A. Toliyat, "A method for dynamic simulation and detection of dynamic air gap eccentricity in synchronous machines", *IEEE International Electric Machines and Drives Conference*, Antalya, Turkey, pp. MA2/5.1- MA2/5.3, 1997.

[21] H. A. Toliyat, and N. A. Al-Nuaim, "Simulation and detection of dynamic air-gap eccentricity in salient-pole synchronous machines," *IEEE Trans. Industry Applications*, vol. 35, pp. 86-93, 1999.

[22] H. C. Kramer, "Broken damper bar detection studies using flux probe measurements and time-stepping finite element analysis for salient pole

synchronous machines," *IEEE International Symposium on Diagnostics for Electric Machines*, Stone Mountain, GA, no. 24-26, pp. 193-197, 2003.

[23] G. B. Kliman, and R. A Koegl, "Noninvasive detection of broken rotor bars in operating induction motors," *IEEE Trans. Energy Conversion*, vol. 3, pp. 873-879, 1988.

[24] S. B. Jovanovski, "Calculation and testing of damper-winding current distribution in a synchronous machine with salient poles," *IEEE Trans. on Power Apparatus and Systems, IEEE Trans. Power Apparatus and System*, vol. 88, no. 11, pp. 1611-1619, 1969.

[25] M. M. Rahimian, and K. Butler-Purry, "Modeling of synchronous machines with damper windings for condition monitoring," *IEEE Electric Machines and Drives Conference*, Miami, FL, pp. 577-584, 2009.

[26] J. P. Bacher, "Detection of broken damper bars of a turbo generator by the field winding," *International Conference on Renewable Energy and Power Quality*, Barcelona, Spain, pp. 35-41, 2004.

[27] J. R. Ruiz, J. A. Rosero, A.G. Espinosa, and L. Romeral, "Detection of demagnetization faults in permanent-magnet synchronous motors under nonstationary conditions," *IEEE Transactions on Magnetics*, vol. 45, pp. 2961-2969, 2009.

[28] A. Khoobroo, and B. Fahimi, "A novel method for permanent magnet demagnetization fault detection and treatment in Permanent magnet synchronous

machines," *IEEE Applied Power Electronics Conference and Exposition*, Orlando, FL, pp. 2231-2237, 2010.

[29] H. A. Toliyat, and N. A. Al-Nuaim, "Simulation and detection of dynamic air-gap eccentricity in salient-pole synchronous machines," *IEEE Transactions on Industry Applications*, vol. 35, no. 1, pp. 86-93, 1999.

[30] B. M. Ebrahimi, J. Faiz, and M. J. Roshtkhari, "Static-, dynamic-, and mixed-eccentricity fault diagnoses in permanent-magnet synchronous motors," *IEEE Transactions on Industrial Electronics*, vol. 56, no. 11, pp. 4727-4739, 2009.

[31] W. le Roux, R. G. Harley, and T. G. Habetler, "Detecting rotor faults in low power permanent magnet synchronous machines," *IEEE Transactions on Power Electronics*, vol. 22, no. 1, pp. 322-328, 2007.

[32] A. Siddique, G. S. Yadava, and B. Singh, "A review of stator fault monitoring techniques of induction motors," *IEEE Trans. On Energy Conversion*, vol. 20, pp. 106-114, 2005.

[33] P. Neti, and S. Nandi, "Stator inter-turn fault analysis of reluctance synchronous motor," *Canadian Conference on Electrical and Computer Engineering*, Saskatchewan, Canada, pp. 1283-1286, 2005.

[34] P. P. Reichmeider, C. A. Gross, D. Querrey, D. Novosel, and S. Salon, "Internal faults in synchronous machines, Part I: The machine model," *IEEE Transactions on Energy Conversion*, vol. 15, no. 4, pp. 376-379, 2000.

[35] B. M. Ebrahimi, and J. Faiz, "Feature Extraction for short circuit fault detection in permanent magnet synchronous motors using stator current monitoring," *IEEE Transactions on Power Electronics*, vol. 25, pp. 2673-2682, 2010.

[36] Tu. Xiaoping, L. -A. Dessaint, M. E. Kahel, and A. O. Barry, "A new model of synchronous machine internal faults based on winding distribution," *IEEE Transactions on Industrial electronics*, vol. 53, no. 6, pp. 1818-1828, 2006.

[37] A. Ali Abdallah, J. Regnier, J. Faucher, and B. Dagues, "Simulation of internal faults in permanent magnet synchronous machines," *IEEE International Conference on Power Electronics and Drive Systems*, San Antonio, TX, vol. 2, pp. 1390-1395, 2005.

[38] B. Vaseghi, B. Nahid-Mobarakeh, N. Takorabet, and F. Meibody-Tabar, "Modeling of non-salient PM synchronous machines under stator winding inter-turn fault condition: dynamic model - FEM model," *IEEE Vehicle Power and Propulsion Conference*, Arlington, TX, pp. 635-640, 2007.

[39] *Rotating Machinery Insulation-Test Guide*, Doble Engineering Company, Watertown, MA, sec. 5, 1985.

[40] I. M. Culbert, H. Dhirani, and G. C. Stone, *Handbook to Assess the Insulation Condition of Large Rotating Machines*, Electric Power Research Institute, Palo Alto, CA, vol. 16, pp. 5-24 to 5-31, 2002.

[41] D. R. Albright, "Interturn short-circuit detection for turbine generator rotor winding," *IEEE Transactions on Power and Apparatus Systems*, vol. 90, pp. 478-483, 1971.

[42] R. J. Streifel, R. J. Marks, M. A. El-Sharkawi, and I. Kerszenbaum, "Detection of shorted turns in the field winding of turbine generator rotors using novelty detector development and field test," *IEEE Transactions on Energy Conversion*, vol. 11, no. 2, pp. 312-317, 1996.

[43] M. Hongzhong; D. Yuanyuan; P. Ju, and Z. Limin, "The application of ANN in fault diagnosis for generator rotor winding turn-to-turn faults," *IEEE Power and Energy Society*, Pittsburgh, PA, pp. 1-4, 2008.

[44] J. Rosero, J. Cusido, A. Garcia Espinosa, J.A. Ortega, and L. Romeral, "Broken bearings fault detection for a permanent magnet synchronous motor under non-constant working conditions by means of a joint time frequency analysis," *IEEE International Symposium on Industrial Electronics*, Vigo, Spain, pp. 3415-3419, 2007.

[45] M. Pacas, S. Villwock, and R. Dietrich, "Bearing damage detection in permanent magnet synchronous machines," *IEEE Energy Conversion Congress and Exposition*, San Jose, CA, vol.10, pp. 1098-1103, 2009.

[46] G. McPherson and R. D. Laramore, *Electrical Machines and Transformers*, John Wiley, New York, NY, 1990.

[47] P. Neti, S. Nandi, "Analysis and modeling of a synchronous machine with structural asymmetries", *IEEE-Canadian Conference on Electrical and Computer Engineering*, Ottawa, Canada, 2006, pp. 1236-1239.

[48] P. Neti, and S. Nandi, "Stator inter-turn fault detection of synchronous machines using field current signature analysis," *IEEE-Industry Applications Conference*, Tampa, FL, pp. 2360-2367, 2006.

[49] G. B. Kliman, and R. A. Koegl, "Noninvasive detection of broken rotor bars in operating induction motors," *IEEE Trans. Energy Conversion*, vol. 3, pp. 873-879, 1988.

[50] T. A. Lipo, *Analysis of Synchronous Machines*, Madison, WI: Wisconsin Power Electronics Research Center, 2008.

[51] F. Filippetti, G. Franceschini, C. Tassoni, and P. Vas, "AI techniques in induction machines diagnosis including the speed ripple effect," *IEEE Transactions on Industry Applications*, vol. 34, pp. 98-108, 1998.

[52] A. Bellini, F. Filippetti, C. Tassoni, and G. A. Capolino, "Advances in diagnostic techniques for induction machines," *IEEE Transactions on Industry Applications*, vol. 55, pp. 4109-4126, 2008.

[53] A. Bellini, F. Filippetti, G. Franceschini, and C. Tassoni, "Quantitative evaluation of induction motor broken bars by means of electrical signature analysis," *IEEE Transactions on Industry Applications*, vol. 37, pp. 1248-1255, 2001.

[54] W. Deleroi, "Broken bar in squirrel-cage rotor of an induction motor, Part I: Description by superimposed fault-currents", *Archiv fur Elektrotechnik*, no. 67, pp. 91-99, 1984.

[55] W. T. Thomson, M. Fenger, "Current signature analysis to detect induction motor faults," *IEEE Industry Applications*, vol. 7, no. 4, pp. 26-34, 2001.

[56] C. Hargis, B. G. Gaydon, and K. Kamash, "The detection of rotor defects in induction motors," in *Proc. IEE International Conference on Electrical Machines Design and Applications*, London, U.K., pp. 216–220, 1992.

[57] F. Filippetti, M. Martelli, G. Franceschini, and C. Tassoni, "Development of expert system knowledge base to on-line diagnosis of rotor electrical faults of induction motors," *IEEE Industry Applications*, vol. 1, pp. 92–99, 1992.

[58] J. Faiz, and B. M Ebrahimi, "A new pattern for detecting broken rotor bars in induction motors during start-up," *IEEE Transactions on Magnetics*, vol. 44, pp. 4673-4683, 2008.

[59] S. Williamson, and A. C. Smith, "Steady state analysis of 3-phase cage motors with rotor bar and end ring faults," *IEE Proceeding - Software*, vol. 129, no. 3, pp. 93-100, 1982.

[60] C. Demian, A. Mpanda-Mabwe, H. Henao, and G. A. Capolino, "Detection of induction machines rotor faults at standstill using signals injection," *IEEE Transactions on Industry Applications*, vol. 40, no. 6, pp. 1550–1559, 2004.

VITA

Mina Mashhadi Rahimian received her B.S. and M.S. degrees, both in electrical engineering from University of Wisconsin, Madison in 1989 and 1991, respectively. She held a lecturer position at Ferdowsi University, Mashhad, Iran until 1994, then worked as a research engineer at Oceanography International Corporation in College Station, TX, before joining the Department of Electrical and Computer Engineering at Texas A&M University as a lecturer in 2000. She joined the doctoral program in the Department of Electrical and Computer Engineering at Texas A&M University with Dr. Karen Butler-Purry as her adviser in 2006, and received her Ph.D. in August 2011. Her current research interests include fault diagnosis of electric machinery, machine design and modeling, and digital signal processing-based industrial applications.

Attn.: Mina Mashhadi Rahimian

Texas A&M University ECE Dept.

214 Zachry Engineering Center

TAMU 3128

College Station, TX 77843-3128